INFORMATION TO USERS

This manuscript has been reproduced from the microfilm master. UMI films the text directly from the original or copy submitted. Thus, some thesis and dissertation copies are in typewriter face, while others may be from any type of computer printer.

The quality of this reproduction is dependent upon the quality of the copy submitted. Broken or indistinct print, colored or poor quality illustrations and photographs, print bleedthrough, substandard margins, and improper alignment can adversely affect reproduction.

In the unlikely event that the author did not send UMI a complete manuscript and there are missing pages, these will be noted. Also, if unauthorized copyright material had to be removed, a note will indicate the deletion.

Oversize materials (e.g., maps, drawings, charts) are reproduced by sectioning the original, beginning at the upper left-hand corner and continuing from left to right in equal sections with small overlaps. Each original is also photographed in one exposure and is included in reduced form at the back of the book.

Photographs included in the original manuscript have been reproduced xerographically in this copy. Higher quality 6" x 9" black and white photographic prints are available for any photographs or illustrations appearing in this copy for an additional charge. Contact UMI directly to order.

UMI®

THE NATURE OF ROUGH-WALL STEADY, OSCILLATORY AND COMBINED BOUNDARY LAYERS

by

Rajka V. Krstić

A Dissertation Presented in Partial Fulfillment
of the Requirements for the Degree
Doctor of Philosophy

ARIZONA STATE UNIVERSITY

December 1999

UMI Number: 9940069

THE NATURE OF ROUGH–WALL STEADY, OSCILLATORY AND

COMBINED BOUNDARY LAYERS
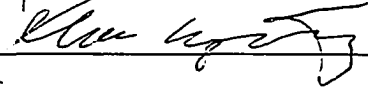
by
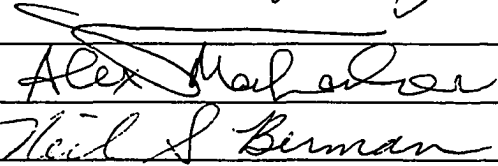
Rajka V. Krstić

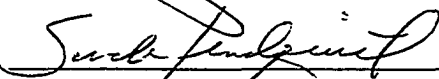has been approved

August 1999

APPROVED:

_____ ,Chair

_____

_____

_____

Supervisory Committee

ACCEPTED:

_____

Department Chair

_____

Dean, Graduate College

ABSTRACT

Oscillatory (turbulent) boundary layers over a rough wall were studied experimentally by oscillating a flat bottom plate in an otherwise quiescent fluid. The velocity field was measured with respect to a fixed (laboratory) coordinate system and was converted to that relative to a coordinate system fixed to the wall. The flow visualization revealed that the boundary layer is replete with dipole–like vortex structures generated due to flow separation at roughness elements. The boundary layer thickness was found to scale with the extent to which these vortex structures travel away from the wall. Enhanced turbulent intensities as well as vertical fluxes of horizontal momentum were observed at phases conducive for vorticity generation, that is in the proximity of maximum flow velocities. At high Reynolds numbers, the integral length–scales agreed well with the existing theoretical predictions. Eddy diffusivities based on the Reynolds and total stresses, however, did not agree with available models and showed wide variability over an oscillating cycle.

The turbulent wave–current boundary layers were studied using the long tank in the test section with the sinusoidally oscillating bottom. The turbulent steady current was achieved by water circulation throughout the long tank and the wave component was produced by oscillating bottom. The studies included determination of the boundary layer thickness, velocity profiles, turbulent kinetic energy, shear stresses, eddy viscosity and integral length–scales. It has been found that the assumption about the existence of the wave sublayer within a wave–current layer has a strong physical foundation based on the consistent behavior of various turbulent flow characteristics. The fit of mean velocity to the logarithmic profile also confirmed the existence of the wave sublayer and was used to obtain the "apparent roughness." The friction velocity changes very consistently for all experiments and its value strongly depends on the ratio of mean and amplitude velocity of oscillation. The friction

factor was determined to increase linearly with $U_m/A\omega$. Eddy viscosities based on mean and phase–averaged equations of motion, change linearly in the wave sublayer, but eddy viscosity based on phase–averaged equations of motion takes negative values. The integral length–scales were determined to be much larger than in the case of wave boundary layer, due to the strong influence of current motion that imposes large scales. The ratio of integral length–scales based on horizontal and vertical velocity components was determined to be constant with respect to Reynolds number of oscillations.

iv

ACKNOWLEDGMENTS

I am very thankful to my advisor, Professor Harindra J. S. Fernando, who guided me through the difficult stages of this research. I appreciate his mentoring and the opportunity he provided for me to work on this interesting research topic. Working in the Environmental Fluid Dynamics Laboratory, I have gained valuable experiences in establishing an independent research, working in the team environment, and I have significantly improved my technical and design skills. Moreover, Dr. Fernando has encouraged me to enroll in "Preparing Future Faculty Program" that taught me about the activities in an academic environment. I would also like to thank my Ph.D. Supervisory Committee members: Professors Don L. Boyer, Alex Mahalov, Kang Ping Chen, and Neil S. Berman for their valuable suggestions and help. I would also like to thank Professor Don L. Boyer, the Head of the Department, who provided me the opportunity to gain teaching experience, while finishing my dissertation research. The support for this research provided by the Office of Naval Research and in part by the National Science Foundation (Fluid Dynamics and Hydraulics Program) is gratefully acknowledged.

These studies were completed with the great support of many people in the Environmental Fluid Dynamics Lab: Angela Srdić-Mitrović a very good friend of mine and research colleague, Leonard Montenegro, Richard Hampton, Gabrielle Stidham and Ching. I am grateful to have the constant support of my friends from Sombor, Novi Sad, Belgrade, Tempe, Columbus, Milwaukee, San Francisco... I am especially thankful for the emotional support of my parents, Andjelka and Vukašin, and my sister Rosana. They always encouraged me to study hard and explore, and they taught me about the right life values. Finally, I owe a lot to David Corder for his constant encouragement, help and motivation. He would always put me under pressure, but with his generous support I was able to go further, higher and faster.

v

TABLE OF CONTENTS

vii

LIST OF TABLES

x

LIST OF FIGURES

xii

xiii

xiv

xvii

xviii

CHAPTER 1

INTRODUCTION

1.1 IMPORTANCE OF UNDERSTANDING THE OCEAN COASTAL BOUNDARY LAYER

Current environmental concerns on the dispersion of pollutants, as well as the recent military emphasis on littoral oceans, have triggered an increased interest on processes pertinent to continental shelf waters. The continental shelf is a heartily utilized region that involves numerous human activities, for example, mining of minerals from the beach sand, building of coastal structures, harbors and recreational areas, and, disposal of waste from municipal treatment plants. Such anthropogenic activities perturbs the natural formation and maintenance of beaches, thus leading to erosion as well as build up of sand. Underlying such changes are processes that control sediment transport, which include current and wave patterns and their interaction with sediments. Most advanced sediment transport models couple ocean boundary layer dynamics with sediment transport through suspended sediment interaction and influence of bottom roughness. The region in the immediate vicinity of the bottom influenced by the bottom roughness represents the coastal boundary layer. The boundary layer is a region where exchanges of particles, chemicals and living organisms between the ocean bottom and overlaying water take place. Though extemporal research has been done on coastal boundary layer, much remains to be done to understand the mechanics of coastal boundary layer.

The continental shelf is an extremely dynamic region due to numerous processes driving the water motion. In general, water motion is driven by surface waves, tides,

sea–surface slope, atmospheric high and low pressure regions and the density differences. Myriad of motions so generated interact with each other to form complex current patterns and phenomena of consequences of such patterns that defy predictability of current models. Improving the modeling capabilities requires increased understanding of variety processes and interactions thereof.

A major component of the continental shelf is the bottom boundary layer which is characterized by strong turbulent mixing and transport of mass, momentum and heat. Different scales of motion as well as components with different characteristics make the bottom boundary layer a challenging region to work with and model. The knowledge on important scales, parameters and their relationships is imperative for further understanding of sediment transport and erosion, and its prediction. Coastal ocean predictive tools are often utilized for planning coastal operations such as construction of piers and breakwaters, issuing warnings to recreational users and for military purposes. Most predictive tools consist of numerical models, the development of which require an adoption of certain assumptions on turbulent characteristics of the flow and recasting of these assumptions in terms of mathematical parametrizations. Most of the existing theoretical models cannot be verified by using field measurements as the details required for such a task are untenable in field programs. This is the reason why coastal engineers often resort to laboratory experiments for coastal bottom boundary-layer research.

1.2 MAIN COMPONENTS OF COASTAL BOUNDARY LAYER

To simplify the problem of coastal boundary layers, the common practice is to consider two primary forcing mechanisms: surface waves and ocean (tidal) currents. Figure 1.1 shows a schematic of possible interaction of surface waves and a ocean currents. The domain of present research is the bottom boundary layer in the region on the

continental shelf influenced by both surface waves and a ocean current, in the shoaling region of waves away from the deep ocean.

The boundary layer is defined as the layer in the immediate vicinity of the bottom where velocity changes are drastic. The thickness of the boundary layer is usually defined as the distance from the bottom where local velocity reaches 99% of the free–stream velocity. If the boundary layer is created only by surface waves, it is called the wave (or oscillatory) boundary layer (WBL or OBL). If the boundary layer is influenced by a combination of surface waves and ocean currents it is called the wave–current boundary layer (WCBL).

Field observations show that waves at the water surface induce an oscillatory motion of fluid above the bed in depths less than about the half of their wavelengths (Grant & Madsen (1986)). Laminar flow patterns over a smooth bed forced by a far field flow of harmonic oscillatory motion can be analytically described and has been understood very well. Unfortunately, the sea beds are neither smooth nor laminar and they are usually inclined, containing sand sediments and cobbles. Further, the water motion above the bed in the farfield is not strictly harmonic. Existence of turbulence is restricted to the thin boundary layer just above the seabed, which is created by the motion over the rough bottom. Large Reynolds numbers based on the amplitude and frequency of fluid oscillations always cause the development of turbulence in the wave or wave–current boundary layer. The turbulence imposes a strong shear stress on the seabed, which loosens and fluidizes the sediments. The process of such boundary layers are thus complicated and the unsteadiness of the flow as well as phase difference of oscillations of adjacent layers exacerbates the difficulty of coastal boundary layer research.

It is usual that ocean currents and surface waves propagate at an angle to each other. In such cases, the alongshore components of ocean currents carry the sediments
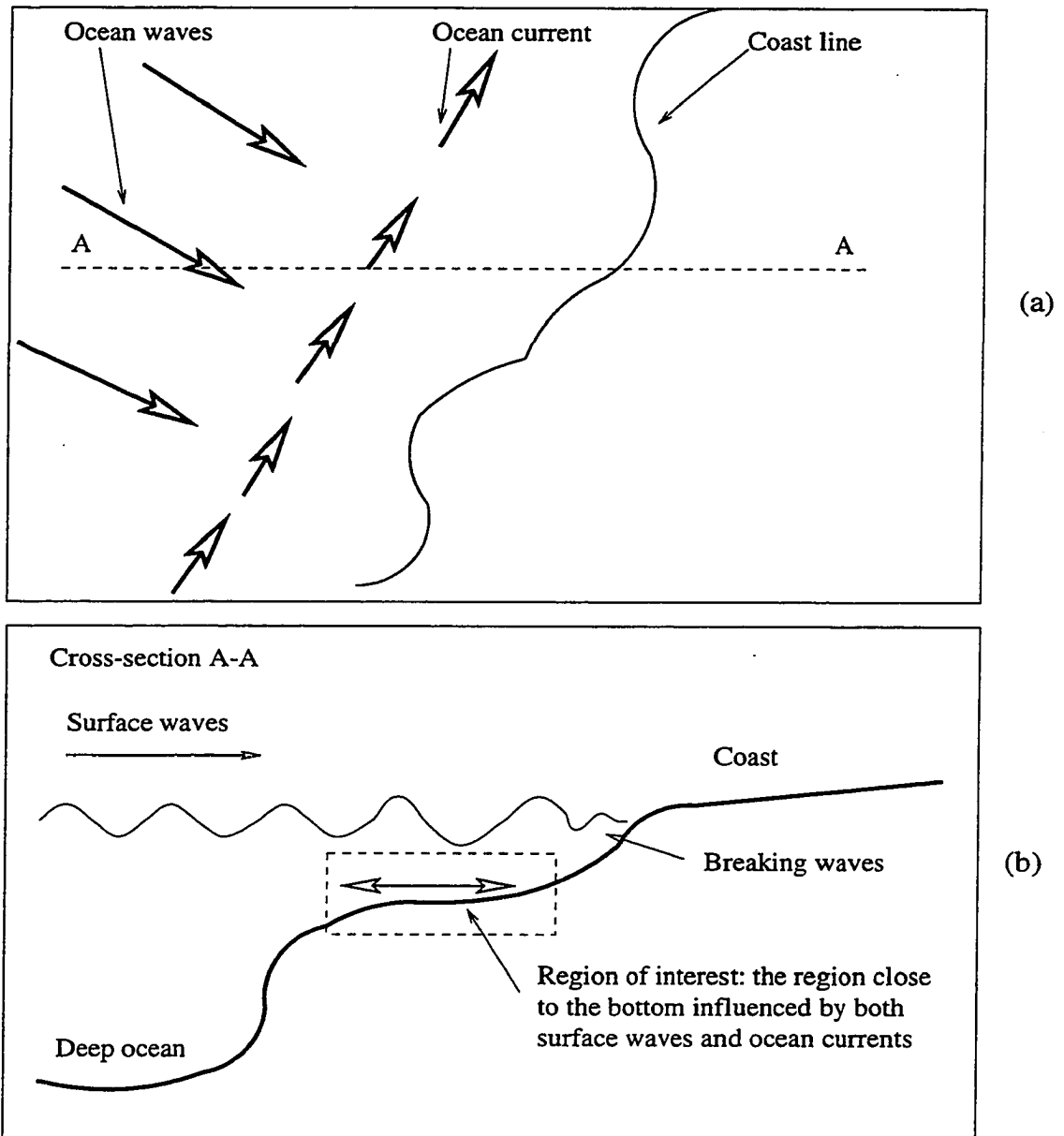
FIGURE 1.1. The primary forcing mechanisms on continental shelf: surface waves and ocean currents. (a) top view, (b) side view.

already fluidized by the wave–current boundary layer, thus complicating the mechanics of sediment transport. The sediment pile up in some areas and enhanced erosion in others can be attributed to these complex fluidization and transport mechanisms.

There are no steady currents in the ocean environment. However, the fluctuations of currents occur with time scales larger than the period of waves so that the current can be considered as steady relative to wave–current interactions. Conversely, the periodic motion induced by the waves can be considered as harmonic with relatively short period of oscillations. Therefore, superposition of ocean currents and waves having mismatched time and length–scales are typically handled as waves perturbing a steady current. Field and laboratory experimental measurements show that the coupling of those two kinds of motion is strongly nonlinear and that the characteristics of the combined flow are very different from each contributor.

1.3 MODIFICATION OF COASTAL BOUNDARY LAYER BY A MEAN CURRENT

The basic modifications of the structure of the boundary layer when waves and currents are coupled can be easily observed through modifications of velocity profiles (Nielsen (1992)). Phase–averaged velocity profiles in the case of wave induced oscillatory flow, even for the turbulent case, are periodic, and changes in magnitude and direction according to the phase of oscillations and the distance from the bottom. In addition to the change of magnitude and direction of motion, vortices are ejected from the roughness elements at the end of each half–cycle (when the flow changes its direction; Sleath (1987)). It is well known that velocity profiles of steady turbulent current follow a logarithmic–velocity distribution. The question is what would happen to the velocity profiles if waves are superimposed on the current. The previ-

Velocity Profile

Pure oscillatory flow: A = 11 cm, T = 8 s
Steady current: U_m = 9.13 cm/s, Roughness L-W-r=0.318-0.318-0.635cm
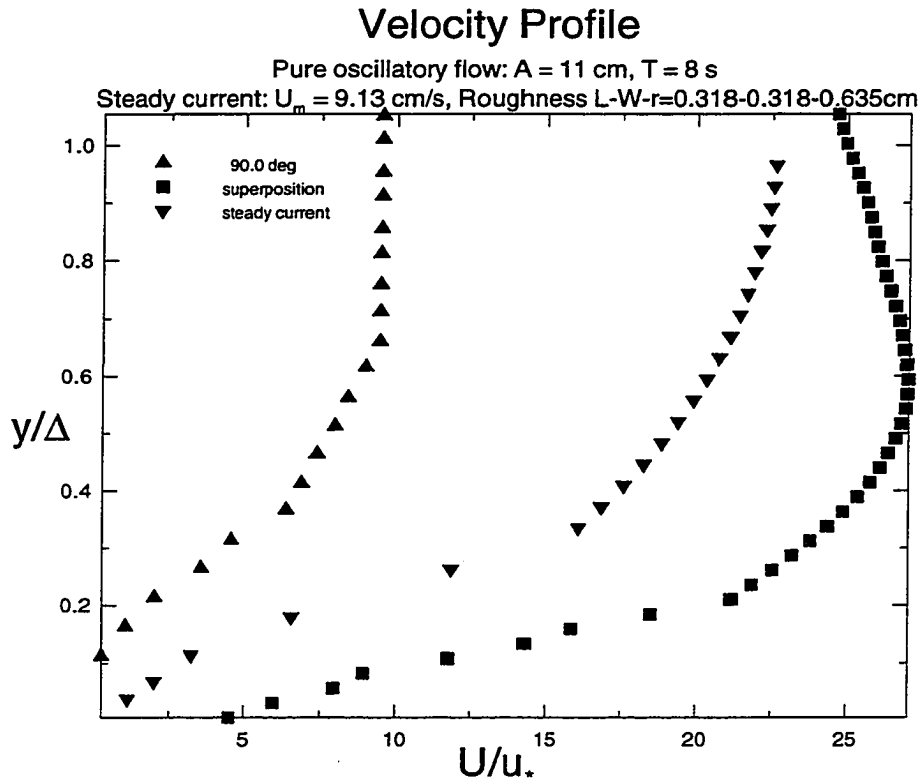
FIGURE 1.2. Comparison of the velocity profiles for the case of pure oscillatory (wave) flow, steady current flow and superposition of previous two.

ous and present experiments have demonstrated that the velocity profiles cannot be simply superimposed, but that there are significant qualitative changes.

To exemply the above discussion, let us consider velocity measurements from the present experiments shown in figure 1.2. The wave boundary layer velocity at the phase of 90° and the steady current velocity are shown when only one or the other is present. The velocity profile when the two are superimposed is also presented.

One can notice that the velocity profile of the superimposed motion does not represent simple addition of individual contributors. An important observation is

that, in the case of the superimposed motion, the velocity gradient is large close to the bottom, and greater than either of pure oscillatory motion or of steady motion. The turbulence of the oscillatory motion apparently, causes intense momentum exchange so as to make the mean profile close to the wall more uniform, thus increasing the velocity gradient near the wall. Thus, velocity profile changes from the zero at the bottom to that corresponding to the free–stream velocity in a very thin region in the immediate vicinity of the bottom. The large velocity gradient so generated enhances the bottom shear stress and, thus, directly influences the motion within the boundary layer.

Therefore, the mean (steady) and periodic (oscillatory) velocity components of a wave–current boundary layer interact in a nonlinear fashion. The data show that the addition of waves considerably changes the steady current profile. The effect of the periodic motion is the increase of velocity gradient inside the boundary layer, just above the bottom, which is believed to be the wave–dominated sublayer (Grant & Madsen (1979), see figure 1.3). Thus, the sublayer just above the bottom is called the "wave sublayer" considering the enhanced influence of the bottom roughness through the ejection of vortices from roughness elements. Thus, the coupled flow changes the characteristics of the boundary layer and creates distinct sublayers.

1.4 SCOPE OF THIS RESEARCH

The present research to be described here is devoted to the studies of the cases of steady current, pure oscillatory motion and a superposition thereof. The aim is to consider the dynamics of the shoaling region over the continental shelf over the rough bottom. The primarily interest is to determine boundary layer properties as a function of period of oscillations T (or frequency ω), semi-orbital amplitude of oscillations A, bottom roughness height r, and the intensity of mean current U_m. The main boundary

Free-stream velocity

Top of the wave-current
boundary layer

Part of the boundary layer
influenced mostly by current

Part of the boundary layer
influenced mostly by waves:
wave sublayer
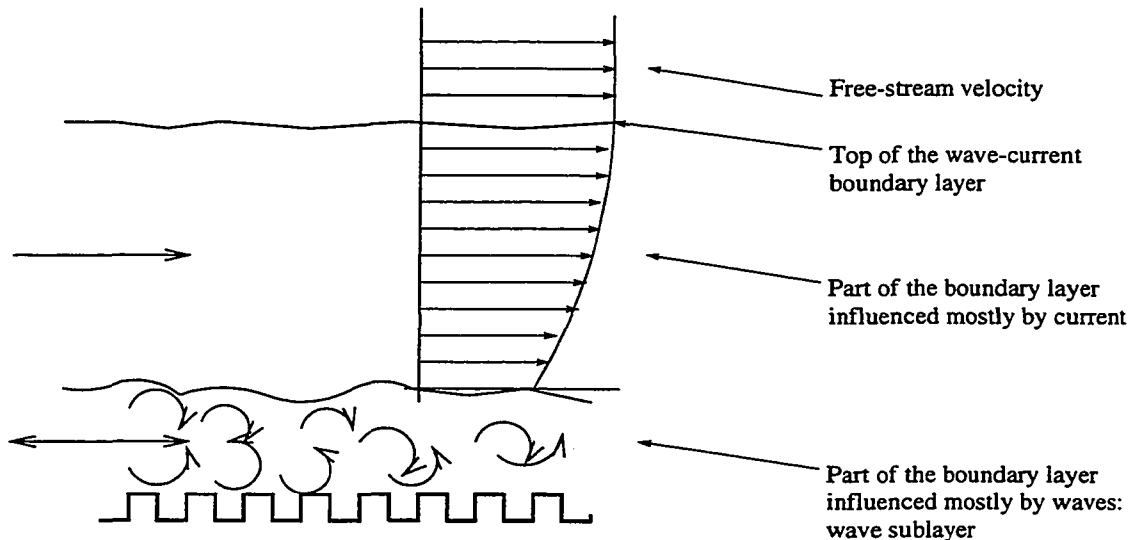
FIGURE 1.3. Definition of the wave sublayer within a wave–current boundary layer
(Grant & Madsen (1979)).

layer properties of interest are the boundary layer thickness Δ, bottom shear stress τ_b
and friction velocity u_*, distribution of turbulence intensity u_{rms}, shear stress $\tau(y,t)$,
eddy viscosity ν, and integral length–scales of turbulence $L_x{}^{uu}$, $L_x{}^{vv}$. Qualitative
observations of the structure of the boundary layer will also be presented and will be
related to turbulent characteristics of the flow.

The intention of this research is to delineate proper scaling for turbulence prop-
erties as functions of the basic flow parameters listed above. Furthermore, one of the
aims is to examine the variety of a theoretical models related to parametrization of
wave–current BL, currently used in numerical models.

In particular, we are interested in delving into the details of the theoretical models
of Grant & Madsen (1979) and Trowbridge & Madsen (1984) which are currently being
used in or considered for adoption in the wave–current boundary layer predictive
models. The sponsor of this work, the Office of Naval Research (ONR), therefore

has been interested in verifying those models using laboratory or field data. The results of this and other similar projects can also be used to understand the impact of wave–current boundary layers on the sediment transport in coastal ocean.

1.5 ORGANIZATION OF THE DISSERTATION

This dissertation is divided into the chapters. Chapter I gives a narrative description of the importance of wave and wave–current boundary layers, basic definitions and broad explanations on qualitative characteristics of coastal boundary layers. Chapter II discusses classical theory of steady boundary layers, as a precursor to the theoretical modeling of wave and wave–current BL. Only a few selected theoretical models will be described in detail, and will be used in comparison with experimental data. Chapter III describes research of wave and wave–current BL. The major conclusions on the physics of those flows will be explained. The results of sparsely suitable field measurements will be also presented. Chapter IV provides a description of experimental installations used in the current research, experimental technique and procedures. Chapter V gives a discussion on present experimental results on steady current, wave (oscillatory) and wave–current boundary layers; they will be compared with previous experimental and theoretical work. Special attention will be given to the qualitative description of the structure and the physics of the boundary layer. Chapter VI will give the summary of major conclusions and directions for future work.

CHAPTER 2

THEORETICAL CONSIDERATIONS

This chapter presents an overview of theoretical models on wave (oscillatory) and wave–current boundary layers. First, as preamble to the more complicated cases of wave boundary layers, the classical theory on the turbulent steady boundary layers will be discussed. The research that lineages to the beginning of this century, on wave boundary layers started in 1940's and were primarily experimental. Significant theoretical descriptions on wave boundary layers however, were achieved in the 1960's. At that time, several theoretical models were formulated, which will be described in this Chapter. The analytical modeling and experimental work on wave–current boundary layers began to develop in the late 1970's, but so far, there have been only a very few theoretical models and experimental measurements reported. Thus, wave–current boundary layers represent a research topic with prospects of major breakthroughs.

2.1 OVERVIEW OF THE THEORY ON STEADY–CURRENT BOUNDARY LAYERS

2.1.1 The physics of the multiple scales problem

Imagine a flow over a flat plate at large Reynolds numbers ($Re = U_m D_h / \nu$, where D_h is hydraulic diameter) such that the flow is turbulent with a boundary layer thickness Δ_c. The plate can be either smooth or rough, with an effective roughness height r. The presence of the solid wall imposes major constraint: the viscosity of the fluid imposes the no–slip boundary condition. Therefore, the viscous constraints naturally create a viscosity–dominated length–scale in the immediate vicinity of the wall. If

the kinematic viscosity of the fluid is ν and v_{rms} is the *root–mean–square*–velocity (characteristic of the level of turbulent velocity fluctuations), the viscosity–dominated length–scale is ν/v_{rms}. In general, the boundary layer thickness Δ_c is much larger than ν/v_{rms}. At large Reynolds numbers, one can surmise that small scales do not significantly influence the dynamics of the flow as the large scales control the small scales. The common approach, however, is to divide the boundary layer into sublayers characterized by different length–scales. Therefore, the viscosity–dominated scale is characteristic of the *surface layer*, while the thickness of the boundary layer is characteristic of the *outer layer*. The layer in between is described by appropriate asymptotic methods, and thus, it is called *overlap or asymptotic or matched sublayer*. Since the boundary layer thickness is larger than ν/v_{rms}, one can expect that the integral scales of turbulence in the boundary layer, especially in the outer sublayer, are on the order of magnitude of Δ_c.

The large scale motions (large eddies) govern the energy exchange between the mean flow and turbulence. The large eddies are responsible for turbulent energy production and the energy extracted from the mean flow enters the turbulence at scales comparable to integral length–scales $L_x{}^{uu}, L_x{}^{vv}, L_x{}^{uv}$.

The viscous dissipation of turbulent kinetic energy (TKE) occurs at small scales, comparable to the Kolmogorov scale l_k (smallest scale of turbulence). At very small length–scales viscosity smoothes out the velocity fluctuations and dissipates small scale energy into heat. Furthermore, small scale motions tend to have small time scales and one can assume that relatively slow large scale turbulence is statistically independent of the fast small scale turbulence. The small scale turbulence depends only on the rate of energy supplied by the large scale motion. Therefore, it is fair to assume that the rate of energy supply is equal to the rate of energy dissipated (*Kolmogorov's universal equilibrium theory*). The process explained above is very

similar to the surface sublayer where viscosity generates the "sink" for momentum and viscosity–dominated length–scales are on the order of magnitude or smaller than the Kolmogorov scale. Turbulence does not exist if the scales of motion are smaller than the Kolmogorov scale and, in that case, the only dominant parameter is diffusion. The nature of turbulence in the surface sublayer will be discussed later.

In the framework of Kolmogorov theory, the region between the large and small scales of turbulence is called the inertial subrange. In this subrange, energy is cascaded down from large to small scales at a constant rate. The transfer of energy is accomplished by vortex stretching mechanisms. When an eddy finds itself in a strain–rate field, it is stretched and compressed by the nearby eddies. The stretching involves an exchange of energy because the strain–rate field performs deformation work on eddies. At the same time, small eddies (small scale motion) are exposed to the strain–rate field of large eddies and, because of straining, the vorticity of small eddies increase at the expense of the large eddies. Therefore, inertial subrange gives the link between large scale and small scale dynamics. According to analogy between the turbulence in the boundary layer and spectral structure of turbulence, the inertial subrange corresponds to the overlap or asymptotic sublayer. In the overlap layer, the viscous–dominated length–scale is to small and the thickness of the boundary layer Δ_c is too large to affect the dynamics of motion. Therefore, it is necessary to determine intermediate scales for the description of flow in the overlap layer.

2.1.2   The governing equations for the steady current boundary layer

Theoretical analysis of boundary layer flows can be conducted only if the downstream changes are slow. Thus, it is necessary to require that $\Delta_c/l << 1$, (l is the length of the plate), so that the local scales Δ_c, ν/v_{rms} and v_{rms} are only relevant in the dimensional analysis. Let us consider the steady mean turbulent flow of a incompressible fluid
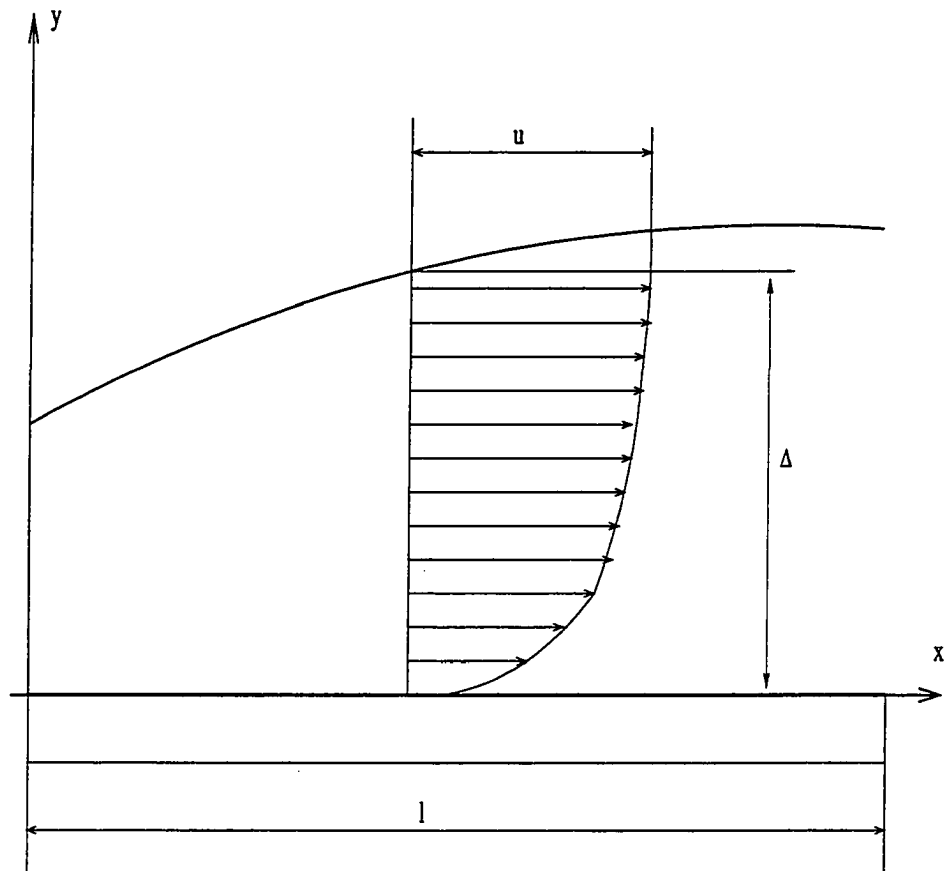
FIGURE 2.1. Steady current boundary layer thickness

along a flat plate. The plate is assumed to be long and wide, the mean flow is taken as steady, all derivatives in the downstream direction are zero, except for the pressure gradient (see figure 2.1). The relevant equations of motion for the mean flow are:

$$0 = -\frac{1}{\rho}\frac{\partial \overline{P}}{\partial x} - \frac{d}{dy}\overline{u'v'} + \nu\frac{d^2\overline{u}}{dy^2} \qquad (2.1)$$

$$0 = -\frac{1}{\rho}\frac{\partial \overline{P}}{\partial y} - \frac{d}{dy}\overline{v'^2} \qquad (2.2)$$

Integration of equation 2.2 yields:

$$\overline{P} = \overline{P_o}(x) - \rho\overline{v'^2}$$ (2.3)

where P_o is a function of x only and represents the pressure outside the boundary layer. If the equation 2.1 is integrated with respect to y from 0 upward, one obtain:

$$0 = -\frac{y}{\rho}\frac{d\overline{P_o}}{dx} - \overline{u'v'} + \nu\frac{d\overline{u}}{dy} - u_*^2$$ (2.4)

where u_*^2 is the friction velocity defined as:

$$u_* = \sqrt{\frac{\tau_w}{\rho}}$$ (2.5)

τ_w is the shear stress at the wall. Using the fact that the friction velocity is constant (since the flow is homogeneous in the streamwise direction by assumption), equation 2.4 can be evaluated for $y = \Delta_c$, and thus the friction velocity can be evaluated as a function of pressure gradient. Simple manipulation of equation 2.4 gives:

$$-\overline{u'v'} + \nu\frac{d\overline{u}}{dy} = u_*^2(1 - \frac{y}{\Delta_c})$$ (2.6)

If the Reynolds number based on the friction velocity

$$R_* = \frac{u_*\Delta_c}{\nu}$$ (2.7)

is large enough, the viscous stresses can be neglected. Therefore, the proper scaling for the Reynolds stress $-\overline{u'v'}$ is u_*^2. Similarly, velocity gradient in the outer region can be scaled with u_* /Δ_c, since turbulent scales of velocity and length are u_*^2 and

Δ_c, respectively. The nondimensional form of equation 2.6 based on outer variables can be written as:

$$-\frac{\overline{u'v'}}{u_*^2} + \frac{\nu}{u_* \Delta_c}\frac{d(\frac{\overline{u}}{u_*})}{d(\frac{y}{\Delta_c})} = 1 - \frac{y}{\Delta_c} \tag{2.8}$$

To describe the flow near the surface, the scaling for the inner layer should be introduced. The problem of different scales was discussed in the section 2.1.1. For convenience, let us define following length–scales:

$$y_+ = \frac{y u_*}{\nu} \tag{2.9}$$

$$\eta = \frac{y}{\Delta_c} \tag{2.10}$$

The first is appropriate near the wall, corresponding to very small values of the second length–scale. The implementation of these length–scales into the governing equation 2.6 will be presented in following sections.

2.1.3 Surface layer

Consider the flow over a *smooth surface* so that the height r of roughness elements is not an independent parameter. In the region close to surface, based on 2.9, the equation of motion 2.6 can be normalized as:

$$-\frac{\overline{u'v'}}{u_*^2} + \frac{d}{dy_+}(\frac{\overline{u}}{u_*}) = 1 - \frac{1}{R_*}y_+ \tag{2.11}$$

Therefore, when $R_* \longrightarrow \infty$ and $y_+ \sim O(1)$, the following solutions are expected (Tennekes & Lumley (1989)):

$$\frac{\overline{u}}{u_*} = f(y_+) \tag{2.12}$$

$$\frac{-\overline{u'v'}}{u_*{}^2} = g(y_+) \tag{2.13}$$

which is well–known the *law of the wall*. According to 2.11 the sum of the non–dimensionalized viscous and Reynolds stresses must be one throughout the surface layer. The region where neither of the stresses can be neglected is called the *buffer layer*, which is the region of vigorous turbulent energy production; here the domination changes from viscous stresses to Reynolds stresses. It has been found experimentally that this layer is in the region $y_+ = 5 - 30$ (for more information see Tennekes & Lumley (1989)).

At small heights from the surface, the largest eddies (of size of integral length–scale) should be scaled with $l = \kappa y$, where $\kappa = 0.4$ is the von Kármán constant. In addition, this region has the smallest scales of turbulence, meaning, that size of the eddies should be on the order of the Kolmogorov length–scale $(\nu^3/\varepsilon)^{1/4}$. If we non–dimensionalize the Kolmogorov and integral length–scales with respect to 2.9, and plot non–dimensional values versus y_+ (see Tennekes & Lumley (1989)), it has been shown that, in the layer in the immediate vicinity of surface $y_+ < 5$, the integral length–scale of turbulence is smaller than the Kolmogorov scale, in which the turbulence is dumped. This region is called the *viscous sublayer* or sometimes the *laminar sublayer*. It is important to emphasize that velocity fluctuations in this region exist but they do not contribute to the total stress due to strong effects of

viscosity. The thickness of the viscous sublayer is usually taken to be:

$$\delta_{vis} = 11.6 \frac{\nu}{u_*}$$

(2.14)

If we consider the flow over a *rough surface* with roughness height r, the velocity profile in the surface layer can be described as:

$$\frac{\overline{u}}{u_*} = f(\frac{y}{r}, R_r)$$

(2.15)

where $R_r = \frac{ru_*}{\nu}$ is the Reynolds number based roughness height. It has been shown that viscous stress is small at values of y/r of order one and that r/Δ_c should remain small in order that the distinct surface layer can exist.

It is accepted that the surface layer over the smooth wall is consisted from viscous and buffer sublayer. Turbulence does not exist in the viscous layer, while the buffer sublayer is characterized by the intensive turbulent production. In the case of flow over the rough surface, the surface layer exist if r/Δ_c is small. It is questionable if viscous sublayer exists since the roughness elements submerge into the viscous sublayer. Also, depending on the size and distance of the roughness elements, it is possible that turbulence exists between individual roughness elements.

2.1.4   Outer layer

The outer layer motion can be represented by the equation of motion normalized by the length–scale given in 2.10. Therefore, equation 2.8 can be rewritten as:

$$-\frac{\overline{u'v'}}{u_*^2} + \frac{1}{R_*} \frac{d}{d\eta}(\frac{\overline{u}}{u_*}) = 1 - \eta$$

(2.16)

If the $R_* \longrightarrow \infty$ and η is of order one, the equation 2.16 reduces to:

$$-\frac{\overline{u'v'}}{u_*^2} = 1 - \eta \qquad (2.17)$$

This equation represents $\eta \approx O(1)$, corresponding to the core of the flow related to channels or pipes, which is called *outer layer* (Tennekes & Lumley (1989)). Therefore, in the outer layer, the momentum equation deals only with the Reynolds stresses which reasonably scale with the square of friction velocity. In order to get explicit information on the mean velocity $\overline{u}$, it is necessary to analyze the turbulent energy equation. By the order of magnitude analysis, from TKE equation, is possible to obtain the mean velocity in the form:

$$\frac{d\overline{u}}{dy} = \frac{u_*}{\Delta_c}\frac{dF}{d\eta} \qquad (2.18)$$

where F is an unknown function to be determined. Integration from the top of the boundary layer towards the wall results in the *velocity defect law*,

$$(\frac{\overline{u} - U_m}{u_*}) = F(\eta) \qquad (2.19)$$

where U_m is mean velocity outside the boundary layer.

2.1.5   Overlap layer

The overlap layer represents the part of the boundary layer where the surface and the outer layer merge. Mathematically, this is the layer where the limits $y_+ \longrightarrow \infty$ and $\eta \longrightarrow 0$ exist simultaneously. Physically, this is the layer where both length–scales given in 2.9 and 2.10 play significant roles. The convenient way to determine the mean velocity profile in this region is to match the velocity gradients in the surface

and outer layer. Therefore, if we take the derivative of 2.12 with respect to y, it is possible to obtain:

$$\frac{d\overline{u}}{dy} = \frac{{u_*}^2}{\nu}\frac{df}{dy_+}$$

(2.20)

The gradient of the mean velocity in the outer layer is given by equation 2.18. Keeping in mind the above two limits, applying proper scaling and matching the gradients of the mean velocity leads to

$$\eta\frac{dF}{d\eta} = y_+\frac{df}{dy_+} = \frac{1}{\kappa}$$

(2.21)

It can be seen that the left–hand side of the previous equation is a function of η only, and the right–hand side is a function of y_+ only, suggesting that both sides must be equal to some universal constant. Integration of 2.21 will lead to:

$$F(\eta) = \frac{1}{\kappa}ln\eta + c = \frac{(\overline{u} - U_m)}{u_*}$$

(2.22)

which is valid for $\eta \ll 1$, and

$$f(y_+) = \frac{1}{\kappa}lny_+ + c = \frac{\overline{u}}{u_*}$$

(2.23)

valid for $y_+ \gg 1$, and κ is Kármán's constant (Kármán (1930) and Millikan (1939)). The logarithmic velocity profile is one of the most elegant contributions to turbulence theory, since it was derived based on, but without solving, the equations of motion.

Let us consider the Reynolds stresses in order to come up with another major characteristic of the overlap layer. Letting $\eta \longrightarrow 0$ in 2.17, it is possible to conclude that the Reynolds stress is constant and equal to ${u_*}^2$. Conversely, if 2.11 and 2.23

are considered, and if the limit $y_+ \longrightarrow \infty$ is taken, one can obtain the same result. Therefore, the Reynolds stress in the overlap layer is approximately constant. Furthermore, in the overlap layer the viscous stresses are negligible and to this reason it is often called the *inertial layer*. It has been determined experimentally that the overlap layer exists in the region approximately $y_+ = 30 - 350$. In engineering applications it is very common that the logarithmic velocity profile is represented as a function of the standard *Nikuradse* roughness k_s or roughness equivalent to k_s. The Nikuradse roughness can be obtained experimentally by fitting velocity of the flow over arbitrary roughness to the logarithmic profile using 2.22 or 2.23. According to the pipe flow studies of Nikuradse and later measurements, the rough pipe can be classified as follows:

- "hydrodynamically smooth": $0 < \frac{k_s u_*}{\nu} \le 5$

- "transitional": $5 \le \frac{k_s u_*}{\nu} \le 70$

- "rough": $\frac{k_s u_*}{\nu} > 70$

Using the Nikuradse roughness, the logarithmic velocity profile is usually written as:

$$\frac{\overline{u}}{u_*} = \frac{1}{\kappa} ln(\frac{30y}{k_s}) = \frac{1}{\kappa} ln(\frac{y}{y_o}) \tag{2.24}$$

2.1.6 Shear stress, eddy viscosity and mixing–length theory

One of the difficulties of turbulence modeling is to obtain relationship between the shear stress and the time–mean velocity. For a steady flow, the common approach is to assume that the mean flow is the same as the laminar one with the difference

being that kinematic viscosity ν is replaced by eddy viscosity ν_t:

$$\frac{\overline{\tau}}{\rho} = \nu_t \frac{\partial \overline{u}}{\partial y} \tag{2.25}$$

By measuring the velocity and shear stress, therefore, it is possible to determine the eddy viscosity distribution. The traditional modeling assumption, since Boussinesq (1877), is to express the shear stress as Reynolds stress (τ_R), which can be easily measured,

$$\overline{\tau_R} = -\rho\overline{u'v'} \tag{2.26}$$

An alternative approach is to use the mixing–length theory of Prandtl and Von Kármán. Prandtl suggested that turbulent eddies travel the distance l before giving up momentum to the surrounding fluid parcels. In this case, the fluctuating horizontal velocity component (u') will be equal to the gradient of mean horizontal velocity component in vertical direction ($\partial \overline{u}/\partial y$) and the distance l over which fluid particles moved, i. e. :

$$u = -l\frac{\partial \overline{u}}{\partial y} \tag{2.27}$$

Substituting 2.26 into 2.25 gives

$$v' \simeq -u' \tag{2.28}$$

The argument is based on the assumption that the eddy viscosity is positive. Therefore, if we consider a shear flow with a positive gradient of mean velocity (like the steady current flow) it is necessary to observe the values of velocity fluctuations. An

eddy coming down ($v' < 0$) to some position y will generally bring momentum from higher streamwise velocity ($u' > 0$), and vice versa, and hence the eddy motions are expected to have negative correlation $\overline{u'v'}$.

Applying 2.27 and 2.28, the Reynolds stress becomes:

$$\overline{\tau_R} = \rho l^2 |\frac{\partial \overline{u}}{\partial y}|\frac{\partial \overline{u}}{\partial y} \tag{2.29}$$

From the previous equation we can derive eddy viscosity expression as:

$$\nu_t = l^2 |\frac{\partial \overline{u}}{\partial y}| \tag{2.30}$$

According to the Prandtl and Von Kármán the mixing–length can be estimated as follows:

- surface layer: $l \simeq y^2$

- overlap layer: $l \simeq \kappa y$

- outer layer: $l = constant$

Thus, if the size of the eddies are of order l, the gradient of the mean velocity can be scaled as u_*/l. Applying previous assumption to the 2.30 we can get very well known expression for eddy viscosity distribution in the overlap layer as:

$$\nu_t = \kappa y u_* \tag{2.31}$$

The eddy viscosity concept is a popular tool in numerical modeling of coastal boundary layer. As such numerous models have been proposed, during the past thirty years, to close coastal boundary layer equations, each of them has certain advantages and disadvantages.

2.2 OVERVIEW OF THEORETICAL MODELS ON WAVE (OSCILLATORY) BOUNDARY LAYERS

2.2.1 Laminar oscillatory flow over the smooth bed – Stokes' second problem

Most natural flows tend to be turbulent, and they are developed over rough surfaces. However, the study of the laminar flow over the smooth bed provides useful clues towards efficient analysis of natural flows. The theory on laminar oscillatory flow was developed by Stokes in 1851, and since it has been known as "the Stokes' second problem".

Stokes analysis was based on linear equations of motion together with assumption of horizontal homogeneity in the x–direction:

$$\rho\frac{\partial u}{\partial y} = -\frac{\partial p}{\partial x} + \frac{\partial \tau}{\partial y} \tag{2.32}$$

The far–field velocity is u_∞ and, using the assumption that the shear stress vanishes outside the boundary layer, it is possible to write

$$\rho\frac{\partial u_\infty}{\partial y} = -\frac{\partial p}{\partial x} \tag{2.33}$$

Then the governing equation of motion can be written as:

$$\rho\frac{\partial(u - u_\infty)}{\partial y} = \frac{\partial \tau}{\partial y} = \mu\frac{\partial^2 u}{\partial y^2} \tag{2.34}$$

Let us assume, further, that the fluid column above the plate is oscillating according to:

$$u_\infty(t) = A\omega\cos(\omega t) = U_o\cos(\omega t) = A\omega\exp(i\omega t) \tag{2.35}$$

Introducing the non–dimensional velocity defect function:

$$A\omega D(y,t) = u_\infty(t) - u(y,t) \tag{2.36}$$

the governing equation 2.34 becomes:

$$\frac{\partial D}{\partial t} = \nu \frac{\partial^2 D}{\partial y^2} \tag{2.37}$$

The previous equation can be solved by the separation of variables and solution has a form:

$$D(y,t) = \sum_{n=1}^{\infty} D_n(y) \exp(in\omega t) \tag{2.38}$$

where

$$D_n(y) = A_n \exp\left(y\sqrt{in\omega/\nu}\right) + B_n \exp\left(-y\sqrt{in\omega/\nu}\right) \tag{2.39}$$

Since the velocity defect is zero at large y, the coefficient $A_n = 0$, and the boundary condition at the bed is:

$$u(0,t) = u_\infty(t) - A\omega D(0,t) = A\omega \exp\left(i\omega t\right) - A\omega \sum_{n=1}^{\infty} B_n \exp\left(in\omega t\right) = 0 \tag{2.40}$$

The previous equation gives $B_1 = 1$ and $B_n = 0$ for $n \neq 1$. Thus, the complete solution is:

$$u(y,t) = A\omega(1 - D_1(y)) \exp\left(i\omega t\right) = A\omega(1 - \exp\left(-\frac{(1+i)y}{\sqrt{\frac{2\nu}{\omega}}}\right)) \exp\left(i\omega t\right) \tag{2.41}$$

The complex velocity defect function $D_1(y)$ gives the velocity which is changing with time (t) or phase of oscillation (ωt) and with the distance from the bottom. The bottom shear stress can be easily derived from the 2.41 as:

$$\tau(y,t) = \mu A \omega (1+i) \sqrt{\omega/2\nu} \exp\left(-(1+i)\frac{y}{\sqrt{2\nu/\omega}}\right) \exp(i\omega t) \qquad (2.42)$$

The shear stress distribution is found to decrease exponentially away from the bed with the decay length–scale:

$$l_s = \sqrt{\frac{2\nu}{\omega}} \qquad (2.43)$$

which is the "Stokes length–scale". Furthermore, it can be seen from 2.42 that the bottom shear stress is a harmonic function that leads the free stream velocity by 45°.

For the case where the plate is oscillating, the velocity distribution can be obtained using the boundary condition:

$$u(0,t) = U_o \cos(\omega t) \qquad (2.44)$$

Giving the velocity distribution for the case of oscillating bed is:

$$u(y,t) = U_o \exp(i\omega t) \exp\left(-(1+i)\frac{y}{\sqrt{\frac{2\nu}{\omega}}}\right) \qquad (2.45)$$

Comparison of 2.41 and 2.45 shows a strong similarity between the solutions obtained for the boundary layer above the flat bed under the wave action (forced oscillations of the fluid column) and the one obtained above the plate oscillating in the still fluid. This similarity has the agreement of the first order only, while the second order accuracy can be obtained if the solution was obtained as the function of streamwise

coordinate x, assuming that the flow is periodic in time and in space.

2.2.2 Theoretical models for the turbulent wave (oscillatory) boundary layers

A large number of theoretical models have been proposed for turbulent oscillatory boundary layers. These theoretical models make certain assumptions about the turbulence in the boundary layer, which, at times, appeared to be unrealistic as far as oceanic boundary layers are concerned. The nature of the assumption reflects from the velocity profiles, shear stresses and turbulent characteristics of the flow. Verifications on such models can be made directly via detailed turbulent measurements or indirectly by comparing the predictions with the experimental results. Coastal ocean measurements are relatively expensive and sparse, and hence currently not suitable for testing of models. Therefore, it is necessary to collect comprehensive sets of experimental data to verify model assumptions and their performance.

Rigorous theoretical models for pure oscillatory boundary layers have been proposed by Kajiura (1968), Jonsson (1980), Brevik (1981), Myrhaug (1982), Trowbridge & Madsen (1984), Madsen & Rosengaus (1988) and several others researchers. These models were aimed at developing eddy viscosity closures for wave boundary layers by addressing questions related to the existence of logarithmic velocity profile and the overlap layer, friction factor (bottom shear stress) changes with time, and relationship between the shear stress and velocity field (eddy viscosity). The development of many of those ideas will be reviewed below through brief explanations of selected theoretical models.

Kajiura (1968) developed a comprehensive linear model for the calculation of velocity profiles based on the 2.34. The main assumptions were: (i) vertical averaged velocity and bottom shear stress are harmonic functions in time, (ii) for the case of the

smooth bottom, the boundary layer consists of three parts: inner, outer and overlap layer, (iii) for the case of the rough bottom an equivalent bottom roughness (or the new level of the bottom surface) exists, so that the three sublayers of the boundary layer are shifted in the vertical direction, (iv) the eddy viscosity distribution is time invariant. The eddy viscosity for the smooth surface was assumed to be:

$$K_y = \nu \qquad 0 < y < D_l \tag{2.46}$$

$$K_y = \kappa \widehat{u_*} y \qquad D_l < y < \Delta_w \tag{2.47}$$

$$K_y = \kappa \widehat{u_*} d \qquad d < y < \Delta_w \tag{2.48}$$

where D_l is the thickness of the viscous sublayer, $\widehat{u_*}$ is the amplitude of the friction velocity, d is the thickness of the overlap layer, and Δ_w is the total thickness of the wave (oscillatory) boundary layer. For the case of a rough bottom, the inner layer was assumed to exist up to a height of $15y_o$ (y_o was the length–scale from the logarithmic velocity profile given in 2.24). The predictions of the model included the mean velocity profile, friction coefficient and the shear stress distribution. Kajiura (1968) estimated that the overlap sublayer exists if $A/k_s \geq 30$, so that the assumption of the logarithmic velocity profile is valid as for the case of steady current flow. Kajiura's represents an impressive analytical model, but the conclusion was that the turbulent characteristics of the flow cannot be obtained using the properties averaged over a wave period.

Brevik (1981) tried to simplify the Kajiura's model by assuming a two layer eddy viscosity distribution. Simply, he omitted the inner layer and assumed that the eddy

viscosity distribution is given by

$$K_y = \kappa u_{*max} y \qquad 0 < y < \delta_o \qquad (2.49)$$

$$K_y = \kappa u_{*max} \delta_o \qquad \delta_o < y < \Delta_w \qquad (2.50)$$

where u_{*max} is the maximum of the bed friction velocity and δ_o is the thickness of the overlap layer. The periodic variations of the velocity and shear stress were represented as harmonic functions of time. The eddy viscosity was a function of the distance from the bottom only and the nonlinear terms in the 2.34 were neglected. Therefore, this model appears to be an attempt to reduce the tediousness of Kajiura's model rather than attempt to incorporate new physics.

Myrhaug (1982) developed a model somewhat similar to that of Brevik (1981). The difference between these two models is that the eddy viscosity in Brevik's model is a linear function of the distance from the bottom in the overlap layer, whereas Myrhaug assumed a quadratic function:

$$K_y = 0.5\kappa u_{*max} \delta_o \qquad y > \delta_o \qquad (2.51)$$

$$K_y = 0.5\kappa u_{*max} \delta_o (1 - (\frac{z}{\delta_o} - 1)^2) \qquad 0 < y < \delta_o \qquad (2.52)$$

The differential equation of motion took the form of the Legendre's differential equation, and the model predictions were in good agreement with the experimental data of Jonsson (1980) and Jonsson & Carlsen (1976). Further, Myrhaug (1982) calculated

the bottom shear stress, bottom friction coefficient, and the shear stress distribution. However, no information on turbulent properties of the flow were provided.

Jonsson (1980) reviewed experimental and theoretical investigations on wave boundary layers. He derived a new expression for a friction factor coefficient as the function of A/k_s, which results are in better agreement with experiments. Also, he suggested the modified logarithmic phase averaged velocity profile, which had an explicit component dependent on time:

$$\frac{u}{u_{1*}} = -\frac{1}{\kappa}\ln(\frac{30y}{k_s})\cos(\omega t + \phi_o) \tag{2.53}$$

The u_{1*} is calculated from the expression of Jonsson (1980) for the friction factor and ϕ_o is the phase of the velocity at $y = 0$.

A general characteristic of previous theoretical models is that all of them considered the eddy viscosity to be invariant in time, although the flow is obviously time dependent. This was a bare for numerical studies as these models cannot account for time dependent development of turbulence in the boundary layer. The next advancement of the theoretical modeling was the corporation of time and space dependent eddy viscosity. However, we still do not have enough space–time and structure information on turbulence properties which can be directly used in modeling of oscillatory turbulent flows. Thus, the importance of the eddy viscosity is to relate the kinematics (flow field, velocity) to the dynamics (forces, i. e. shear stresses) of the flow. Solving the problem of eddy viscosity can open up myriad of opportunities to predict the turbulent characteristics of the flow using numerical calculations.

The first theoretical model of the wave boundary layer, taking into account the space–time dependence of eddy viscosity was given by Trowbridge & Madsen (1984).

The main assumptions were that the viscous stresses are negligible or small in comparison to Reynolds stresses and that the free-stream velocity changes according to:

$$u_\infty = A\omega \cos\theta = A\omega \cos(\omega t - kx) \tag{2.54}$$

The momentum equation 2.34 was solved assuming that the velocity profile is of the form:

$$u(x, y, t) = \Re\{\sum_{n=0}^{\infty} u^{2n+1}(y) \exp(i(2n+1)\theta)\} \tag{2.55}$$

i. e. the velocity is expressed by odd harmonics of the Fourier series. The shear stress is expressed similarly and the relationship between the velocity gradient and shear stress suggested that the eddy viscosity contains only an even harmonics:

$$\nu(x, y, t) = \Re\{\sum_{n=0}^{\infty} u^{2n}(y) \exp(i2n\theta)\} \tag{2.56}$$

The modeling of eddy viscosity was based on that of the steady current case and the final mathematical form of their model for eddy viscosity was:

$$\nu = \nu^{(0)}(z)\Re[1 + a^{(2)} \exp(i2\theta)] \tag{2.57}$$

where

$$\nu^{(0)} = \kappa u_* y \qquad 0 < y < \delta_1 \tag{2.58}$$

$$\nu^{(0)} = \kappa u_* \delta_1 \qquad \delta_1 < y < \Delta_w \tag{2.59}$$

and the thickness of the overlap layer δ_1 was assumed to be $1/6l$, where l is the characteristic length–scale defined by Grant & Madsen (1979):

$$l = \kappa \frac{u_*}{\omega}$$ (2.60)

The friction velocity was defined as:

$$\overline{u_f} = \overline{|\frac{\tau_b}{\rho}|^{1/2}}$$ (2.61)

while the coefficient $a^{(2)}$ was defined as:

$$\overline{u_f}a^{(2)} = \overline{2\exp{(-2i\theta)}|\frac{\tau_b}{\rho}|^{1/2}}$$ (2.62)

Eddy viscosity in this model, represents the product of the vertical scale and the first two Fourier components of a shear velocity based on the instantaneous local bed shear stress. They obtained an approximate closed–form solution for the velocity distribution in the boundary layer, and thus, were able to calculate turbulence characteristics such as energy dissipation, instantaneous shear stress and friction factor. They assumed that the time–varying eddy viscosity has the same vertical structure as that of the steady current case. Calculations show, however, that the time–dependent portion of eddy viscosity decay more rapidly with the distance from the bed than the eddy viscosity for steady boundary layers, the reason being that the time–scale for the decay of turbulent kinetic energy is much smaller than the period of oscillations.

2.2.3 Numerical modeling of turbulent oscillatory boundary layers

The analytical modeling which prevailed in 1960-1980's was replaced by the pure numerical modeling in the beginning of 1990's. Development of the mathematical

theories, grid generation methods and algorithms contributed to the major application of numerical modeling of turbulent flows. However, this development has its own problems, since the numerical models should introduce the minimum amount of complexity while capturing the essence of relevant physics. Thus, in order to capture dynamics of turbulence, it is necessary to detect the changes at the large (integral) and small (Kolmogorov) scales as functions of time.

Justesen (1988) applied a two equation $k - \varepsilon$ and one equation $k - l$ turbulence model on the wave boundary layers in order to investigate the distribution of turbulent kinetic energy, integral length–scales and shear stress. The purpose of his study was to compare turbulence characteristics calculated by different numerical methods. In an extension of this work, Justesen (1991) improved the two equation turbulence model and compared the numerically obtained turbulence properties with available experimental data. The turbulent kinetic energy (TKE) was found to be highest at the bed and has maximum at the phase when the production of TKE is maximum. Away from the bed, TKE is sustained by the diffusion from the near–wall region. Observations of the length–scales showed that the length–scales increase away from the bottom, in agreement with what is expected from a decaying turbulent flow. Calculations of the friction factor were slightly underestimated by this model in comparison to experiments. However, both studies of Justesen showed that refined numerical models are required in capturing important changes of turbulence characteristics.

Brørs & Eidsvik (1994) applied a standard Reynolds stress model for oscillatory boundary layers. This model was somewhat more complicated then the standard $k - \varepsilon$ model, but both of them predicted the data reasonably well. High Reynolds number data were predicted to a great detail, especially the variations of boundary layer thickness and bottom shear stress amplitude. They also applied their model to study sediment entrainment by waves.

Waywell & Sajjadi (1997) modeled the transition from laminar to turbulent flow in oscillatory boundary layers over smooth surface. They used three differential second–moment (DSM) closure models and compared the results with those of previous models in order to compare the performance. The main aim was to capture the transition in the first acceleration stage of the oscillation cycle by continuing calculations straight "to the wall" via integration of equations of motion. The assumptions of this models include the balance of turbulent production with dissipation in the vicinity of the bed, the existence of logarithmic velocity profile and the existence of constant shear layer during the whole cycle.

Sajjadi & Waywell (1997) used turbulence models to study the oscillatory flow over the rough bottom. They implemented the $k - l$ and differential second–order model (DSM). Modification of the models was related to the boundary conditions where the local state of the bed roughness has been used instead of traditional no–slip velocity condition. The prediction for the near–bed turbulent kinetic energy profile was improved by this method.

Chowdhury, Sato & Ueno (1997) used a closure scheme based on one equation turbulent model to study mean characteristics of the boundary layer created by different amplitudes of water waves. This appears to be a step back in modeling work, but their implementation of a time varying eddy viscosity was a salient point. The eddy viscosity was related to the characteristic turbulent velocity (*rms*–velocity) and length–scales of turbulence. They concluded that the stable mean velocity profiles is achieved after 22 cycles of oscillations and that the depth of the boundary layer gradually increases from deep to shallow water.

There are many other numerical studies on wave boundary layers; Sleath (1974), Madsen & Rosengaus (1988), Savioli & Justesen (1997), and Vittori & Verzicco (1998), to name a few. It can be seen that the most of numerical research has been

done in the last decade and that appropriate schemes capable of representing turbulence characteristics are still under development. However, it is obvious that the numerical studies cannot further develop without supporting experimental data as the later is required to obtain an understanding of physics and verification of models pertinent to oscillatory boundary layer flows.

2.3 OVERVIEW OF THEORETICAL MODELS ON WAVE–CURRENT BOUNDARY LAYERS

2.3.1 Theoretical models for the wave–current boundary layers

One of the first attempts to establish mathematical model for wave–current interaction was given by Grant & Madsen (1979). The complexity of this problem rises due to contrasting time–scales associated with slowly varying, essentially steady current, and unsteady oscillatory motion caused by the surface waves. For the purpose of modeling, the current can be considered as steady and fully developed, with its boundary layer (of thickness Δ_{cw}). The shear stress at the bottom surface is significant in this type of flows. However, the region where shear stress associated with the wave (oscillatory) motion dominates, is placed in the thin sublayer just above the bottom, considering the short time–scale of interaction between the fluid parcels and bottom roughness. This particular sublayer is called the wave sublayer and it has a thickness δ_w. Therefore, in the immediate vicinity of bottom the shear stress and turbulent intensities are considered to exist due to combined effects of waves and current. Due to the complex nature of the flow, one must assume that two effects are coupled non–linearly. In the region above the wave sublayer, the current experiences shear stress partially due to the bottom roughness and partially due to the existence of wave sublayer. The wave sublayer has physical characteristics as the inner layer of the steady current, while the layer just above the wave sublayer can be considered

as an overlap layer for the steady current. If one chooses the Nikuradse roughness height to reflect the characteristics of physical rough bottom and turbulence in the wave sublayer, the current velocity profile in the layer above the wave sublayer (or in the overlap layer for steady current) will be logarithmic according to:

$$\overline{U}_c = \frac{u_{*c}}{\kappa} ln \frac{30y}{k_{cw}} \qquad y > \delta_w \qquad (2.63)$$

while the distribution of mean steady current velocity profile inside the wave sublayer would be:

$$\overline{U}_c = \frac{u_{*c}}{\kappa} \frac{u_{*c}}{u_{*cw}} ln \frac{30y}{k_s} \qquad y < \delta_w \qquad (2.64)$$

The Nikuradse roughness k_{cw} is called the *"apparent roughness"* according to Grant & Madsen (1979), $u_{*c}^2 = \kappa |u_{*c}| y \partial u_c / \partial y$ valid for $y > \delta_w$ and u_{*cw} is defined by expression $\kappa |u_{*cw}| y \partial u_c / \partial y = u_{*c}^2$ valid for $y < \delta_w$. Since numerical modeling is sensitively dependent on the relation between the dynamics (shear stress) and kinematics (velocity field) of the turbulent flow, the eddy viscosities in the two sublayers are described in analogy with steady boundary layers as:

$$\varepsilon_c = \kappa |u_{*c}| y \qquad y > \delta_w \qquad (2.65)$$

and

$$\varepsilon_{cw} = \kappa |u_{*cw}| y \qquad y < \delta_w \qquad (2.66)$$

Furthermore, Grant & Madsen (1979) proposed the length–scale of the wave sublayer as:

$$l = \frac{\kappa |u_{*cw}|}{\omega} \qquad (2.67)$$

where the thickness of the wave sublayer is $\delta_w \approx 2 - 4l$. It is important to emphasize that, according to Grant & Madsen (1979), the eddy viscosity in the wave sublayer is time–invariant. At the time of their research, little experimental data were available to check their numerical results. Thus, Grant & Madsen (1979) compared model results with available experimental data for wave boundary layers.

Another theoretical model was proposed by Sleath (1991) who assumed that the shear stress is linked to the velocity gradient in the combined flow through an eddy viscosity expressed as:

$$\varepsilon = \varepsilon_c + \varepsilon_w \qquad (2.68)$$

where ε_c is the eddy viscosity for the steady current alone and ε_w for the wave motion alone. This was based on his experimental work (Sleath (1990)) which showed that the mean square turbulent intensity of the combined flow is approximately equal to the summation of the mean square turbulent intensities of individual components. Eddy viscosity for the current was defined by 2.31, while the eddy viscosity for the wave motion was defined from mixing length arguments as $\varepsilon = v'l$. He also modified the steady current velocity profile in a such a way that the argument of logarithmic profile depends on $\frac{U_o}{u_*}(\frac{A}{k_s})^{0.5}$, by which he introduced the wave forcing of the flow. Sleath (1991) by comparing his results with the results of Grant & Madsen (1979), found that 2.68 predicts velocity measurements close to the bed much better. The model

of Sleath (1991) also treats eddy viscosity for the wave motion as time–independent. Furthermore, superposition of eddy viscosities diminishes the significance of nonlinear coupling between wave and current forcing.

Since the large number of theoretical models that have been proposed do not predict the experimental data satisfactory, Madsen & Wikramanayake (1991) developed a theoretical model that allowed the eddy viscosity to vary with time, in addition to its spatial variation, for the case of a weak current. They assumed that the wave motion is periodic and that the velocity components, pressure and eddy viscosity can be decomposed into mean (time–independent) and time–dependent components. The time–dependent components are further decomposed into even and odd harmonics, using the Fourier expansion. The steady current velocity was obtained by time–averaging of the momentum equations while time–dependent velocity components were implicitly obtained by subtracting time–averaged and instantaneous equations of motion. The weak current assumption was used to derive the ratio of friction velocities of the current and wave motion. It was assumed that the friction velocity of the current is less than the friction velocity of the wave motion, the later being time–dependent. Eddy viscosity was assumed to be a function $\varepsilon_t = g(z)f(t)$, where $f(t)$ is obtained from temporal variation of friction velocity. The bottom shear stress was decomposed into the first harmonic of the bottom shear stress and even and odd harmonics of the shear stress above the bottom which are time and space dependent. Time dependent friction velocity was obtained directly from bottom shear stress, while eddy viscosity had a form of eddy viscosity for steady current with a time dependent friction velocity. This model gave a good comparison with experiments for small heights from the bottom.

A theoretical approach on the studies of turbulence in the wave–current interaction was offered by Nielsen (1992), which appeared to be based on the original

decomposition of Hussain & Reynolds (1970). The instantaneous components of velocity (u, v, w) are decomposed into a mean, periodic and fluctuating component as:

$$u = \overline{u} + \tilde{u} + u'$$

(2.69)

The periodic component is defined as the phase averaged component over N periods minus the time average:

$$\tilde{u} = \frac{1}{N}[\sum_{j=1}^{N} u(x, y, t + jT)] - \overline{u}(x, y)$$

(2.70)

Introducing this velocity decomposition into Navier–Stokes equations and taking time– and phase–average it is possible to obtain the mean and phase–averaged momentum flux in the vertical direction as:

$$\overline{\tau} = \mu\frac{\partial \overline{u}}{\partial y} - \rho\overline{u}\ \overline{v} - \rho\overline{\tilde{u}\tilde{v}} - \rho\overline{u'v'}$$

(2.71)

and

$$\tilde{\tau} = \mu\frac{\partial \tilde{u}}{\partial y} - \rho\overline{u}\tilde{v} - \rho\tilde{u}\overline{v} - \rho\widetilde{\tilde{u}\tilde{v}} - \rho\widetilde{u'v'}$$

(2.72)

For the details on the derivation see Nielsen (1992). Based on 2.71 and 2.72, the eddy viscosity "felt" by the steady current is:

$$\nu_c = \frac{\overline{\tau}}{\rho\frac{\partial \overline{u}}{\partial y}} = \frac{\overline{u}\ \overline{v} - \overline{\tilde{u}\tilde{v}} - \overline{u'v'}}{\frac{\partial \overline{u}}{\partial y}} + \nu$$

(2.73)

and the eddy viscosity "felt" by the periodic component is:

$$\nu_w = \frac{\tilde{\tau}}{\rho \frac{\partial \tilde{u}}{\partial y}} = \frac{\overline{\tilde{u}}\,\overline{\tilde{v}} - \widetilde{\bar{u}\bar{v}} - \widetilde{\tilde{u}\tilde{v}} - \widetilde{u'v'}}{\frac{\partial \tilde{u}}{\partial y}} + \nu \tag{2.74}$$

It is also clear that ν_c is constant in time, while ν_w is a function of time as well as the vertical distance y. According to Nielsen's review on previous experimental results (Nielsen (1992)), the eddy viscosity given by 2.74 can take negative, positive or infinite values. Moreover, it has been determined that the eddy viscosity ν_c is three to four times greater than the ν_w. According to Nielsen (1992), there are alternative ways of defining eddy viscosity based on previously given momentum equations. Therefore, the 2.73 and 2.74 represent an attempt to analytically express eddy viscosity.

Nielsen (1992), in his study on the change of steady velocity profile in the presence of waves adopted the concept of "apparent roughness" from the model of Grant & Madsen (1979). He argued that the apparent roughness depends on the relative current strength, relative roughness and the angle between waves and current, viz.,:

$$\frac{k_{cw}}{k_s} = F(\frac{A\omega}{\overline{u}_*}, \frac{r}{A}, \varphi) \tag{2.75}$$

Determination of the dependence of apparent roughness on the flow parameters will be one of the major goals in the present research.

2.3.2 Numerical modeling of wave–current boundary layers

There are very few numerical models dealing with wave–current boundary layers, mainly because of the poor understanding of the physics of this complex problem. There are very few experimental investigations and, at this moment, the amount of data is grossly insufficient to provide adequate comparisons with the numerical

predictions. The following is s brief overview of wave–current numerical modeling studies.

The eddy–viscosity model of Grant & Madsen (1979) has been implemented by Fredsøe (1984), who numerically modeled the wave–current interaction for the case of an arbitrary angle between the directions of wave and current propagation. The mean velocity profiles were obtained using the depth–integrated x–momentum equation. The main assumption was that the velocity is logarithmic inside as well as outside the wave boundary sublayer, but with different slopes. From these logarithmic mean velocity profiles, he calculated the values of apparent roughness. Work of Fredsøe (1984) included the calculation of shear stress from the integral–momentum equation, thus avoiding an explicit formulation for eddy viscosity.

In order to facilitate computing of wave–current interaction, Madsen (1994) developed a theoretical model using linearized momentum equations and time–invariant eddy viscosity. The wave motion was specified by the directional spectrum of the near–bottom orbital velocity. This work was definitely valuable for the development of numerical approaches, but reflected a step back in the determination of relation between the kinematics and dynamics of the wave–current flows as it assumed time–invariant eddy viscosity.

Recent modeling of Malarkey & Davies (1998) was based on model of Grant & Madsen (1979). In the former case, the eddy viscosity had odd and even time–dependent harmonics of the Fourier series expansion. The model was based on the assumption that velocity, eddy viscosity, shear stress and pressure can be decomposed into averaged and time dependent components. The variation of instantaneous velocity of the current due to the asymmetry of turbulence in two successive wave half–cycles was also included. It was found that the time–dependent eddy viscosity

reduces non-linear coupling between wave and current forcing. The velocity predictions of Malarkey & Davies (1998) agreed well with the experimental data of Jonsson & Carlsen (1976).

A numerical investigation on the mean flows generated by surface waves was conducted by Knobloch & Pierce (1998). The intention of this research was to determine the connection between the mean flow, mean surface elevation and modulations of wave amplitude. In this investigation, inviscid waves were investigated with the assumption that the flow is viscous in the interior of the fluid. This model delineated time scales of the evolution of weakly non-linear waves (of order of minutes), and viscous diffusion time scale (of order of hours or days). As such, the bottom boundary layer is expected to behave as inviscid over the time scale of typical engineering applications.

It is interesting to note that the majority of presented models have employed the wave-current boundary layer model of Grant & Madsen (1979). With the availability of more data, however, it is possible to expect refinements in numerical modeling efforts on wave-current boundary layers.

2.4 THE SUMMARY OF THEORETICAL MODELING

General characteristics pertinent to the theoretical modeling of wave boundary layers can be summarized as follows:

- Early theoretical models were based on certain assumptions related to the physics of turbulence based on which the researchers were able to calculate the mean properties of the flow (velocity, shear stress and eddy viscosity). Attempts have also been made to model the wave (oscillatory) boundary layer using theoretical foundations underlying steady current boundary layers, for

example by assuming the existence of a logarithmic velocity profile and that the eddy viscosity is a linear function of the distance from the bed (Kajiura (1968), Brevik (1981), Jonsson (1980), Myrhaug (1982)).

- The major challenge for analytical modeling was the finding of a proper relation between the kinematics (velocity profile) and dynamics (shear stresses or forces) of the flow. This relation represents the eddy viscosity, and it is now recognized that in oscillatory (periodic) flows, the eddy viscosity must be treated as the function of the distance from the bottom and the phase of oscillations (Trowbridge & Madsen (1984)).

- Complexity and mathematical limitations of analytical models led to the development of numerical models which were intended to capture the changes of instantaneous turbulence properties (Justesen (1988), Justesen (1991), Waywell & Sajjadi (1997), Sajjadi & Waywell (1997), Chowdhury et $al.$ (1997), etc.), in addition to mean variables. Numerical models are still in the development and further experimental data are required for their validation and refinement.

- A variety of scaling are used for oscillatory boundary layers, but their universality is yet to be established.

Available theoretical models on wave–current flows are sparse and have the following general characteristics:

- The majority of models are based on the existence of an "apparent roughness" and the parametrization of non–linear interaction between waves and current proposed by Grant & Madsen (1979).

- The problem, as in the case of the wave boundary layer, appears to be the formulation of eddy viscosity. So far, two major attempts have been reported

on the formulation of the eddy viscosity. One is based on the foundation of the steady current theory, in that the eddy viscosity changes linearly with the distance from the bottom (Grant & Madsen (1979)) and that the viscosity of steady current and wave motion can be simply superimposed (Sleath (1991)). The second attempt is based on the equations of motion, allowing eddy viscosity to change with the phase of oscillations in addition to its dependence on the distance from the bottom (Nielsen (1992)).

- Numerical modeling efforts still continue and their progress is currently hindered by the lack of experimental data and information on the physics of turbulence.

CHAPTER 3

PREVIOUS EXPERIMENTAL WORK

This chapter gives an overview of the techniques used and results obtained in previous laboratory experiments. First, a brief introduction will be given to different types of experimental facilities. Overview of the experiments on the wave and wave–current boundary layer will be given next. Finally, the findings of major field measurements will be presented.

3.1   TYPES OF EXPERIMENTAL APPARATUSES

Due to the cost and practical difficulties involved with field measurements, the bulk of the experimental work on coastal hydrodynamics is carried out in the laboratory using three major types of installations; see figure 3.1. One of the most frequently used installation is the oscillating water tank or the "U–tube". Here the flow is driven by a piston placed in one of the vertical limbs, while the other limb is completely open. In order to achieve high Reynolds numbers, it is necessary to have large amplitude of water oscillations, and thus the test section is usually very long (2–10 m). The orbital motions of fluid in the test section are very uniform in the horizontal direction and a good design of the U–tube enables zero vertical motion. The turbulence in the U–tube is enhanced by the bottom roughness (sand, two or three–dimensional calibrated roughness elements).

The second popular installation is the wave tank, which is a facility capable of creating actual waves. The wave maker is placed at one end of a tank, creating waves of desired characteristics (such as height, frequency and wave number). It is the usual case that, on the opposite side of the wave maker, the bottom surface is
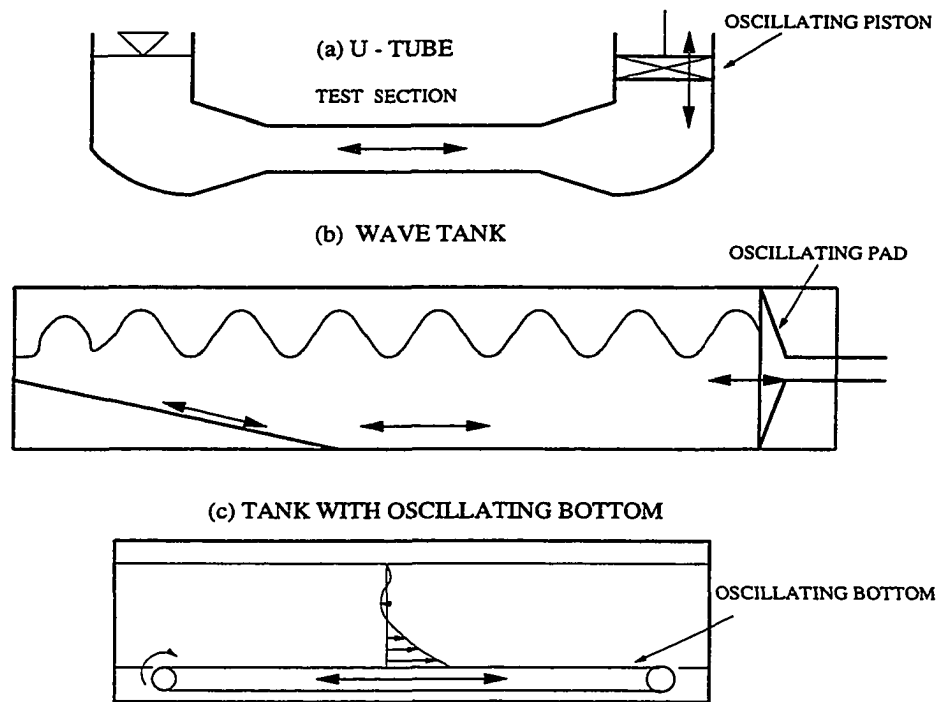
FIGURE 3.1. Types of experimental installations: (a) U–tube, (b) wave tank, (c) tank with the oscillating bottom.

inclined creating "beach" conditions. Wave tanks can be very large facilities and their length can go up to 80 m.

Due to the considerable cost and complexity of design of oscillating water tunnels and wave tanks, a tanks with oscillating bottoms are used to study wave boundary layers. Instead of oscillating the bulk fluid, the bed is oscillating in its own plane through otherwise quiescent water. The flow generated herein is similar to that of an oscillating water tunnel if the measured velocity is transformed as:

$$u^*(y, t) = u(y, t) - u_\infty(t) \qquad (3.1)$$

However a question arises as to the suitability of oscillating–bottoms in studying oscillatory boundary layers created by oscillating fluid columns. A detailed mathematical explanation of the similarity between the two velocity fields will be given in following discussion.

Similarity between flow due to an oscillatory bottom and that due to far–field fluid oscillations

So far, several researchers have used results obtained from oscillating bottom experiments to make inferences on wave boundary layers (see Kalkanis (1964), Sleath (1974), George & Sleath (1979), Jonsson (1980), Du Toit & Sleath (1981), Sleath (1984), Sleath (1990), Earnshaw (1996)). This is based on the fact that there is kinematic similarity between the velocity field obtained relative to an oscillating coordinates ($\underline{x}^*$) fixed to the bottom and what is seen in oscillating fluid column. If one measures the velocity relative to an inertial coordinate system ($\underline{x}$) fixed to the laboratory, and the bottom is oscillating with a velocity $u = U_o sin(\omega t)$, then with respect to the oscillating coordinate system, the flow velocity is $u - U_o sin(\omega t)$. In order to transform the velocity field obtained by the installation with oscillatory bottom ($\underline{u}$–field) to the velocity field similar to ocean ($\underline{u}^*$–field), one can simply use the following transformations:

$$u^*{}_1 = u_1 - U_o sin(\omega t) \tag{3.2}$$

$$u^{*2} = u_2 \tag{3.3}$$

$$u^{*3} = u_3 \tag{3.4}$$

under the assumption of sinusoidal oscillations of the bed. This is the same as the velocity defect observed in the oscillatory fluid experiments or in real wave boundary layers $(U_o sin(\omega t) - u_1)$, thus establishing kinematic similarity between the two. The question is: does the velocity field generated by the bottom oscillations with $u = U_o sin(\omega t)$ create a velocity field that is <u>dynamically</u> equivalent to oscillations of the water column with a far–field fluid velocity $U_o sin(\omega t)$.

Let us consider two systems: inertial, with coordinates described by (x_1, x_2, x_3, t), and non–inertial with coordinates $(x_1{}^*, x_2{}^*, x_3{}^*, t^*)$ which oscillate relatively to the inertial system so that its origin is at $x_1 = -A\cos(\omega t)$. Thus, the relations between coordinates can be expressed as:

$$x_1{}^* \;=\; x_1 + A\cos(\omega t) \tag{3.5}$$

$$x_2{}^* \;=\; x_2 \tag{3.6}$$

$$x_3{}^* \;=\; x_3 \tag{3.7}$$

$$t^* \;=\; t \tag{3.8}$$

Consider the incompressible Navier–Stokes equations and the continuity equation, applied to the motion in an inertial frame:

$$\frac{\partial u_i}{\partial t} + u_j \frac{\partial u_i}{\partial x_j} = -\frac{1}{\rho}\frac{\partial p}{\partial x_i} + \nu \frac{\partial^2 u_i}{\partial x_j{}^2} \tag{3.9}$$

$$\frac{\partial u_j}{\partial x_j} = 0 \tag{3.10}$$

Any variable f derived with respect to x_1 or t gives:

$$\frac{\partial f}{\partial x_1} = \frac{\partial f}{\partial x_i^*}\frac{\partial x_i^*}{\partial x_1} + \frac{\partial f}{\partial t^*}\frac{\partial t^*}{\partial x_1} = \frac{\partial f}{\partial x_1^*} \tag{3.11}$$

$$\frac{\partial f}{\partial t} = \frac{\partial f}{\partial x_i^*}\frac{\partial x_i^*}{\partial t} + \frac{\partial f}{\partial t^*}\frac{\partial t^*}{\partial t} = -\frac{\partial f}{\partial x_1^*}A\omega\sin(\omega t) + \frac{\partial f}{\partial t^*} \tag{3.12}$$

Applying previous transformations into equation 3.9 and equation 3.10, one can obtain:

$$\frac{\partial u_i}{\partial t^*} - A\omega\sin(\omega t)\frac{\partial u_i}{\partial x_1^*} + u_j\frac{\partial u_i}{\partial x_j^*} = -\frac{1}{\rho}\frac{\partial p}{\partial x_i^*} + \nu\frac{\partial^2 u_i}{\partial x_j^{*2}} \tag{3.13}$$

$$\frac{\partial u_j}{\partial x_j^*} = 0 \tag{3.14}$$

At the same time, according to 3.8, the origin of non–inertial frame moves with velocity $(A\omega\sin(\omega t), 0, 0)$. Using the velocity transformations

$$u_1^* = u_1 - A\omega\sin(\omega t) \tag{3.15}$$

$$u_2^* = u_2 \tag{3.16}$$

$$u_3^* = u_3 \tag{3.17}$$

one can replace velocities in the inertial frame with velocities from the non–inertial frame. The equation 3.13 becomes:

$$\frac{\partial u_i^*}{\partial t^*} + A\omega^2 \cos(\omega t^*)\delta_{i1} - A\omega \sin(\omega t^*)\frac{\partial u_i}{\partial x_1^*}$$
$$+ u_j^*\frac{\partial u_i^*}{\partial x_j^*} + A\omega \sin(\omega t^*)\frac{\partial u_i^*}{\partial x_j^*}\delta_{j1} \tag{3.18}$$
$$= -\frac{1}{\rho}\frac{\partial p}{\partial x_i^*} + \nu\frac{\partial^2 u_i^*}{\partial x_j^{*2}}$$

Equation 3.14 becomes:

$$\frac{\partial u_j^*}{\partial x_j^*} = 0 \tag{3.19}$$

The third and the fifth term in 3.18 cancel out and if we assume that

$$p^* = p + \rho A\omega^2 x \cos(\omega t^*) \tag{3.20}$$

the transformed Navier–Stokes equations for the motion in a non–inertial system are

$$\frac{\partial u_i^*}{\partial t^*} + u_j^*\frac{\partial u_i^*}{\partial x_j^*} = -\frac{1}{\rho}\frac{\partial p^*}{\partial x_i^*} + \nu\frac{\partial^2 u_i^*}{\partial x_j^{*2}} \qquad i,j = 1-3 \tag{3.21}$$

The continuity equation already takes the transformed form in 3.19.

Hence, the motion in a non–inertial frame is governed by the same equations as that in an inertial frame, but with a modified pressure field. The solution of the two sets of equations (i. e. in the inertial and the non–inertial frame) *will be the same if boundary conditions are entirely placed on velocity but not on the pressure.* If $\rho = \rho(p)$, then the modification in the pressure terms changes the inertia terms. Since the present study concentrates on the velocity fields only, it is expected to give results that are applicable to the oceanic wave boundary layers without any modifications.

On the other hand, if it is desired to study force fields or sediment transports then the oscillatory bottom flows cannot be considered reliable. The pressure gradient forces of the two cases are different, and hence the oscillatory boundary-layer experiments should not be used in studies involving fluid forces.

3.2 PREVIOUS EXPERIMENTAL WORK ON WAVE (OSCILLATORY) BOUNDARY LAYERS

There are a large number of studies on the wave (oscillatory) boundary layers with diversified aims. However, the common experimental installations that have been used were the U–tube (or the oscillatory–flow water tunnel) and tanks with the oscillatory bottoms (plates) and pertinent results will be reviewed in this section.

The first detailed experiments with oscillatory bottoms were done by Kalkanis (1964). He solved the linearized equations of turbulent fluid motion with a constant eddy diffusivity and performed detailed measurements of the mean velocity profiles for the case of two– and three–dimensional bottom roughnesses. The two–dimensional roughness consisted of bars (of different shapes) placed along the bottom in the direction perpendicular to the oscillations. The three–dimensional roughness consisted of single cube-shaped elements individually placed at the bottom. Kalkanis (1964) found that the critical Reynolds number based on the roughness necessary for the transition to turbulence is smaller in the case of three–dimensional roughness. He modeled the sediment transport rate based on the mean velocity profile obtained by experimental measurements and the validity of the model was verified by fitting experimental data to his model. Jonsson & Carlsen (1976) conducted measurements of turbulent velocity profiles and gathered more information on turbulent properties. This was the first detailed and precise LDV measurements of turbulence in the oscillatory boundary layers, which enabled the calculation of the integral–momentum shear

stress distribution, assuming a logarithmic velocity profile with phase–dependent friction velocity. Simple models for the thickness of the boundary layer and wave friction factor were also derived. The velocity, integral shear stress and eddy viscosity were presented as functions of the distance from the bottom and phase of oscillations. For the first time, negative eddy viscosities were reported and their explanation was that "the shear stress has inertia", or in other words, there is a phase leg between different vertically spaced layers in the fluid. Jonsson (1980), while providing a detailed overview of experimental work, presented some new results obtained in an oscillatory water tunnel. Based on the experimental results, the logarithmic velocity profile was modified to include a phase lead between the layers. This phase lead was comment in the overlap layer, which was observed to exist only for large A/k_s. A modified expression for the calculation of friction factor was provided and some suggestions were also made for three–layer viscosity model.

Du Toit & Sleath (1981) studied flow over self–formed and artificially placed ripples in tanks with an oscillating bottom tray and an oscillating water tank, using LDA measurements. The focus was the change of fluctuating, mean and rms–velocity above the rippled bed in the turbulent boundary layer flow. Hino, Kashiwayanagi, Nakayama & Hara (1983) did first detailed studies on the structure of turbulent eddies in an oscillatory flow using the wind tunnel. They studied the profiles of mean velocity, turbulent intensities, Reynolds stress, and turbulent energy production in accelerating and decelerating phases. Power spectra and spatial correlation measurements indicated high energy dissipation in the decelerating phases. A special attention was given to the bursts and ejection of the fluid from roughness elements. They observed that the coherent structures were built up in a short time. The velocity fluctuations increased in the decelerating phases of the flow, followed by the "bursting" in the wall boundary layer that causes the decrease of the fluctuations to a minimum. The

acceleration phase was characterized by small high–frequency turbulence fluctuations. Further fundamental investigations on turbulence in oscillatory flow were carried on by Sleath (1987) using an oscillating water tunnel. This excellent experimental study had several significant conclusions. Sleath (1987) obtained logarithmic velocity profiles in the immediate vicinity of the bed and studied in detail the distribution of turbulent intensities, Reynolds stresses, integral–momentum stress, eddy viscosities and mixing lengths. He emphasized that the Reynolds stresses are approximately ten times smaller than the stresses obtained from the integral–momentum equation. Also, he reported negative eddy viscosities very close to the bottom. With respect to turbulent structure, he discussed the appearance of jets and bursts, and the ejection of the fluid from the roughness elements at the end of each half–cycle, that was used to explain the appearance of negative eddy viscosities.

Jensen, Sumer & Fredsøe (1989) studied the structure of turbulent OBLs for high Reynolds number flows up to $Re = 6 \times 10^6$. They detected the formation of the logarithmic (overlap) layer for high Reynolds number at the phase $\omega t \approx 15^o$, and this transitional phase was lower for higher Re. They also found that the turbulence quantities normalized by the inner flow parameters and averaged over half–cycle corresponded to a steady boundary layer distributions, but significantly depended on the ratio of amplitude to bottom roughness A/r. Systematic measurements were also performed to obtain the dependence of the wave friction factor on the Reynolds number.

Excellent overviews of experimental and theoretical modeling of wave boundary layers can be found in publications of Sleath (1995), Nielsen (1992), Fredsøe & Deigaard (1992), Grant & Madsen (1986), Nielsen (1984), Sleath (1984) and Jonsson (1980). More recent research in this subject appears to be moving towards the wave–current boundary layers. In general, field measurements showed that currents,

besides the waves, play an important role in the dynamics of coastal flows as well as on the sediment transport over continental shelf. The difficulty of the studies on wave–current boundary layers is exacerbated by the paucity of the knowledge on mechanisms coupling the waves and currents.

3.3 PREVIOUS EXPERIMENTAL WORK ON WAVE–CURRENT BOUNDARY LAYERS

As noted, there have been only a few experimental investigations on the interaction between a steady current and oscillatory motion. The need for various experimental data cannot be overstated for improved understanding of this interaction. It has been argued, moreover, that the further development of numerical models in this context depends on extending our understanding of the relevant physics.

Reniers, Battjes, Falqués & Huntley (1997) conducted laboratory experiments in a wave basin 40 m long and 25 m wide. The basin was arranged to have a beach at an angle to the wave generator as to enable the observation of instabilities of wave over a wide region of the basin. The aim was to perform spectral analyses in the frequency and longshore wavenumber domain, and to develop simple models that can describe the experimental data. They have found that there is a significant influence of the beach profile on the development of shear instabilities. The wavenumber range for those instabilities can be reproduced by their numerical model.

Kemp & Simons (1982) performed experiments in a long channel with steady current and waves were propagating in the same direction (see figure 3.2). They studied the flow over the rough and smooth boundaries and showed that the "linear superposition" of the waves and currents to predict the combined flow is untenable. The measured velocities near the bottom were larger and in the outer flow, were smaller, than in that predicted by the simple linear superposition between wave and

current velocities obtained if one or the other is absent. For the case of a rough boundary, the velocities were less than that predicted by the linear superposition, the reason being the formation of vortex structures at the top of the roughness elements. They observed that, within two roughness heights, the turbulence characteristics are dominated by the periodic motion, as predicted by Grant & Madsen (1979) for the wave dominated sublayer. Also, the maximum turbulent intensities and Reynolds stresses were as high as three times the values of the current alone. Kemp & Simons (1983) also studied the case where the waves are propagating in the opposite direction to the current. They showed that the interaction near the bed is not dependent on the relative directions of waves and currents, but the wave attenuation is increased by an opposing current and vice versa.

Several recent experiments have been carried out in several European Institutes. For example, Villaret & Perrier (1992) studied the transport of sand in the presence of waves and currents in a large wave flume (80 m long, 1.5 m high, 1.5 m wide). The velocities were measured by three ultrasonic velocimeters and concentrations were measured by optical turbidity probes. They found that waves significantly increase the apparent roughness height when compared to physical roughness. Also, the mass transport by the oscillatory wave motion was found to be reduced when the wave direction oppose the direction of the mean current. Earnshaw (1996) studied, using the PIV technique, the kinematics of two–dimensional flow over rippled beds when the currents and waves have same direction of propagation. It was shown that apparent roughness is about twenty times larger than the ripple height. Ejection of vortices was also observed in this study and vortices were described by their circulation and radius.

Arnskov, Fredsøe & Sumer (1993) performed direct measurements (i.e., not via velocity profiles) of bed shear stress over a smooth bed for various combinations
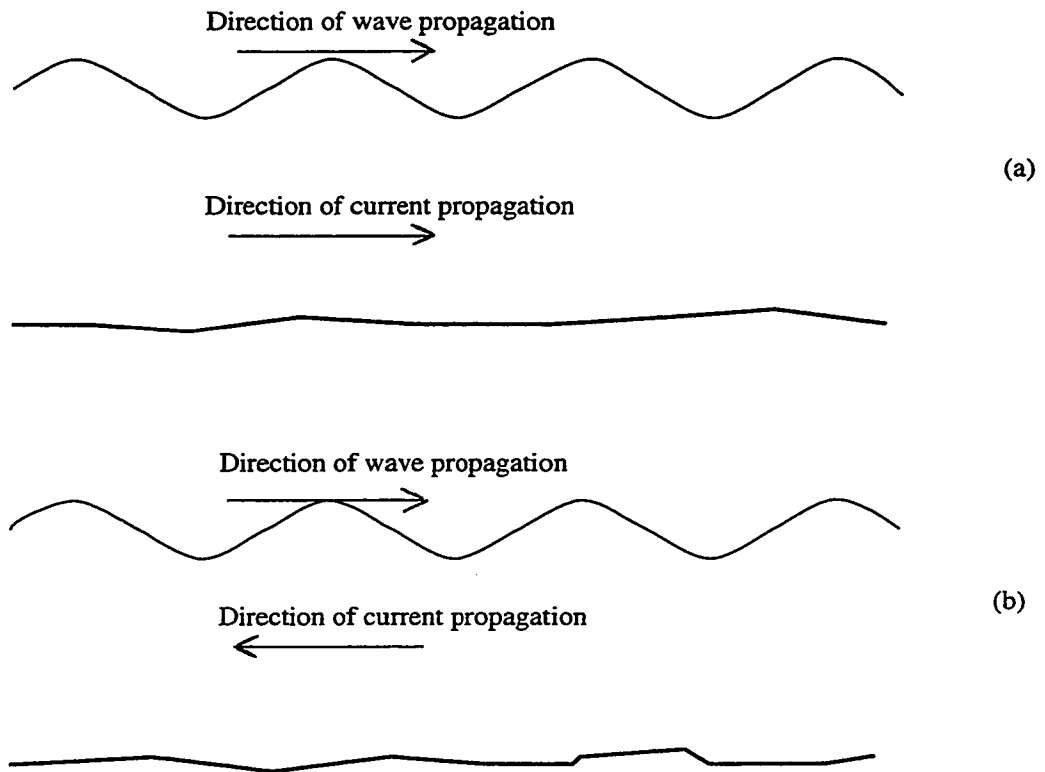
FIGURE 3.2. Directions of propagation of surface wave and ocean current: (a) same direction, (b) opposite direction.

of wave and current properties to understand the mechanism of interaction between waves and currents. The experiment was carried out in the wave basin (12.5×23.5 m), so that the waves and current can travel at arbitrary angles. Their studies confirmed the dependence of friction factor on Reynolds number in the laminar case and the logarithmic profile in the steady current case. A vigorous exchange of momentum was observed when wave influence on the current was strong. Thus, the bed shear stress is significantly increased in the case of a combined flow when compared to the case of the current alone. Arnskov *et al.* (1993) computed the apparent roughness and found it is dependent on the ratio of mean current and friction velocity, and A/k_s.

In particular, the increase of apparent roughness was proportional to the increase of U_m/u_*, and A/k_s, but they did not provide any models to explain the data.

Sleath (1990) measured velocity and bed friction in a steady flow flume with bed oscillating in its plane normal to the direction of the steady current. The Reynolds number of oscillatory flow component was not high enough that the effect of oscillatory motion on the steady current was negligible for the case of smooth bottom. The apparent roughness and bed shear stress were evaluated, and a poor agreement with the model of Grant & Madsen (1979) was noted.

Swan (1990) measured velocities in a long wave flume for different wave amplitudes and periods and observed the modification of the steady current profile by the wave induced flow. The variation of the current velocity profile with depth was a cause for the creation of additional vorticity. The measurement technique used, however, yields detailed information.

Brevik & Aas (1980) performed flume experiments on waves and currents over a rippled bed, when the waves propagate either in the same or opposite direction of the current. They developed a theoretical model to estimate the wave deformation when the waves are opposing the current. In their experimental study, the friction factor in the wave–current motion over the rippled bed was estimated. Their theoretical model showed reasonable agreement with data for the case when the direction of propagation of the waves and currents are the same. They also observed a reduction of the mean current velocity in the presence of waves, in a region close to the bottom. Therefore, the mean velocity in the wave–current boundary layer is smaller than that of the steady current boundary layer.

George & Sleath (1979) studied the superposition of a mean current and the oscillatory flow produced by an oscillating rough plate in the bottom of the apparatus. The working fluid was air and the bottom roughness consisted of closely packed

spheres. The flow was laminar in all cases, and the thickness of the steady boundary layer was larger in the case of rough bottom, due to the mixing produced by the jets and vortices ejected by roughness elements. In the case of combined flow, they reported the ejection of vortices from the top of roughness elements at the end of each half–cycle. Also, the linear vector superposition hypothesis to predict velocity components of the combined flow was found to be unattainable.

3.4 FIELD MEASUREMENTS

The most valuable data related to the physics of wave or wave–current boundary layers have been obtained via field measurements, which are unfortunately very rare. The reported field studies include those of Kontar & Sokov (1997), Signell & List (1997), Trowbridge & Agrawal (1995), Myrhaug, Slaattelid, Soulsby & Lambrakos (1995), Trowbridge & Kineke (1994), Evdoshenko & Lozovatski (1994), Madsen, Chisholm & Wright (1994), Madsen, Wright, Boon & Chisholm (1993), Slaattelid, Myrhaug & Lambrakos (1990), Lambrakos, Myrhaug & Slaattelid (1988), and Smith & McLean (1977).

Lambrakos *et al.* (1988) measured velocity profiles in the *Strait of Juan de Fuca*, which is a channel between the Vancouver Island and Washington State on the US–Canadian border. The range of tidal and wave velocities was 0.24–3.66 m/s and the measurements were fitted to the logarithmic velocity profile (see equation 2.24). The values of the friction velocity u_* and roughness y_o were studied as a function of wave and current velocities and bottom roughness. It has been found that, for the case of small wave activity or relatively pure current, the velocity profile matched the logarithmic law. For the case of large wave activity, the values of u_* and y_o are much larger and y_o increased by nearly 100 if the ratio of wave to current velocity becomes

2. For the same variation of the velocities ratio, the friction velocity increased by about 50%.

Slaattelid *et al.* (1990) measured the velocity profiles in the *North Sea* in the velocity range of 0.1–5 m/s. It was found that the logarithmic velocity profile is more accurately followed by the data for both, small and large wave activity. The value of y_o was found to depend on the angle between the waves and the current and, in general, this value was always increased by the wave activity (which contributed to the increase of the bottom shear stress).

Madsen *et al.* (1993) measured velocity profiles under extreme storm conditions in the coastal waters of North Carolina. They observed wave periods ranging 10–12 seconds and velocity amplitudes at the bed from 0.6–1 m/s. Using velocity profiles, that were fit to the logarithmic law and using model of Grant & Madsen (1979), they found that the apparent bottom roughness was $k_s = 15d$, where d is the median grain size of the sand (sediments) placed on the bed. They also studied the suspended sediment concentration under movable flat bed conditions. On sequel study, Madsen *et al.* (1994) developed simple theoretical models for the prediction of longshore and crosshore suspended sediment transport rates in the region that is not affected by the influence of breaking waves.

Evdoshenko & Lozovatski (1994) carried the measurements at the coast of Western Sahara in a region 41×45 miles. The velocity fluctuations, temperature, density and salinity profiles were measured, in order to study the development of the bottom nepheloid layer (high turbulent zone or a region having several layers separated by sharp velocity gradient zones) at the steep continental slope. They found that there is a critical angle of slope over which this boundary layer does not exist.

Trowbridge & Agrawal (1995) performed measurements in the *Field Research Facility* in North Carolina and they observed the distortion of the mean current by

the waves. Although comparison of data with the model of Grant & Madsen (1979) was attempted, the measurements were not sufficiently extensive to accept or reject model.

Kontar & Sokov (1997) conducted measurements using autonomous self–contained instrument packages developed by specialized Russian institutions. The equipment were deployed at depths ranging from 730–6125 m at various places in the Atlantic and Pacific Ocean in order to study the bentic boundary layer velocity components and temperatures. They found that turbulence conditions in the bentic boundary layer are influenced by organized movements of coherent structures in the turbulent flow. These structures represent large eddies with periods from tens to hundreds of seconds and they are related to the global circulations in the oceans. Those organized movements were found to transport significant fraction of vertical flux of heat and momentum across the turbulent boundary layer.

3.5 SUMMARY OF PREVIOUS EXPERIMENTAL WORK

The major contributions of a variety of experimental and field investigations can be summarized as follows:

- Quantitative information has been gathered on turbulent oscillatory (wave) boundary layers, especially on velocity profiles, fluctuations, the bottom shear stress, and the friction factor. Major attempts have been made to correlate turbulence characteristics of unsteady oscillatory flow with the steady flow case by applying the logarithmic velocity profile and linearly varying eddy viscosity. Only partial success has been achieved since there are additional parameters defining the structure of the flow, such as A/k_s, $A\omega$ (see Jonsson (1980), Sleath (1987), Justesen (1988)).

- The basic understanding of the physics of the flow comes through observation of flow structures. Many authors (Jonsson & Carlsen (1976), Hino *et al.* (1983), Sleath (1987)) have observed that the coherent structures appear in a very short period of time and they reported the ejection of vortices and appearance of jets from the top of the bottom roughness elements. Those observations play a major role in defining the time and length–scales, especially in the context of studies on the interaction between waves and currents.

- Observations of the structure of the turbulent flow were used to explain the existence of negative eddy viscosity (Jonsson & Carlsen (1976), Sleath (1987)). However, still there is no consensus on how to define the eddy viscosity for oscillatory flow. It has been argued that the eddy viscosity cannot be treated as in the case of steady flow due to short time–scales of fluid–bottom interaction in oscillatory flows. Since eddy viscosity represents the link between the kinematics and dynamics of the flow, it is necessary to continue studies until a final conclusions can be made. This information will be extremely important for improving numerical modeling.

- Available results cannot give a clear understanding on flow characteristics due to existence of several governing flow parameters and their poor coverage in laboratory experiments. Therefore, the continuation of research should lead to the definition of appropriate length–scales and to the exact dependence of turbulent properties on outer flow parameters. This is imperative if the laboratory experiments are to be extrapolated to real ocean conditions.

- Early studies on wave–current boundary layers included the velocity and bed shear stress measurements for the case when the wave and current propagate in the same direction (George & Sleath (1979), Kemp & Simons (1982), Kemp &

Simons (1983)). The aim was to determine the importance of non–linear effects and to prove that the simple superposition cannot be applied.

- To simulate the real ocean environment, several laboratory experiments have been performed in large wave basins (Reniers *et al.* (1997), Arnskov *et al.* (1993)). Again, only velocity measurements have been made.

- So far, experimental studies on wave–current boundary layer have yielded insufficient information on turbulent properties and their relation to the outer flow parameters, the scaling of flow parameters and the importance of different time. and length–scales. Also, no reliable information exists on the relation between the dynamics and kinematics of flow field (eddy viscosity).

- Many authors have resorted to the theoretical model of Grant & Madsen (1979) (for example Arnskov *et al.* (1993), Sleath (1990)), although the experimental data were insufficient to verify the validity of the model.

- The field measurements strongly support the existence a logarithmic layer for mean velocity and its distortion by wave motion. Furthermore, it was observed that the effective bottom roughness and bottom friction significantly increase in the presence of combined flow.

CHAPTER 4

EXPERIMENTAL PROCEDURE

The present experiments were carried out using the two different installations a short tank to study oscillatory boundary layers (OBL) and a long tank to study OBLs and current interactions. The measurements were made using Particle Tracking Velocimetry (PTV) and Laser Induced Fluorescence (LIF) was used for flow visualization. The description of the facilities, measurement techniques and experimental methods are systematically presented in this chapter.

4.1 DESCRIPTION OF THE SHORT TANK

The experiments were conducted in a Plexiglas tank of rectangular cross section $(1.5 \times 0.5 \times 0.29m)$ as shown in figure 4.1. The test section $(1 \times 0.39 \times 0.29m)$ comprised of a Plexiglas plate, with roughness elements milled on to it, located below a homogeneous water column. The plate was mounted on to a smooth belt drive resting on a false bottom and capable of performing oscillatory motions according to $U_p = U_o sin(\omega t)$. One of the two pulleys of the belt drive was driven by a vertical sprocket-belt arrangement, via a stepping motor controlled by a *DAS–16* data acquisition board. All the belt drives were pre-tensioned by the adjustment of pulleys and by using an auxiliary tension pulley to ensure minimum slip. The test cell was isolated from the surrounding gadgetry of the driving mechanism. Carefully designed openings at the two lower ends of the test–section allowed the belt to communicate with the driving mechanism. Also, these openings reduced the build up of fluid at the edges of the plate and the reflection of accumulated fluid from the end walls during oscillations. At the end of each cycle, high momentum fluid moving with the plate enters and diffuses within two end chambers (water columns) that enclose pulleys. Extensive

flow visualization performed by dye injection at various locations showed that the end effects due to finite size of the oscillating plate are suitably damped by the end chambers and no strong secondary flows are present in the parameter ranges covered.

The working fluid was filtered salt water of density 1030 kgm^{-3}, thus facilitating the suspension of Pliolite particles (of diameter $100-150\ \mu m$) that have the same density. Systematic flow visualization was performed using the standard Laser–Induced Fluorescence (LIF) technique by illuminating the long axis of the tank with a sheet of laser light and by interspersing fluorescent dye between the roughness elements. The dye dispersion patterns elicited the nature of flow structures emanating from roughness elements. The movements of these particles were video recorded to extract velocity information via Particle Tracking Velocimetry (PTV). This technique has been successfully used in many previous studies for whole–filed velocity measurements (see Drayton (1993), Srdić (1998)). Velocity measurements were performed in a $10 \times 12\ cm$ window, aligned with the long axis of the tank with its lower boundary coinciding with the top of roughness elements (all distances y were measured from this level). This window was illuminated by a $0.5\ cm$ thick light sheet emitted by a $500\ W$ halogen lamp. In order to suppress the reflection of light, the roughness elements and back side of the test–section were painted into black.

The input parameters of the computer code which controlled the stepping motor were amplitude A and period of oscillations T. The accuracy of the amplitude of oscillations was controlled by the potentiometer whose voltage was read by the data acquisition board. The maximum amplitude of oscillations which can be achieved by this installation was $17.5\ cm$. After the calibration of the output amplitude and period of oscillations, it was determined that maximal relative error for the amplitude was 4.4% and maximal relative error for the period of oscillations was 15% corresponding for the very short period of oscillations. The maximum error for the period seems
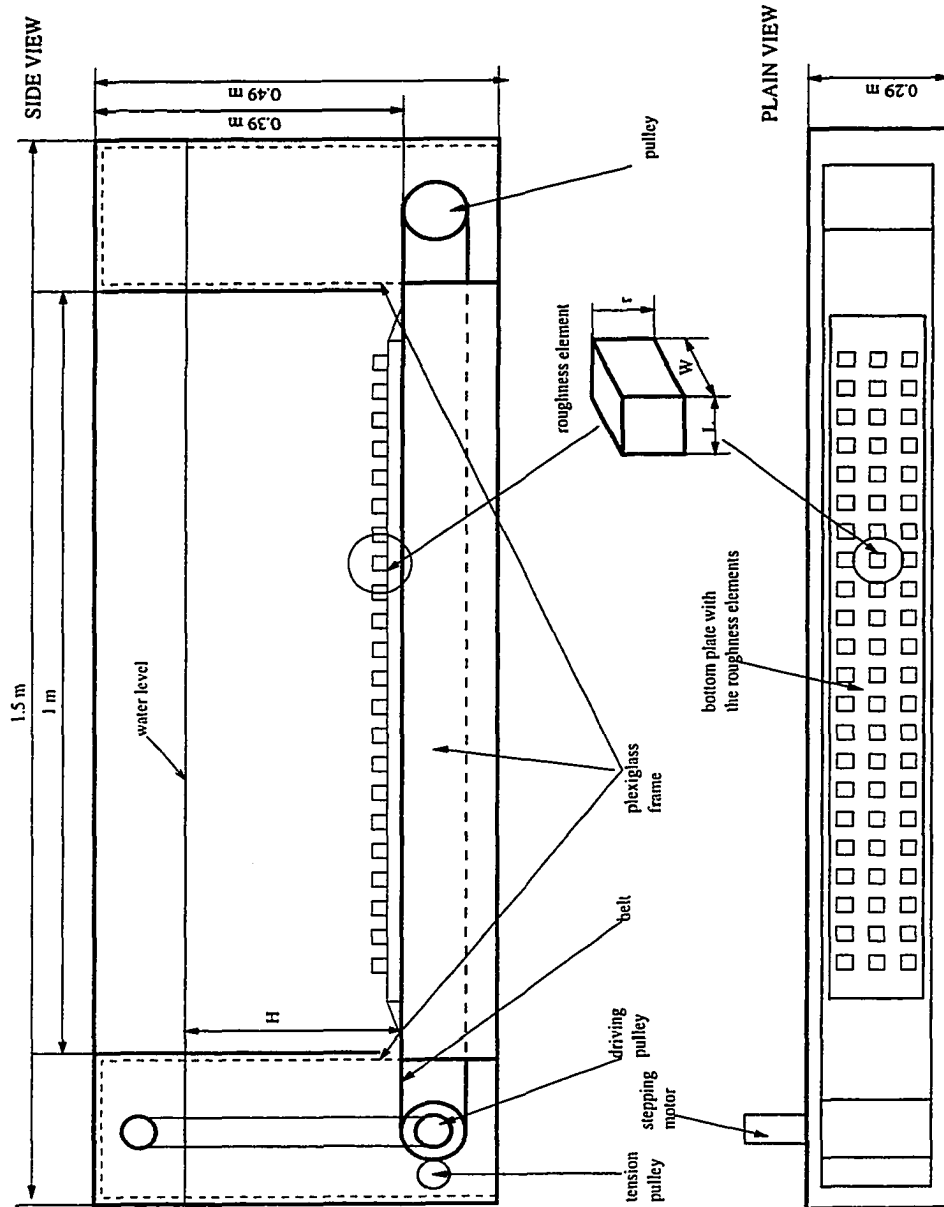
FIGURE 4.1. Short tank for wave (oscillatory) boundary layer studies.
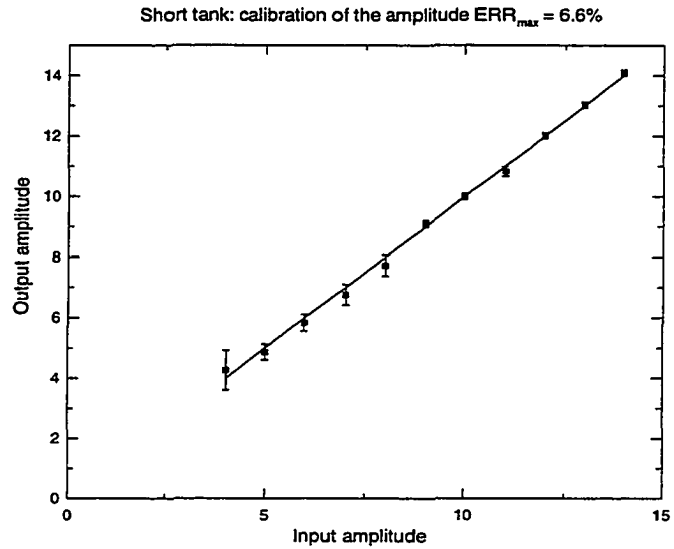
FIGURE 4.2. Calibration of the amplitude of oscillations of the plate in the short tank.
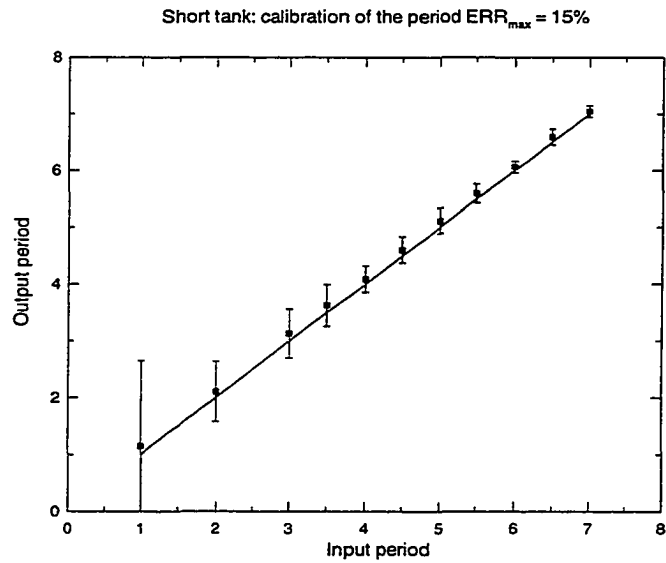
FIGURE 4.3. Calibration of the period of oscillations of the plate in the short tank.
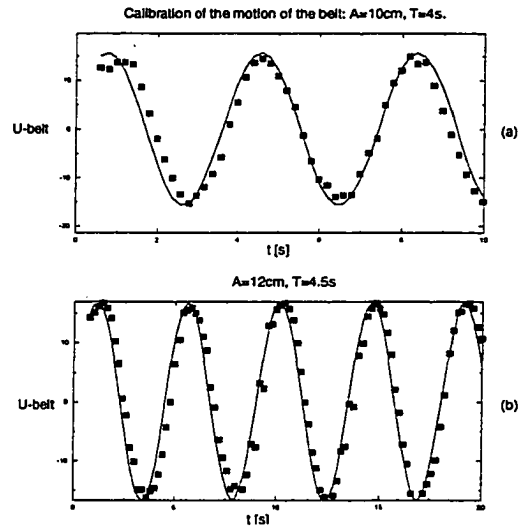
FIGURE 4.4. Calibration of the velocity of the bottom belt for the short tank: (a) A=10cm, T=4s and (b) A=12cm, T=4.5s.
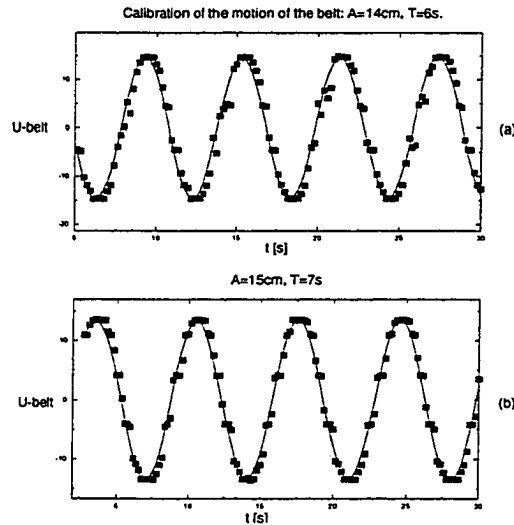
FIGURE 4.5. Calibration of the velocity of the bottom belt for the short tank: (a) A=14cm, T=6s and (b) A=15cm, T=7s.

to be high only for very short periods of oscillations. However, the average relative error for the period of oscillation was 6.5%. Calibration curves are shown in figure 4.2 and figure 4.3. The relative errors were averaged over 20 periods of oscillation for the each value of amplitude and period of oscillations. The calibrated amplitude values were 4-15 *cm* and period of oscillations values were 1-8 *s*. Furthermore, it was necessary to calibrate the motion of the belt, in order to confirm its sinusoidal motion. The calibration was obtained by particle tracking technique, following the motion of several "particles" attached to the belt. The "particles" were firmly attached to the belt and thus the velocity profile of the belt is the same as velocity of those "particles". Their velocity of the belt is presented in figure 4.4 and figure 4.5. It can be seen that the motion of the belt follow the sinusoidal motion fairly well for the range of amplitudes and periods which will be used in the experiments.

The experiments were completed for the eight different roughness types (see table 4.1 and four different water depths. In this study, we used the three–dimensional calibrated roughness elements. The roughness elements were machined out of plexiglas plates and they were square in their shape. The distance between roughness elements was the same as their width W and length L (see figure 4.6). The rough plexiglas plate was firmly attached to the belt at the bottom of a test section. In order to avoid end effects due to the vertical sides of the plexiglas frame (see figure 4.1) and due to the ends of the rough plates, the measurements were done in the middle of a test section. The window which was observed changed with the experiments, but the maximum dimensions were 10 cm width by 12 cm height. The preliminary visualization of the flow showed that there are no end effects due to the vertical walls of the plexiglas frame. Also, preliminary experiments showed that there are some effects created on the ends of roughness plate for the cases of larger amplitudes. Thus,
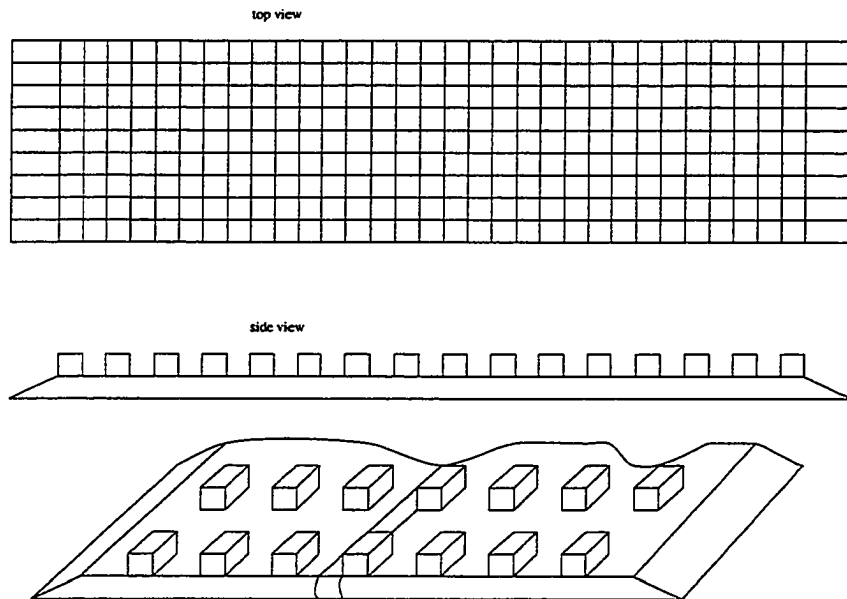
FIGURE 4.6. Roughness elements

Roughness Type	L [mm]	W [mm]	r [mm]
square el. (r1)	1.6	1.6	3.2
square el. (r2)	3.2	3.2	1.6
square el. (r3)	4.8	4.8	1.6
square el. (r4)	6.35	6.35	2.4
square el. (r5)	4.8	4.8	0.8
sand paper (r6)			0.8
square el. (r7)	4.76	4.76	4.76
square el. (r8)	3.2	3.2	6.35

TABLE 4.1. Dimensions of the roughness elements used in the short tank.

it has been decided that maximum amplitude that we could consider was 15 cm in order to get valid experiments.

4.2 DESCRIPTION OF THE LONG TANK

The long tank was used for the studies of wave–current boundary layers (to study OBL and current interactions). It was designed so that a steady, fully developed channel flow, approaches an oscillatory boundary layer and interacts with it in the test section. The schematic of the long tank is presented in figure 4.7 and a photograph of the tank is shown in figure 4.8. The tank is 6.78 m long, 0.31 m wide and 0.41 m deep, of which the sides are made out of plexiglas except the test section where glass sides were used. The tank was supported by an aluminum frame made out of angles and bars, placed outside the channel. The frame was carefully designed to avoid any deflection of the walls when the channel is filled with the water. The tank is placed on a robust steel frame, firmly supported by pretensioned chains to damp unexpected vibrations. The channel was constructed in modular form, consisting of four modules, to facilitate assembly and vibration isolation. The aluminum frame on the side and the steel frame under the channel were used to firmly connect four modules of the channel. The ends of the channels are connected to the feeder and receptor tanks that are used to deliver water to the channel via a water pump. These tanks are slightly wider than the channel and vertical plates were used to smoothly direct the flow towards the test section. Both end tanks have horizontal plates aligned with the bottom of the channel so as to weaken the jets of water coming or exiting the tanks. Also, a set of honeycombs were placed at the entrance to the central part of the channel to suppress the formation of large vortices.

The test section is 1.3 m long and is located 3 m from the entrance to the channel, allowing the flow to become fully developed before entering the test section. The bottom of the test–section was sunken in with respect to the bottom of the channel enabling the placing of oscillating mechanism for the bottom plate of test section.
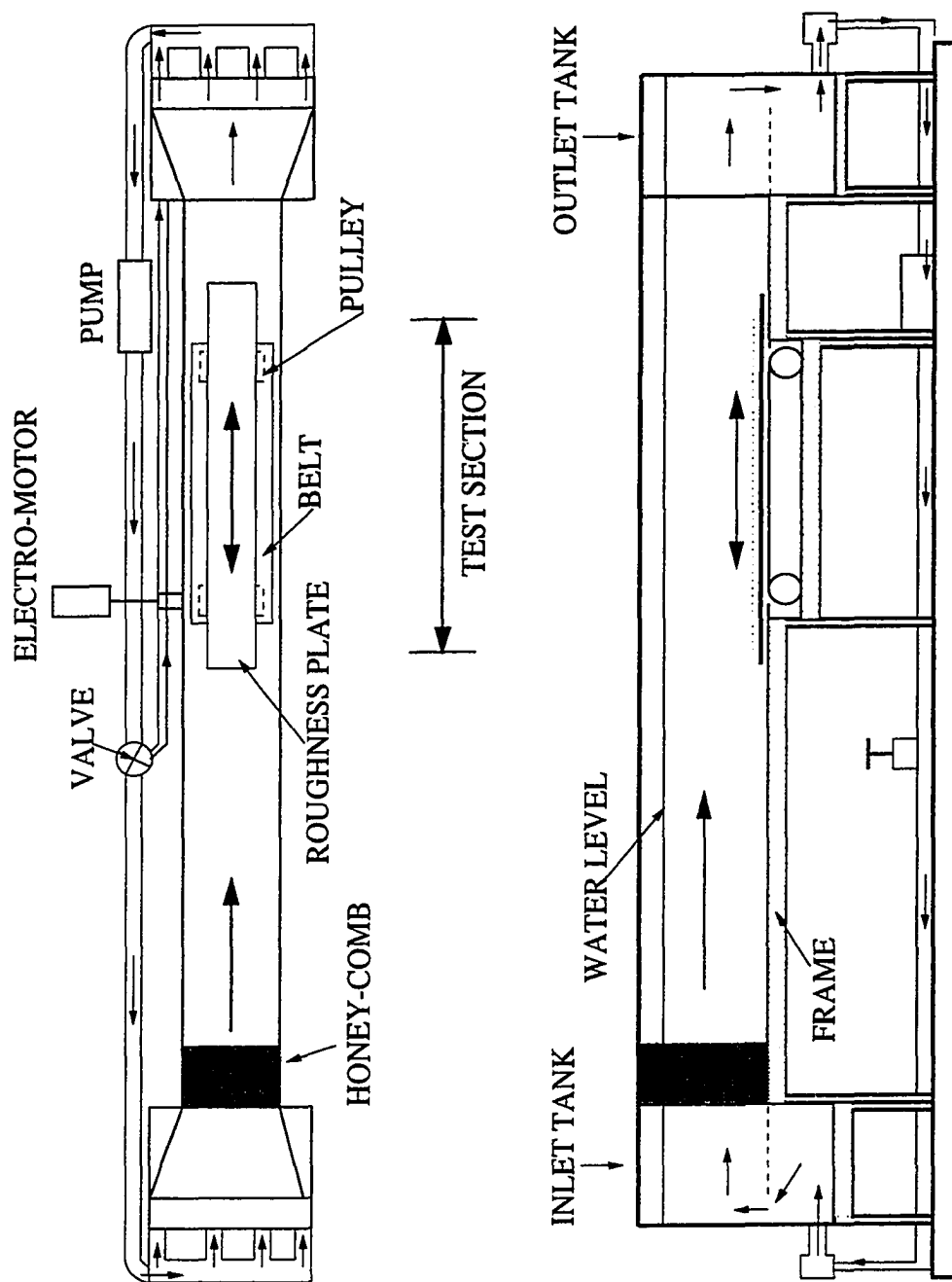
FIGURE 4.7. The details of long tank used for the wave–current boundary layer studies.

FIGURE 4.8. A photograph of the long tank.

Calibration of the amplitude for the long tank, $ERR_{max} = 2\%$

Calibration of the period of oscillation for the long tank, $ERR_{max} = 1.4\%$
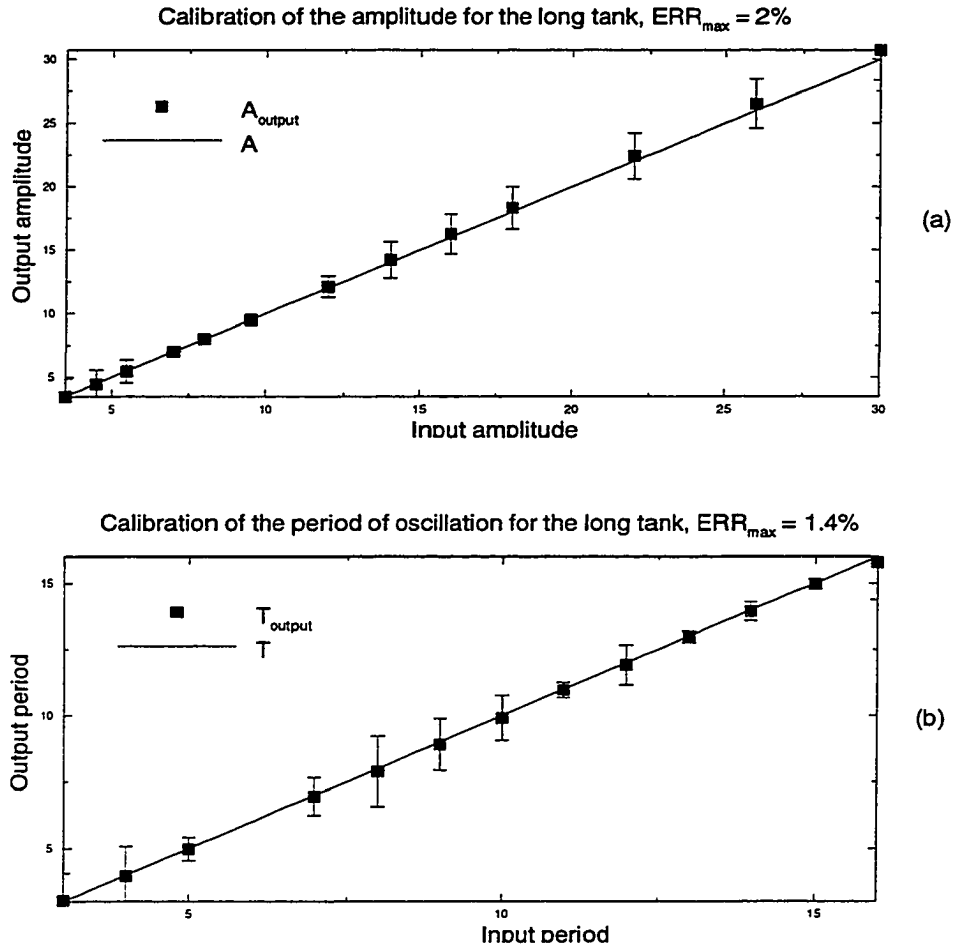
FIGURE 4.9. The calibration of the amplitude (a) and period (b) of oscillation for the long tank.
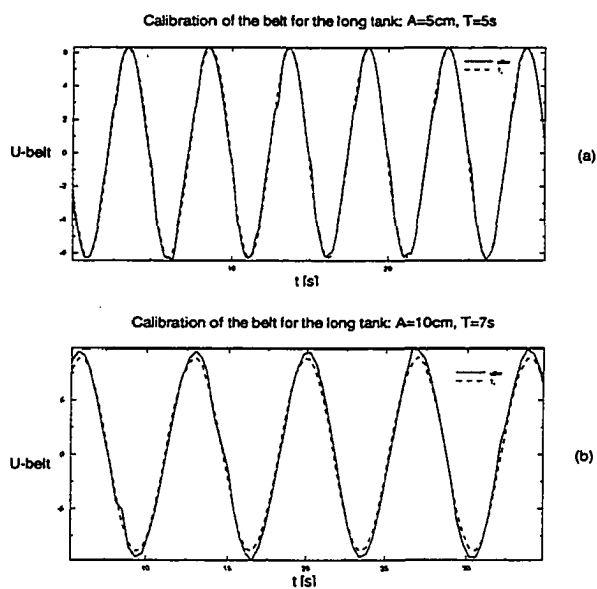
FIGURE 4.10. The calibration of the sinusoidal motion of the belt for the long tank:
(a) A=5cm, T=5s and (b) A=10cm, T=7s.
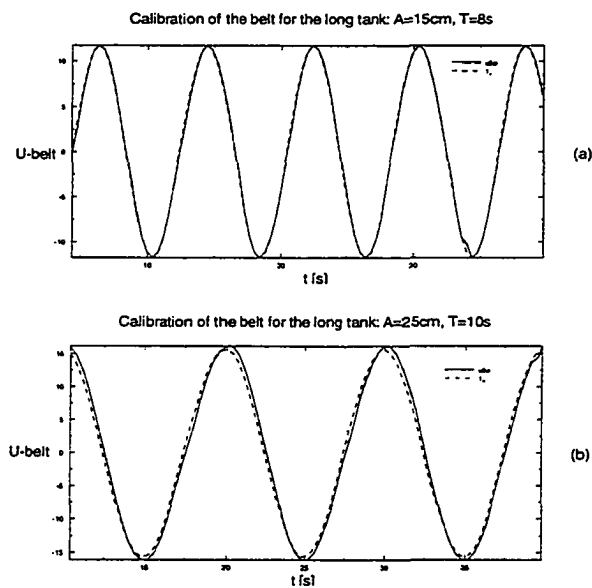
FIGURE 4.11. The calibration of the sinusoidal motion of the belt for the long tank:
(a) A=15cm, T=8s and (b) A=25cm, T=10s.

Roughness Type	L [mm]	W [mm]	r [mm]
square el. (r2)	3.2	3.2	1.6
square el. (r7)	4.76	4.76	4.76
square el. (r8)	3.2	3.2	6.35

TABLE 4.2. Dimensions of the roughness elements used in the long tank for wave–current boundary layer studies.

The plate with the roughness elements (figure 4.6) was firmly attached on the moving belt, and the experiments were performed with the three roughness sizes, listed in table 4.2. The roughness plates used were 1.2 m long in order to minimize any end effects. Again, the measurements were made only in the central part of the test section. The three roughness types are the same as those used in some of the experiments in the short tank; this enabled to reproduce similar bottom conditions for the case of steady, wave and wave–current motion.

The wave component of the motion was achieved by the oscillatory motion of the belt in the test section, while the mean current was obtained by water recirculation. The water was recirculated by the water pump of capacity of 300 gal/min, giving a mean current velocity in the range 5–12 cm/s (depending on the height of water level in the tank). The impeller (the rotor of the pump) was made out of iron, so that the experiments could be conducted with the fresh (tap) water only. The water was supplied to the pump via the receptor tank attached to the end of the channel. This was recirculated to the inlet tank through the pipe–line via the pump. The valve placed on the pipe–line was used to adjust the desired water flow. In order to prevent overheating of the pump, an overflow water–line was placed to return the excess water into the outlet tank. The water flow rate was measured by a flowmeter placed in the vertical pipe–line attached to inlet tank. The water enters the inlet tank in the form

of four separate weak jets rather than one strong jet. The inlet jets are broken using a horizontal plate placed in the inlet tank at the level of the channel bottom ("bucket effect"). Using a honeycomb placed in the inlet tank, it was relatively easy to produce an uniform flow in the central part of the channel.

The present apparatus was designed to study the interaction between the OBL and the current component only for the case where the velocity vectors of both components have the same direction. To broaden the studies to a more general case where the velocity components vectors have different directions, it would be necessary to employ a much larger installation or a square basin.

4.3 MEASUREMENT TECHNIQUES AND DATA ANALYSIS

4.3.1 Particle Tracking Velocimetry

Over the past years, numerous techniques have been developed for qualitative observations and quantitative measurements of fluid flow. Traditional visualization techniques were primarily qualitative, but the development of methods such as Hot Wire Anemometry (HWA) and Laser Doppler Anemometry (LDA) have opened up avenues to measure velocity fields with great accuracy. These techniques, however, have the disadvantage being able to make Eulerian measurements at only one point.

An alternative measurement technique is the Particle Image Velocimetry (PIV). In PIV, the flow is seeded with neutrally buoyant particles which are assumed to follow the streamlines without affecting the flow. The images of the fluid flow are recorded on some medium (film, video tape) and analyzed in order to determine how the particles move in time. So far, there are two methods that are used to gain information from successive images which contain individual particle tracks: image cross–correlation (used in PIV) and Particle Tracking. In the PIV, the image is divided in separate cells and the correlation function between cells in two successive time periods is

evaluated. Further, the velocity of the cell is evaluated from the cell translation based on an optimization of correlation function. In Particle Tracking Velocimetry, a time series of images, especially in the context of digital image processing, is recorded and a larger volume of information about positions of the particles as a function of time can be obtained. Therefore, the velocities can be recorded more accurately. Certainly, it is necessary to have a sampling frequency which is higher than the highest frequency of the particle motion. The accuracy of the particle velocities is limited by the accuracy to which the individual particles are located and the time period over which velocity could be reasonably evaluated. Also, the spatial resolution of particle tracking techniques depends on the number of particles in the flow: the higher number of particles, the higher the resolution.

The present studies were conducted using the two–dimensional Particle Tracking Velocimetry (PTV) Technique based on the DigImage software developed by Dalziel (1992).

System components

The software of the particular PTV system used is composed of two parts: DigImage and Trk2DVel. DigImage has ability to do general image processing and two–dimensional particle tracking. Trk2DVel is a post–processor which calculates statistics of the flow from particle tracking files.

In DigImage, the hardware is connected as shown in figure 4.12. The image observed by the standard monochrome camera (COHU 4910 with 50 mm COSMICAR lens) is recorded by a Panasonic AG–7350 NTSC Super VHS video tape recorder and it can be simultaneously seen on a RGB SONY monitor. The video recorder was fitted to a PC Pentium computer via a modified RS–232 interface, allowing the complete computer to control all video functions. The frame capture is achieved by a Data
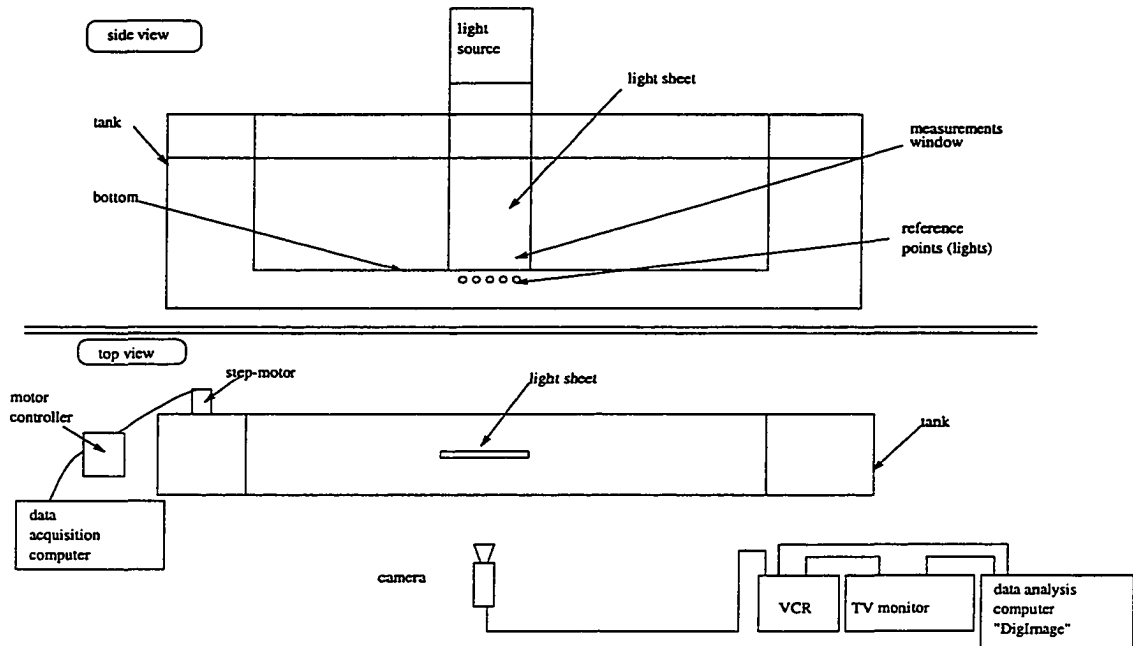
FIGURE 4.12. The experimental arrangement used for the Particle Tracking Velocimetry.

Translation (DT–2861) video frame–grabber with 16 buffers on board that digitizes 480 lines with horizontal resolution of 512 pixels per line. The maximum framing rate of the system is 30 frames per second (or 30 Hz), since it is NTSC based.

Since the sampling frequency of this system is rather low, the system is unsuitable for the analysis of flow with a very high Reynolds numbers. The spatial resolution is imposed by the video system only in the case when the particles are smaller than the resolution length. In the present experiments, this is not the case and the resolution is imposed by the size of tracking window and number of particles detected within that window.

4.3.2 Justification for the use of Particle Tracking Velocimetry

There are three issues that should be discussed in relation to the application of this particular particle tracking system: time resolution, spatial resolution and particle characteristics as a tracer.

The main limiting factor is the low sampling frequency of the particle tracking system which, at times, cannot resolve the smallest time–scale of turbulence (Kolmogorov scale). According to preliminary experiments, the typical $u_{rms} = 0.15U_o$ and the thickness of the boundary layer is on the order of 10 cm. Assuming the highest velocity to be 15 cm/s (in most experiments the maximum velocity was around 12 cm/s) and integral length–scale to be of order of the boundary layer thickness, the dissipation of turbulent kinetic energy can be calculated as:

$$\epsilon = \frac{u_{rms}^3}{L} \approx 1.139 cm^2/s^3 \tag{4.1}$$

Using $\nu = 0.01cm^2/s$, the Kolmogorov time scale was calculated to be $T_k = 0.094s$, which is larger than the sampling time step of 0.033 s. The smallest scale of turbulence was determined to be $L_k = 0.031cm$, being of the same order of smallest spatial resolution of the system. The size of window in most experiments was approximately 10–14 cm high and, with 480 vertical lines per image, the smallest resolution was approximately 0.025 cm. Therefore, for the range of velocities (Reynolds numbers) used in this study, the PTV technique has satisfactory sampling frequency and spatial resolutions.

It should be noted that the spatial resolution of the tracking system is not the same as the velocity field. The resolution of the velocity field depends on size of the tracking window, number of particles detected and number of grid points distributed within the window. This resolution changes from one experiment to another and it is obtained

through post–processing of data. In most experiments, the vertical resolution of velocity data was 0.1 cm. More details about each particular experimental setup, resolution and procedure will be given later.

Tracer particles

The tracer particles used in the present study were made of Pliolite VT (Vinil-toluene–butadiene copolymer). These are white particles, supplied in granular form with specific density of 1.03. These particles have an excellent reflectivity which satisfies optical criteria for Particle Tracking Velocimetry.

Hydrodynamic criteria which should be satisfied by the tracer particles are:

- The particles should be close to a spherical shape – which is satisfied by the Pliolite particles used.

- The particles should be neutrally buoyant. In order to obtain neutrally buoyant particles it was necessary either to add a proper amount of salt or reduce the particle density. More details about reducing of the particle density will be given in the following section.

- The size of the particle must be smaller than the smallest length–scale of the flow. The size used in the present experiments was 100–150 μm. Since the Kolmogorov length scale was estimated to be $L_k = 0.031cm$, this criterion is satisfied.

- The particle response time must be smaller than the smallest time scale present in the flow. From the equation of motion of particle in a fluid (see Srdić (1998)), it is possible to determine the particle response time as:

$$t_p = \frac{d_p{}^2(1 + C_m)}{18\nu} \tag{4.2}$$

Using $\nu = 0.01 cm^2/s$, $d_p = 150 \mu m$ and $C_m = 1.5$, the typical response time was estimated to be $t_p = 0.0075s$, which is smaller than the Kolmogorov time scale $T_k = 0.094s$.

Therefore, the use of Pliolite particles as a tracer for the PTV technique is justified.

4.3.3 Particle Tracking procedure

Particle Tracking using DigImage software has three major stages: experimentation, tracking and subsequent data analysis.

Experimentation

In order to perform successful experiments using PTV technique, it is necessary to conduct the following technical preparations:

- *Contrast.* The particle tracking technique requires a good contrast between the particles and the background. This is achieved using a thin and powerful white light sheet (≈ 0.5 cm thick). The contrast is usually enhanced by providing a black background while the unnecessary reflection is minimized by providing black bottom surface. This can be achieved by simple painting or using the black–contact paper.

- *Particle preparation.* The Pliolite particles need to be pre–wetted before they are suspended into a flow; otherwise, they float on the water surface. The mixing of particles with water should be done in a clean beaker. The particles are placed in the beaker and hot water volume of 10 to 20 times that of the particles should be added (because it contains less dissolved air). In addition, it is necessary to add a few drops of photographic wetting agent (dish–washing soap also works). The particles should be left in water until all of them sink from

the surface. To reduce the density of particles to make them neutrally buoyant in fresh water it is necessary to boil particles so that they can absorb water and reduce their bulk density (recommended by Dalziel (1993)). Alternatively, salt water that matches the density of particles, can be used.

- *Reference points related to the calibration of the system.* The PTV software requires several permanent reference points which are used for the mapping between images and physical space. Physically, they are small lights (LED diodes, in this case) placed close to the window chosen for flow tracking. The easiest way to make reference points is to cover a portable neon–light by the black contact–paper and make small round holes (1–2 mm in diameter). For more details on mapping and usage of reference points see Dalziel (1993).

- *Recording of experiments.* A camera with an appropriate lens should be zoomed at the window and reference points. Individual particles should be clearly distinguished from the background and be seen as approximately round (spherical) objects. For the cases of high velocity flows, it is sometimes recommended to defocus the camera in order to avoid elliptical image of the particle in motion.

- *Physical grid.* Depending on the type of flow, the physical grid can be recorded prior or at the end of the experiment. The easiest way is to make a grid out of a thin plexiglas plate, so that the grid lines (grooves) are accurately spaced with a distance of 1 or 0.5 cm (in), in both horizontal and vertical directions. The grid needs to be placed in the middle of the light sheet to record the images. Those images were used for the definition of a coordinate system in the chosen units (in, cm) rather than in pixels.

Particle Tracking process

The particle tracking process uses DigImage software and has a couple of phases:

- *Calibration of the system* consists of the determination of reference and calibration points and the recording of audio signals on the tape using video recorder audio channel. Choice of reference points determines the reference image space while calibration points defining the physical space. Audio signals were used for the accurate positioning of the tape during the PTV process. These three steps are used for the one–to–one mapping between image space and reference image space and mapping between the reference and physical physical image spaces.

- *Determination of parameters* such as the particle size, size of the tracking window, the period between two frames used for tracking, maximum matching distance, maximum RMS error for mapping, time of tracking, determines the quality of results. The optimum set of parameters depends of the type of the flow studied and should be determined by operators experience.

The particle tracking is an automatic process and, once the parameters are defined, computer positions the tape and acquires 16 images. The images are checked for errors in mapping, images are rejected if the mapping is inaccurate (larger than specified errors). When the error criterion is satisfied, the software locates the particles, performs tracking in time, record particle position, time and two velocity components. The whole process is repeated until specifications for tracking are completed.

Data analysis

The subsequent analysis of data is performed by the software Trk2DVel. Trk2DVel is capable of reading DigImage files and extracting velocities of particles in time. Several options are available for this procedure. The most used in the present study was the

creation of a rectangular grid with respect to which the distribution of velocity in two–dimensional domain is determined (Eulerian velocity field). This option allows a choice for the number of grid points in horizontal and vertical direction. If the experiments are conducted with a large number of particles, it is possible to get very good spatial resolution (distance between grid points less than 0.1 mm). Using this method is very important, especially if one needs to measure the velocity near the surface. Usually, it is advised that the surface should not be a part of a window where the tracking takes place.

While obtaining the rectangular grid, the user is asked to specify the type of velocity that should be extracted: mean, fluctuation or instantaneous velocity. The raw instantaneous velocity files obtained by Trk2DVel were used for data analysis suited for current research problems and calculation of specific turbulent properties.

4.3.4 Suitability of Particle Tracking techniques for present studies

Laboratory studies on the topic in point were mostly based on such laboratory techniques as Laser Doppler Velocimetry – LDV (see Perry, Lim & Henbest (1987), Kemp & Simons (1982), Kemp & Simons (1983), Sleath (1987) and many others), Hot Wire anemometry – HWA (see Hussain & Reynolds (1975), Kim, Kline & Reynolds (1971)) and Hydrogen Bubble Technique (see Grass (1971)). LDV and HWA have excellent frequency response and offer possibility of measuring two or three velocity components. However, LDV and HWA give velocity data only at one point at a given time, and the obtaining the vertical distribution of the velocity components requires the translation of the measurement volume. Still, it is not possible to obtain the whole picture of the flow by these techniques without using certain assumptions for the flow behaviour (homogeneity in horizontal direction for wave boundary layer, for example).

Recent studies, especially on wave–current boundary layers, have focused on more detailed qualitative and quantitative information on the flow, which requires simultaneous measurement of velocity at many locations, at least in a two–dimensional plane. PTV and PIV are the only methods available to obtain such information (see Earnshaw (1996)). In the present study, we take the advantage of DigImage that allows the measurement of velocity in a two–dimensional physical space as a function of time. Recording experiments during a large number of cycles, we were able to decompose instantaneous velocities to mean, periodic and fluctuating components. The two–dimensional swath of velocity in the measurement domain gives information about the changes of variables in horizontal direction, while helping us to better understand complicated physics of those specific boundary layer problems.

4.4 EXPERIMENTAL PROCEDURE

The experimental procedure was very similar in all experiments: steady current, oscillatory and superposition of previous two. An exposition of the experimental procedure will be given for the case of oscillatory (wave) boundary layer experiments, followed by a discussion on how the steady current and wave–current experiments differ from that procedure.

4.4.1 Experimental procedure for oscillatory boundary layer experiments

The experiments on oscillatory (wave) boundary layers were performed in the short tank (see figure 4.1) using salt water (of specific gravity 1.03) as the working fluid. The tracking particles were prepared, as was discussed in the previous section, and mixed with salt water in the tank. A proper amount of particles was chosen by trial and error. The water in the tank was stirred and left to settle until all motions disappeared. A light sheet was placed in the center of the tank and all equipment was

turned on. Further, it was necessary to turn off the lights and to determine proper magnification, apperature and position of the camera with respect to the desirable window of tracking. In order to ensure the presence of a large number of particles, several images were acquired by the DigImage directly from the camera. These images were used for particle counting. The typical number of the particles for a 10×10 cm window was approximately 2000-2300. When the trial images were satisfactory, the grid was recorded, illuminated by the light sheet. The grid was immersed in water under the light sheet and an image was recorded for several seconds. Upon removal of the grid from the tank, it was necessary to wait for the decay of motions in the tank before actual experiments were started.

Immediately before the experiments, the desired amplitude and period of oscillations values were programed to the stepping–motor driver. The room was then darkened and the motion of the belt was started and left to reach quasi–steady state, which usually happened after a few cycles. After quasi–steady state was reached, the images were recorded on a video tape for at least 20 cycles of oscillations. After the completion of an experiment, the motion of the belt was stopped and the motions in the tank were allowed to decay before another experiment was started.

4.4.2 Experimental procedure for steady current experiments

The experiments on steady current boundary layers were carried out in the long tank (figure 4.7). The tank was filled with the fresh (tap) water prior to the experiment until the desired height was reached. The roughness plate was attached to the bottom of the test section, i. e. belt which was stationary for the case of steady current experiments. When the tank was filled in, the pump for the water circulation was started and the flow regulation valves were positioned in order to achieve the desirable flow rate through the channel. Therefore, the mean velocity was regulated by the

height of the water in the tank and the position of flow regulation valves. When the desirable flow rate was achieved, the particles for PTV (that have been previously cooked to soak the water and decrease its density) were added into the tank. Prior to achieving the steady state flow, the mapping grid was video–taped, as before. The water mixed with particles was circulated for another 20–30 minutes (determined by trial and error) to obtain steady state conditions and to allow for the decay of initial transients generated upon the start of the pump.

The flow in the test section was recorded in the windows 20 × 13 cm for about 70 seconds. Particle tracking was performed with 0.033 second step for a duration of 60 seconds, yielding 1800 samples of the two dimensional velocity field obtained by tracking of 1700–2000 particles. The two–dimensional velocity data were transponced on a grid with 20 nodes in the horizontal and 60 nodes in the vertical. The grid based Eulerian velocity field was obtained using the post–processing software Trk2DVel. Two output files were used: the file containing mean velocity data obtained by the averaging of 1800 samples and the file containing instantaneous velocities. Instantaneous velocities at a given moment, were obtained by averaging 10 images (averaging over 0.33 seconds). This averaging was necessary to avert the problem of insufficient data points contained in a single sample (image).

4.4.3 Experimental procedure for wave–current experiments

A set of wave–current experiments were conducted immediately after the steady current experiments to obtain the flow corresponding to the same bottom roughness and mean current. For one set of experiments, the flow was observed in the same window as in the case of steady current (therefore, it was not necessary to record a grid unless the setup of the camera was changed). The desired amplitude and period of oscillation were entered as input parameters for the program controlling the stepping–motor

and oscillations. It was relatively easy to obtain the quasi–state motion upon the imposition of oscillations on the mean flow as all disturbances created by the sudden start of the belt were carried away by the mean current. The images were recorded for 10–20 cycles of oscillations and the same process was repeated for different values of amplitude and period of oscillations.

About 1800–2300 particles were used for the tracking process, encompassing at least 10 cycles of oscillations. Post–processing by Trk2DVel gave the instantaneous velocity data on a grid of 20 points in the horizontal and 60 points in the vertical. The instantaneous velocities were obtained for 12 phases of the flow, separated by $\omega t = 30^o$ (i. e. $30^o, 60^o, ..., 360^o$). From the velocity data it was possible to obtain mean, periodic, instantaneous and velocity fluctuations. The mean velocity was obtained for each grid point by averaging 120 samples (12 phases $\times$ 10 cycles). The periodic velocity component was obtained using phase averaging of 10 cycles. The instantaneous velocities were obtained as before, but only using 3–5 instances (images) centering the phase of motion at which the velocity field is required. This large file was used to obtain periodic velocity component, which was achieved by phase averaging of 10 oscillation cycles. The third file represents the instantaneous velocity field within one cycle, corresponding to 12 phases. Thus, the post–processing of data gave us the instantaneous, mean and periodic component of velocity so that the velocity decomposition of Nielsen (1992) can be easily applied.

For all three types of experiments, the velocity data obtained by Trk2DVel were used as the input file for the software that calculates turbulent properties of the flow, such as, velocity fluctuations, u_{rms}–velocity, turbulent kinetic energy, velocity gradients, shear stress, integral length–scales, eddy viscosity, etc.

CHAPTER 5

EXPERIMENTAL RESULTS AND DISCUSSION

The research on the steady current boundary layers described herein was used as a verification tool for the design of the experimental apparatus (long tank), experimental procedure and measurement techniques. Thus, only basic results on the steady current boundary layers will be presented here. The studies on wave (oscillatory) and wave–current boundary layers were directed to investigate turbulence characteristics, such as the mean velocity profiles, rms–velocity, turbulent kinetic energy, shear stress, eddy viscosity, and integral–length scales. Some salient features of present studies are the mapping of two–dimensional flow fields and establishing links between turbulence properties in terms of physical features of a particular type of flow. The experimental results were compared with some theoretical models that are commonly used in current numerical modeling (Grant & Madsen (1979), Trowbridge & Madsen (1984)).

5.1 RESULTS AND DISCUSSION ON STEADY CURRENT BOUNDARY LAYERS

The measured variables, in general, can be scaled by inner and outer parameters. The outer parameters (velocity of the mean flow U_m, height of roughness elements r, the distance between roughness elements $W = L$, water depth H) are very convenient for scaling if one wants to compare different sets of experiments conducted with various apparatuses. The inner parameters, obtained as a result of the flow analysis (friction velocity u_*, thickness of the boundary layer Δ_w, Nikuradse roughness k_s, viscosity dominated length–scale ν/u_*), can also give a representation of the turbulent characteristics of the boundary layer. In the present work both types of scaling will be used.

experiment	H (cm)	Q (gal/min)	U_m (cm/s)	$\frac{u_*}{U_o}$	r (cm)	d (cm)	Re_m
$exp-01$	27	102	9.13	0.043	0.635	0.318	26357
$exp-12$	23	76	8.46	0.044	0.635	0.318	22336
$exp-24$	25	79	8.03	0.046	0.476	0.476	22220
$exp-31$	20	61	8.26	0.044	0.476	0.476	20073
$exp-38$	27.5	102	9.30	0.038	0.159	0.318	26970
$exp-46$	27.5	67	6.86	0.051	0.159	0.318	19923
$exp-57$	21	102	9.82	0.039	0.159	0.318	24750

TABLE 5.1. Steady current experimental conditions.

Several steady current experiments were performed with different flow rates (i. e. mean velocity), water depths and bottom roughnesses, as evident from table 5.1. The Reynolds number of the steady current was defined with respect to the mean velocity U_m and the hydraulic diameter $D_h = 2Hw_t/(H+w_t)$ (w_t is the width of the channel):

$$Re_m = Re_h = \frac{\overline{U_m}D_h}{\nu} \tag{5.1}$$

5.1.1 Mean velocity profile

Typical velocity profiles obtained at 18 different streamwise positions within the particle tracking window in steady current experiments as shown in figure 5.1. The mean velocity profile shows some scatter of velocity data up to $y_+ = 60$ and a good collapse in streamwise direction for $y_+ > 60$. Therefore, it appears that the flow in the channel is fully developed. In order to confirm the existence of the overlap boundary layer and to determine the thickness of overlap layer, mean velocity was fitted to the logarithmic velocity profile until a best fit has been achieved, according to

$$\frac{\overline{U_m}(y)}{u_*} = \frac{1}{\kappa}ln\frac{y}{y_o} = \frac{1}{\kappa}ln\frac{30y}{k_s} = \frac{1}{\kappa}lny_+ + B \tag{5.2}$$

Velocity profile Re=22220
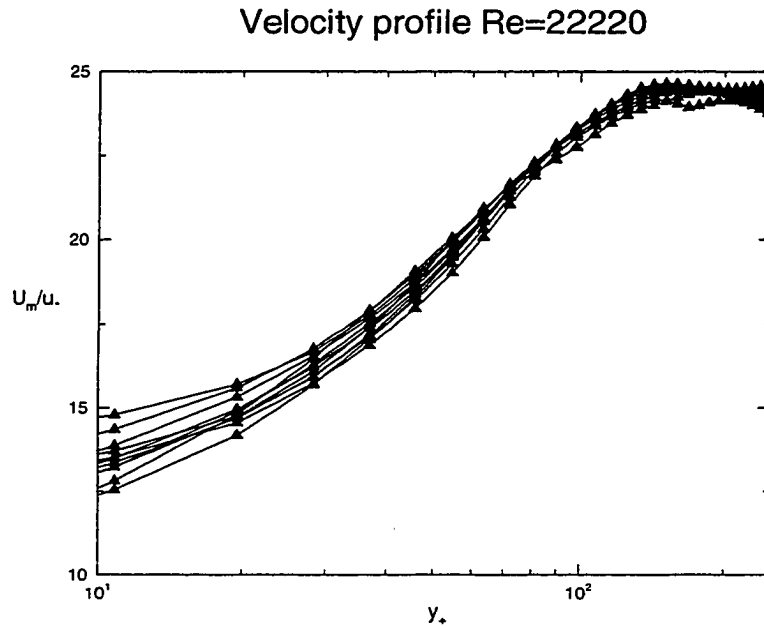
FIGURE 5.1. Velocity profile of steady current Re_m=22220.

and

$$\frac{\overline{U_m}(y)}{u_*} = \frac{1}{\kappa}lny_+ + B \tag{5.3}$$

The results are summarized in table 5.2. The fit of the velocity data are resulted in the determination of the Kármán's constant κ and Nikuradse roughness k_s (i. e. $y_o = k_s/30$) using equation 5.2, and constant B using equation 5.3. The friction velocity u_* was calculated using equation 2.5 and 2.25. It has been shown that constants κ and B match experimental results obtained by previous researchers (Leutheusser (1963), Clauser (1956), Townsend (1956), Landweber (1960)). All of them confirmed the existence of the logarithmic velocity profile and experimentally determined the values of $\kappa \approx 0.41$ and $B \approx 5$. Therefore, velocity profiles obtained for the different

experiment	κ	y_o	k_s	$\frac{k_s}{r}$	B	$\frac{\delta_{overlap}}{\Delta_r}$
$exp - 01$	0.379	7.12e-3	0.213	0.336	6.15	0.158
$exp - 12$	0.448	3.86e-3	0.116	0.183	4.80	0.165
$exp - 24$	0.398	2.41e-3	0.072	0.152	4.92	0.137
$exp - 31$	0.423	6.78e-3	0.203	0.427	4.36	0.157
$exp - 38$	0.435	1.08e-3	0.032	0.301	6.04	0.149
$exp - 46$	0.425	4.41e-3	0.132	0.331	6.43	0.159
$exp - 57$	0.428	3.82e-3	0.114	0.716	5.91	0.165
mean	0.419				5.52	0.156

TABLE 5.2. Results of the velocity fit to the logarithmic profile.
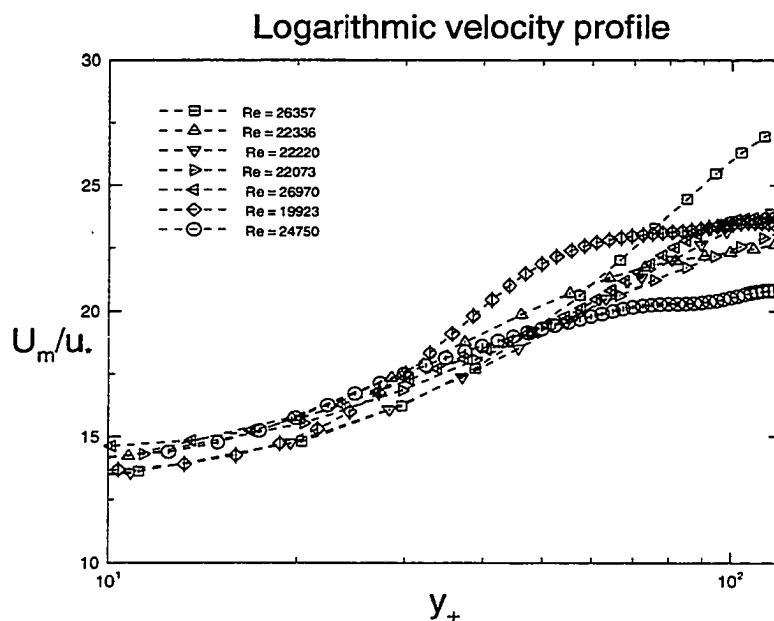
FIGURE 5.2. Velocity profile of steady current for different Reynolds numbers.

Reynolds numbers can be presented in dimensionless form with some scatter (see figure 5.2). In order to reduce the data scatter, it is necessary to average a large number of experiments.

It has been a common knowledge (see White (1991)) that the overlap layer corresponds to region $35 \leq y_+ \leq 350$ corresponding to $2\% \leq y/\delta \leq 20\%$. The present experiments match this fact well and the overlap layer was noted in the region up to $y/\delta \approx 15\%$ or $(y_+)_{max} \approx 57$. Another interesting observation would be the ratio of the friction velocity u_* to the velocity of the mean flow. The present experiments showed that friction velocity (u_*) is approximately 4% of the mean flow velocity (see table 5.1), which is in agreement with the results of Hussain & Reynolds (1975). (one should, however, make a clear distinction between the two experiments, as they have used an air as a working fluid and a smooth boundary).

5.1.2   Turbulence velocity fluctuations

Studies on turbulent velocity fluctuations were performed to determine the turbulence intensity distribution in the region close to the bottom. The characteristics of fluctuating velocity in the fully developed mean turbulent flow can be represented by the *root–mean–square* velocity which is defined by:

$$u_{rms} = \overline{u'^2} = \{\frac{1}{N}\sum_{i=1}^{N}(u_i - \overline{u})^2\} \tag{5.4}$$

The *rms*–velocity distribution is shown in figures 5.3–5.5.

These figures show that the turbulence intensity decreases rapidly towards the top of the boundary layer where intensity has approximately constant value of 2–5% of the free steam (mean) velocity. The turbulence intensity in the immediate vicinity of the bottom is the highest and reaches $10 - 20\%U_m$. However, it has been showed that the turbulence intensity has a local peak usually around $y/\delta \approx 0.1 - 0.2$ (Hussain & Reynolds (1975)), which can be seen for cases of Re_m=22336 and Re_m=22220. The resolution of the present measurement varied from one to the other experiment, and in
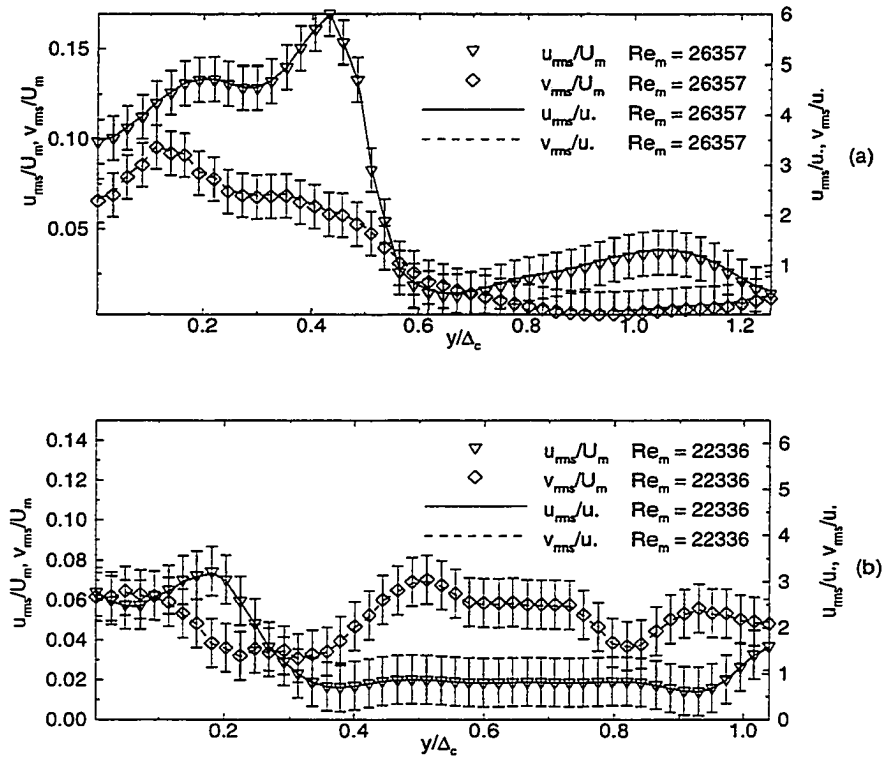
FIGURE 5.3. *RMS* velocity distribution: (a) Re_m=26357 and (b) Re_m=22336.
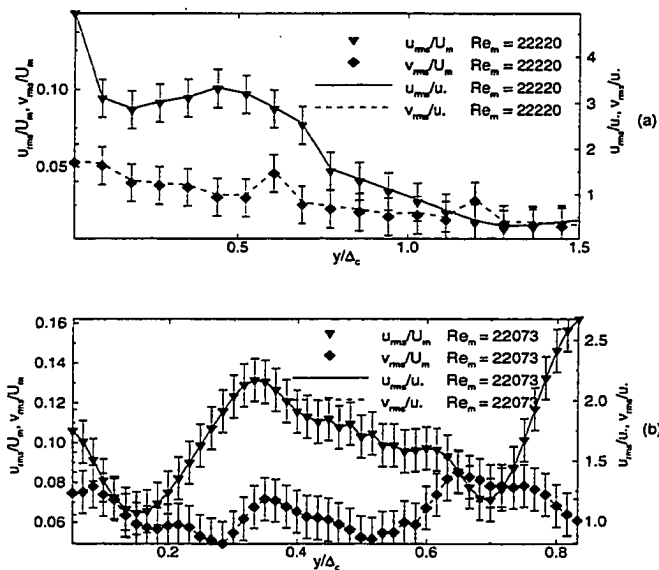
FIGURE 5.4. *RMS* velocity distribution: (a) Re_m=22220 and (b) Re_m=20073.
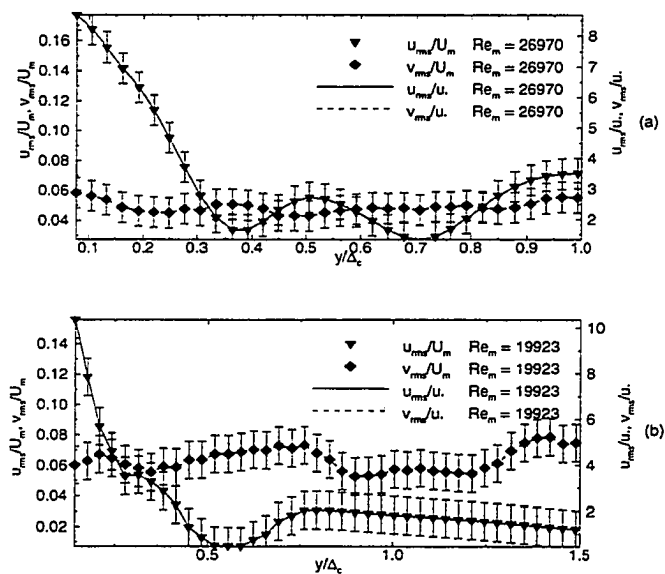
FIGURE 5.5. *RMS* velocity distribution: (a) Re_m=26970 and (b) Re_m=19923.

order to catch fine changes in the velocity fluctuations, it is necessary to have a much finer measurements resolution close to the bottom (see Grass (1971) and Hussain & Reynolds (1975), for example). Moreover, previously (Kim et al. (1971), Grass (1971), Hussain & Reynolds (1975)) has been shown that the ratio of turbulence intensity to the friction velocity is in the range 3–5, which is consistent with present experiments.

5.1.3   Shear stress distribution

The distribution of Reynolds stress and shear stress obtained using equation 2.26 and 2.29, respectively, are presented in figures 5.6 and 5.7.   The distribution of Reynolds stresses has a peak close to the bottom (see Perry et al. (1987)), similar to that of turbulent intensity distribution. However, the Reynolds stress has negative values for some Reynolds numbers in the region close to the bottom $y/\delta < 0.3$. The negative Reynolds stress actually means the positive correlation between u' and v' fluctuation velocities. Grass (1971) offered an explanation to this phenomena based on relatively high longitudinal velocities close to the bottom, which lead to very violent momentum transfer between the layers that keeps $u'v'$ correlation positive. The distribution of shear stress calculated using equation 2.29 shows similar peaks as the Reynolds stresses and turbulence intensities. Those peaks approximately correspond to the top of overlap layer and represent intense turbulence production. Both stresses, change their intensity with the Reynolds number and larger values correspond to larger Reynolds numbers. The Reynolds and shear stresses closer to the top of the boundary layer approaches zero, as expected.

5.1.4   Eddy viscosity distribution

The eddy viscosity was calculated on the basis of Reynolds stress using equation 2.25 and on the basis of shear stress based on the mixing–length 2.29. As discussed in

Reynolds stress distribution
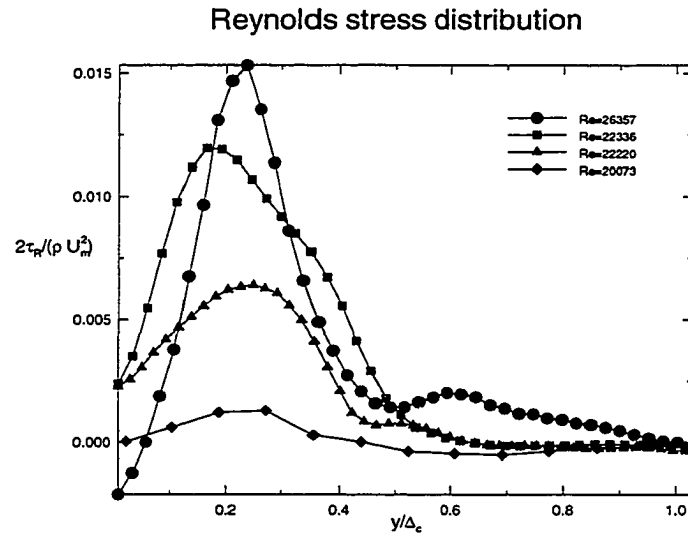
FIGURE 5.6. Reynolds stress distribution in the steady current boundary layer.

Shear stress distribution
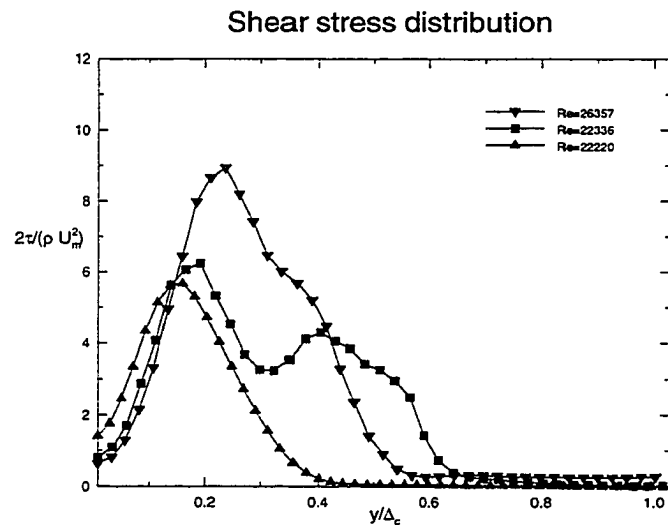
FIGURE 5.7. Shear stress (obtained by equation 2.29) in the steady current boundary layer.
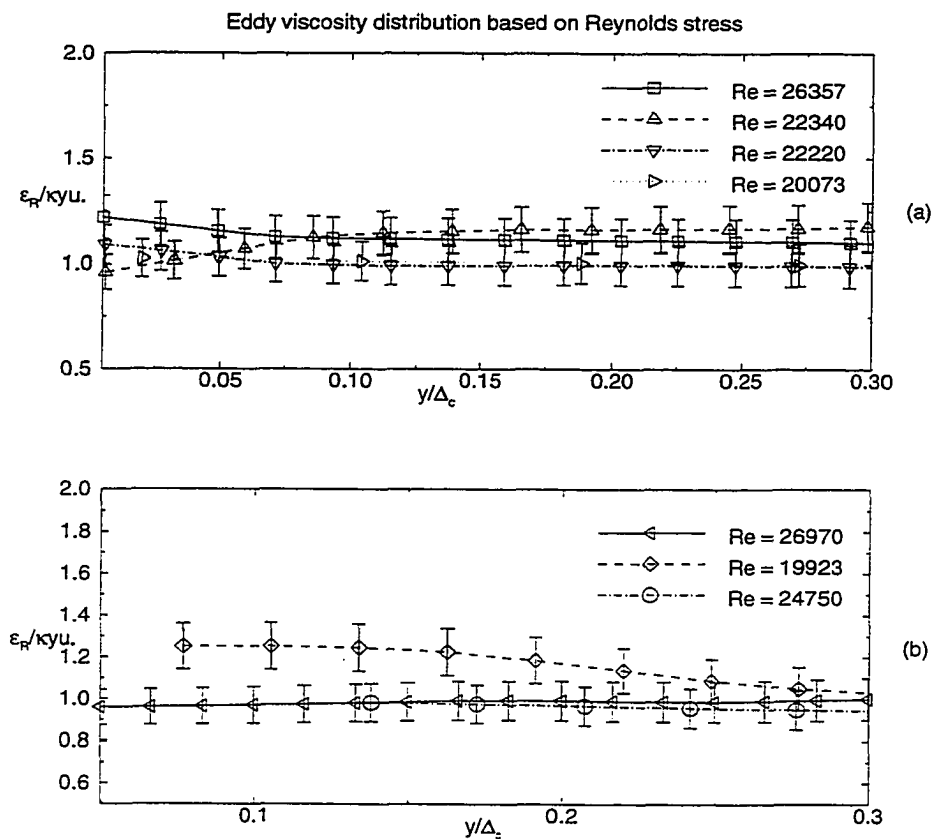
FIGURE 5.8. Eddy viscosity distribution in the steady current boundary layer compared with the theoretical prediction: (a) $Re_m = 26357, 22340, 22220, 20073$ and (b) $Re_m = 26970, 19923, 24750$.

section 2.1.6, the eddy viscosity distribution in the overlap layer is a linear function of the distance from the bottom (or $\varepsilon = \kappa y u_*$). The present data were compared to this theoretical prediction and the results are presented in figure 5.8.

The eddy viscosity calculated on the basis of Reynolds shear stress (see 2.25) showed a fair comparison with the theoretical prediction ($\kappa y u_*$) in the overlap layer ($y/\Delta_c < 0.2$). However, in the immediate vicinity of the bottom the eddy viscosity takes negative values and was commented in the section related to the shear stress (see Grass (1971)). The eddy viscosity distributions of different experiments are presented in figures 5.9 and 5.10. It can be seen that the eddy viscosity is changing drastically from the bottom to the top of the boundary layer, the ones calculated using the Reynolds stress are taking both positive and negative values. The negative values come from the negative Reynolds stress distribution which has been commented in the previous section. The linear (theoretical) eddy viscosity distribution is valid only in the overlap layer which, in present experiments, occupies a region up to about $y/\Delta_c \approx 0.15$. The data, however, showe that although the eddy viscosity is approximately linear in the overlap layer, it does not follow the slope of the theoretical prediction. The eddy viscosity, calculated using 2.29, follows the slope κu_* better for the cases of smaller Reynolds number. Similar tendency was obtained, too, by the experiments of Hussain & Reynolds (1975). Also, the eddy viscosity tends to have smaller values at large distances from the wall.

The experiments on steady current boundary layers, the particle tracking technique and methodology of data analysis reproduced previous results with a reasonable accuracy with regard the mean velocity distribution, turbulence intensity and characteristics of overlap layer. Therefore, our techniques are expected to be valid for the rest of the studies to be discussed in this thesis.
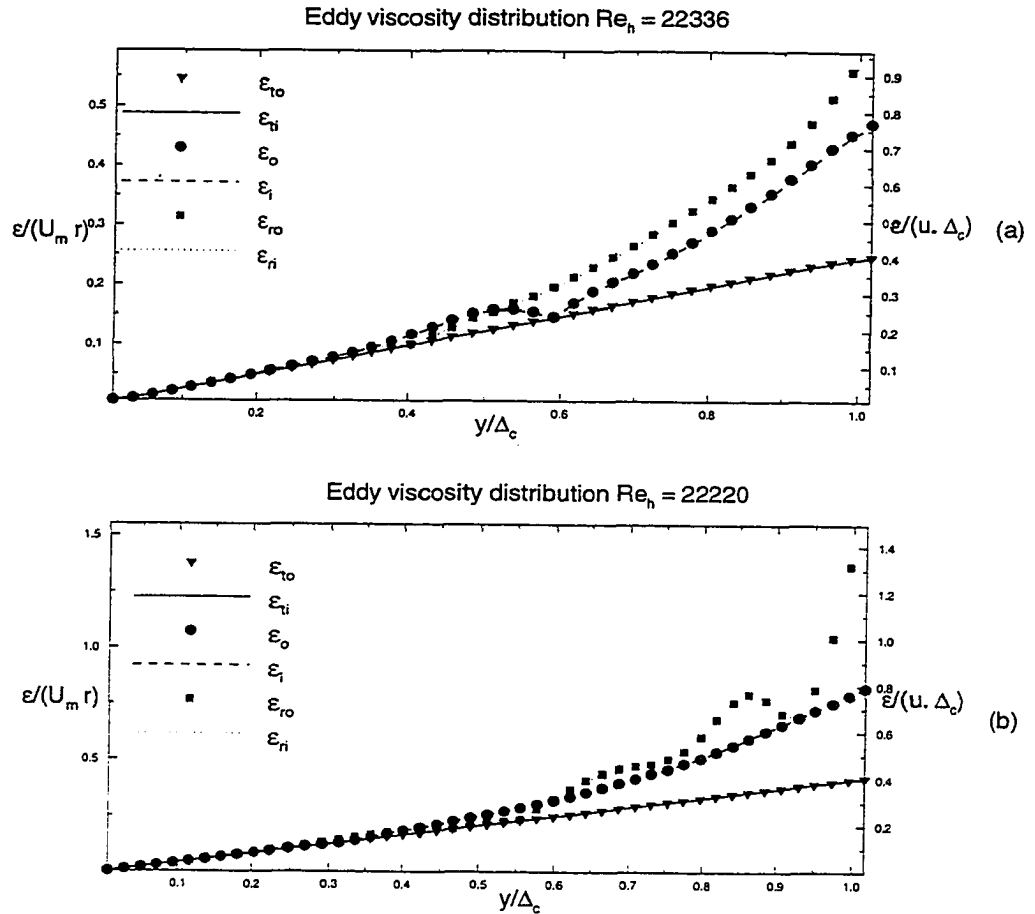
FIGURE 5.9. Eddy viscosity distribution in the steady current boundary layer: ε_{to} and ε_{ti} are calculated using 2.31 and scaled by outer and inner parameters, respectively; ε_o and ε_i are calculated using 2.29 and scaled by outer and inner parameters, respectively; ε_{ro} and ε_{ri} are calculated on the basis of Reynolds stress and scaled by outer and inner parameters, respectively. Two Reynolds numbers: (a) Re_m=22336 and (b) Re_m=22220 are shown.

Eddy viscosity distribution $Re_h = 19923$

(a)

Eddy viscosity distribution $Re_h = 24750$

(b)
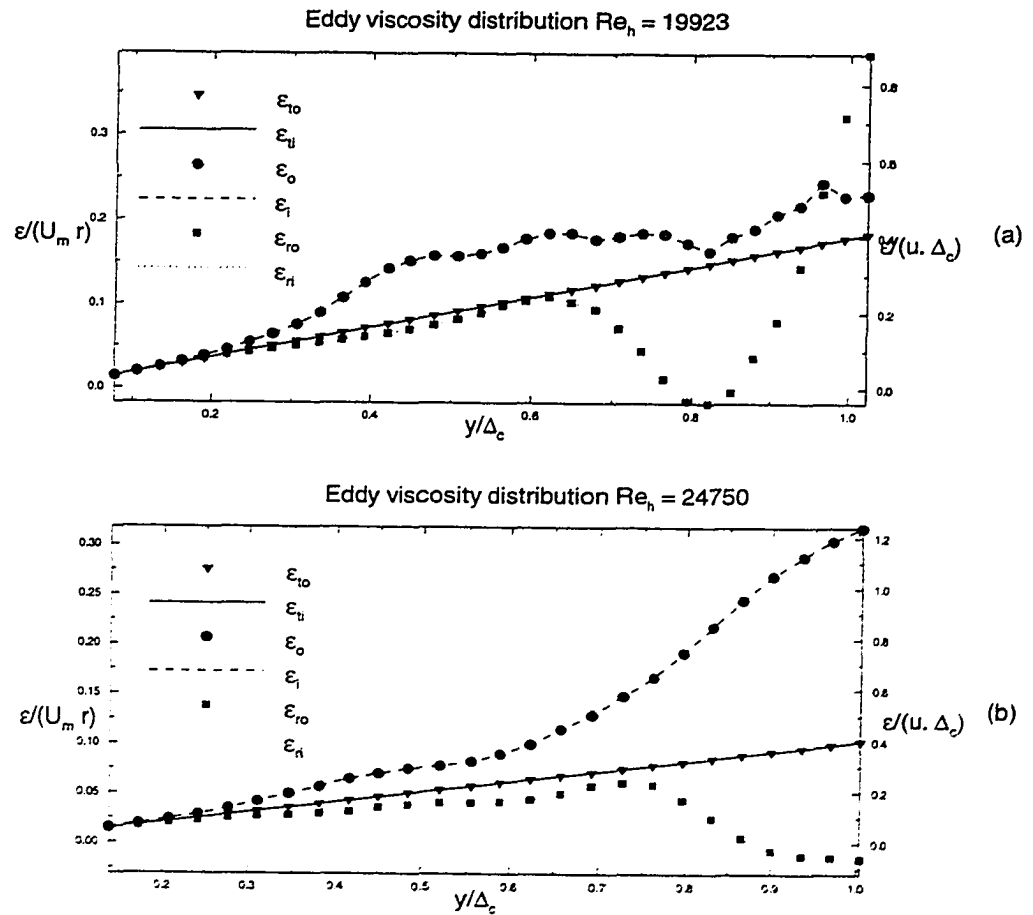
FIGURE 5.10. Eddy viscosity distribution in the steady current boundary layer. See caption of figure 5.9. Comparison was presented for (a) $Re_m = 19923$ and (b) $Re_m = 24750$.

5.2 RESULTS AND DISCUSSION ON WAVE (OSCILLATORY) BOUNDARY LAYERS

5.2.1 Introduction and brief summary of previous work

Studies on oscillatory boundary layers have received considerable attention in the past, particularly because of its relevance to the bottom boundary layer of coastal oceans (Nielsen (1992),Sleath (1995)). Shoaling waves in coastal regions lead to an oscillatory (irrotational) velocity field in the upper layers, which is commonly approximated by the simple harmonic form $u_\infty = U_o sin(\omega t)$ where $U_o = A\omega$ is the velocity amplitude, A the semi–excursion of fluid particles, ω is the forcing frequency and t the time. (Coastal oceanic flows, however, are much more complicated, contributed by tides, rip and longshore currents and random waves). Near the ocean bottom, in the *coastal boundary layer* (CBL), this velocity field is drastically modified in order to satisfy the no–slip boundary condition, and many important coastal phenomena such as scour, erosion and sediment transport are controlled by the CBL. Because of the highly irregular topography the bottom of the ocean can be treated as a rough surface with an effective roughness height r.

In the absence of mean currents, it is customary to model the CBL as an *oscillatory boundary layer* (OBL) over a rough surface, with the governing parameters being A, ω, r and ν (the kinematic viscosity). The relevant non–dimensional parameters are the Reynolds number $Re = A^2\omega/\nu$ and relative roughness r/A (Jonsson (1966)), of which typical CBL values are $Re = A^2\omega/\nu > 10^5$ and $r/A > 0.08$ (Nielsen (1992)). Because of the difficulty of obtaining extensive data sets in oceans, coastal engineers have resorted to laboratory and numerical studies on OBLs to understand the CBLs. In the laboratory context, two types of flow configurations have been used. They are the *oscillatory water tunnels* (Lundgren & Soerensen (1956)), wherein the flow is

periodically slashed by a piston located at one limb of a large U–tube, and *oscillating beds* in which the (infinite) bottom boundary of an otherwise still water column is oscillated (Bagnold (1946)). In the latter case, the bottom is oscillated with a velocity $U_p = U_o sin(\omega t)$, yielding an oscillatory velocity field $u^L(y, t)$ with respect to the laboratory (inertial) coordinates or a velocity $u = u^L(y, t) - U_o sin(\omega t)$ with respect to the oscillating plate (here y is positive upward with $y = 0$ at the bed; the velocity is parallel to the wall, in the x direction). Note the $-u(y, t)$ takes the form of velocity defect in oscillatory water tunnels and hence the kinematic similarities are expected between the two flows, although they are dynamically dissimilar due to the non–inertial nature of oscillating coordinate system (see Chapter 3). It can be shown, however, that the solutions for equations of motions written with respect to the laboratory and oscillating coordinates are the same provided that boundary conditions are specified on the velocity and not on the pressure, as in the case of present study. The pressure gradient forces in the two cases are considerable different, nonetheless, and hence oscillating bed experiments are unsuitable for research embodying fluid forces, for example, sediment transport studies. In spite of this drawback, oscillating bed experiments have become a useful and popular experimental tool in CBL studies because of their simplicity and cost–effectiveness.

As stated earlier, extensive literature exists on OBLs, on which Nielsen (1992) and Sleath (1995) have published excellent reviews. It has been shown that rough–wall oscillating boundary layers generate turbulence, at least during a part of the oscillating boundary cycle, when $Re > 104$, where D is the median grain size of the bed sediment (Kajiura (1968)) and that turbulence is produced over an entire oscillatory cycle when $Re > 70,000(A/D)^{0.17}$ (Sleath (1990)). It is customary to analyze the instantaneous velocity in a turbulent OBL in terms of a deterministic (coherent) oscillatory velocity $\bar{u}_i$ and a random (incoherent) fluctuating velocity u'_i.

Thus the equation 2.69 can be simplified

$$u_i = \tilde{u}_i + u'$$

(5.5)

where the tilde denotes periodic component obtained according to equation 2.70. The resulting vertical flux of horizontal momentum, simplified from equation 2.72, becomes

$$\tilde{\tau} = \nu \frac{\partial \tilde{u}}{\partial y} - (\widetilde{\tilde{u}\tilde{v}} + \widetilde{u'v'})$$

(5.6) .

The previous equation is commonly cast in numerically modeling in terms of eddy diffusivity ν_t as

$$\nu_T = \frac{\tilde{\tau}}{\rho \frac{\partial \tilde{u}}{\partial y}} = \frac{-\widetilde{\tilde{u}\tilde{v}} - \widetilde{u'v'}}{\frac{\partial \tilde{u}}{\partial y}} + \nu$$

(5.7)

Note that this definition of eddy diffusivity differs from the traditional eddy diffusivity ν_i which is based on incoherent velocity component,

$$\nu_i = \frac{-\widetilde{u'v'}}{\frac{\partial \tilde{u}}{\partial y}} + \nu$$

(5.8)

Using equation 5.7, the horizontal equation can be recast in the form

$$\frac{\partial \tilde{u}}{\partial t} = \frac{\partial u_\infty}{\partial t} + \frac{\partial}{\partial y}(\nu_t \frac{\partial \tilde{u}}{\partial y}) = \frac{\partial u_\infty}{\partial t} + \frac{\partial}{\partial y}(\tau)$$

(5.9)

which is frequently used in the modeling work (Trowbridge & Madsen (1984)); here u_∞ is the free–stream velocity. Integration of 5.9 yields

$$\tau(y,t) = \tau_b + \int_0^y (\frac{\partial \tilde{u}}{\partial t} - \frac{\partial u_\infty}{\partial t})dy \qquad (5.10)$$

where τ_b is the bed shear stress. For small y the second them in the right–hand side is negligible, thus yielding an approximately constant stress layer in the vertical direction. A logarithmic velocity profile can be expected in this layer, the existence of which have been verified by many authors; see, for example, Jonsson & Carlsen (1976) and Jensen *et al.* (1989). The smallness of the second term in equation 5.10 implies that the flow in the constant stress layer responds instantaneously to the varying bed shear stress. The distributions of turbulent intensities and shear stresses within OBLs have been subjected to detailed studies (Sleath (1987), Sleath (1995)), but so far only little has been done to relate these observations to the flow structures within OBLs.

In the context of predictions, numerous models have been proposed for the closure of equation 5.9, see Villaret & Davies (1995). These include the eddy viscosity and mixing length models (e.g. Kajiura (1968), Brevik (1981), Trowbridge & Madsen (1984)), $k - \varepsilon$ models (Celik & Rodi (1985), Asano, Godo & Iwagaki (1988), Davies (1986)), and higher order models (Villaret (1987)). Most of these models fall into the first category, wherein models for eddy viscosity ν_T are used for closure. With a few exceptions, the available models use time invariant eddy viscosities (Kajiura (1968), Brevik (1981), Myrhaug (1982)), an assumption which has been challenged repeatedly (Horikawa & Watanabe (1968), Sleath (1987)). Nevertheless, models based on time–invariant ν_T can produce reasonable predictions for the mean flow that are consistent with observations. Because many of the experiments have been performed

using point measurement techniques, such as Laser–Doppler Velocimetry, obtaining time and space resolved velocity is difficult and hence only a handful of studies are available on the direct evaluation of eddy coefficients (Sleath (1987)).

An exception to the time–invariant models is that of Trowbridge & Madsen (1984) wherein the eddy viscosity is written in the form

$$\nu_t = \nu^{(0)} \Re(1 + a^{(2)} e^{2i\theta}) \tag{5.11}$$

and

$$\nu^{(0)} = \kappa \overline{u_f} y \qquad 0 \leq y \leq \delta_I \tag{5.12}$$

$$\nu^{(0)} = \kappa \overline{u_f} \delta_I \qquad \delta_I < y \tag{5.13}$$

Here the real constant $\overline{u_f}$ is a shear velocity characterizing the average turbulence intensity over the wave period, κ is von–Karman constant, $\theta = \omega t$, $a^{(2)}$ is a complex constant representing the amplitude of the temporal variation of viscosity and δ_I characterizes the boundary–layer thickness; δ_I was set to $l_{GM}/6$, where $l_{GM} = \kappa \overline{u_f}/\omega$ is a length–scale introduced by Grant & Madsen (1979). The constants in equation 5.11 can be evaluated using equation 2.5 and

$$\overline{u_f} a^{(2)} = \overline{2e^{-2i\theta} |\tau_b/\rho|^{1/2}} \tag{5.14}$$

where the over–bar denotes average over one wave period. The efficacy of this model has not been verified experimentally.

The experimental study reported herein was carried out with the aim of investigating the flow structures within turbulent OBLs and their role in determing such macroscopic quantities as the effective eddy viscosity ν_T and boundary layer thickness Δ_w. As ν_T is a key quantity in modeling, special attention was given to investigate how ν_T changes over a cycle. In particular, the Trowbridge & Madsen (1984) parametrization was checked and related quantities such as Δ_w and other turbulent length–scales were measured and interpreted in terms of flow structures. These experiments on OBLs were performed using the short tank. The variety of parameters, such as amplitude, period of oscillations and bottom roughness values, have been used and the test conditions are shown in table 5.3.

5.2.2 The nature of the flow

It has been long known that vortex structures present in the OBLs cause a rich variety of flow phenomena, for example, the jet–type features at a certain phase that carry low momentum fluid upward. These structures may take the form of horseshoe–like vortices characteristic of turbulent wall layers or vortices formed by the flow separation at roughness elements (Sleath (1987)). As in other boundary layers, vortex dynamics is a key phenomenon in rough–wall OBLs and, therefore, detailed flow visualization was performed in the wall region to observe vortex structures. Figure 5.11 shows a sequence of LIF video frames taken with the phase separation of 30°, starting from time $t = o$, during the experiment where the dye was interlarded among roughness elements prior to the beginning of oscillations.

The images taken in this and other experiments indicate that the vortex formation at roughness elements is pronounced when the fluid velocity is close to its maximum (see initiation of flow separation in frame 3, $\omega t = \pi/2$). They appear at the leading edge of roughness elements as "separated" vortices (4-5); note that the flow relative

(a)

| $\pi/2<\omega\tau<\pi$ | $\pi<\omega\tau<3\pi/2$ | $3\pi/2<\omega\tau<2\pi$ | $\omega\tau-2\pi$ |
| (i) | (ii) | (iii) | (iv) |

(b)
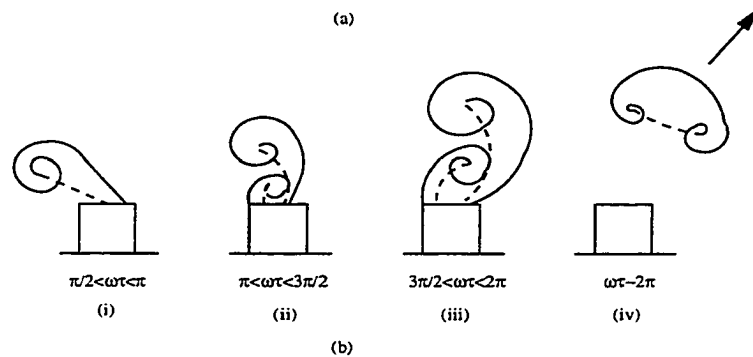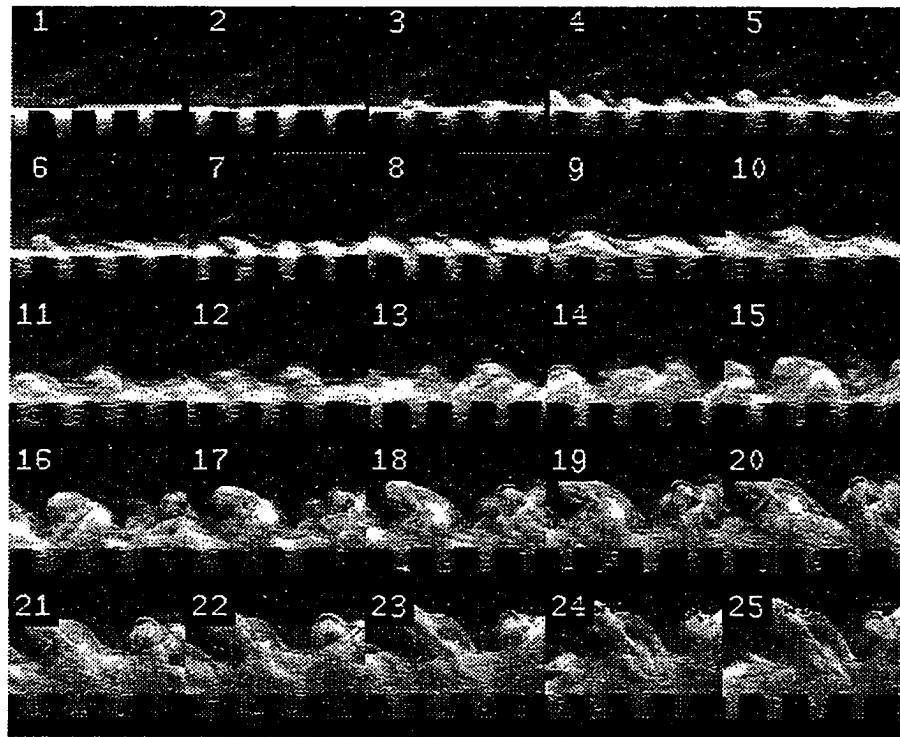
FIGURE 5.11. (a) Visualization photos of dye dispersion during the oscillations of a rough plate: A=10cm, T=5s, W=L=r=0.48cm. Phase difference between the images is $\Delta\omega t$ =30 deg, starting from 0 deg, before which the plate was at rest. (b) Schematic showing the development of vortex structure.

Exp. No.	A [cm]	T [s]	r	H [cm]	$Re = A^2\omega/\nu$
1	5	2	r6	18	7854
2	5	3	r3	25	5235
3	7	7	r2	20	4398
4	8	4	r3	25	10054
5	8	8	r2	20	5027
6	11	8	r3	25	9498
7	7	5	r4	25	6154
8	9	5	r5	18	10179
9	9	6	r4	25	8480
10	10	6	r4	25	10470
11	7	3	r5	18	10260
12	11	6	r5	18	12669
13	14	7	r7	27	17601
14	13	6	r3	25	17697
15	10	5	r8	27	12560
16	12	6	r8	27	15072
17	14	5	r8	27	24618
18	10	5	r2	20	12560
19	12	5	r5	18	18086
20	13	6	r3	25	17694
21	14	9	r1	20	13681
22	14	6	r5	18	20521
23	15	10	r2	20	14130
24	15	6	r3	25	23558

TABLE 5.3. Test conditions for oscillatory boundary layer investigation with short tank. A is an amplitude and T is the period of oscillations, $r - type$ is the type of roughness (table 4.1), H is water depth and Re is the Reynolds number of oscillations.

to the plate at this time is from right to left. The separated vortices appear to remain inactive, or even weaken, and do not show appreciable vertical movement during the decrease of velocity over the rest of the half–cycle (4-6). The vortices appear to be slowly advected by the flow and elongated in the streamwise direction due to background shear. A schematic of this scenario is also shown in figure 5.11(i). As the reversal of the outer flow is felt near the wall (7-12), these vortices, while advecting

back, show a clear vertical movement, thus allowing the formation of vortices at the opposite edge of roughness elements. This is schematized in figure 5.11(ii, iii). Because of strong dye dispersion during the first half of the cycle, the formation of the second set of vortices is unclear in figure 5.11(a) but it was clearly evident during close inspection of video records. Toward the end of the cycle, these vortex pairs appear to detach from roughness elements, having the structure somewhat similar to that of vortex dipoles described by Voropayev, Afanasyev & Van Heijst (1995); see figure 5.11b(iv). In the present case, unlike in the case of Voropayev *et al.* (1995), these entities are highly three–dimensional and hence will be referred as dipole–like structures. Because of opposite polarities of the vortices encapsulating them, these dipole–like structures tend to propel away from the wall by self–induced linear momentum. Each structure blends with similar ones in the background, forming an OBL replete with mutually interacting dipole–like vortex structures. The vorticity produced at the wall, thus, is carried upward in the OBL at a rate faster than that of traditional viscous diffusion mechanism intrinsic to non–oscillatory boundary layers. Dipole–like structures generated in every cycle at each roughness, are subjected to the deformation by the background flow and act as a key vorticity production and transport mechanism. Another noteworthy fact is that, because the direction of vortex ejection is dependent on initial flow direction, certain amount of memory is retained in the OBL with regard to dipole–like structure formation. The asymmetry produced by this memory is mirrored in subsequent turbulent measurements, as will be described below.

The jet–type features that has been identified in oscillatory boundary layers (Sleath (1987)) can be attributed to dipole–like structures propagating off of roughness elements at an angle to the vertical (see figure 5.11b(iv)). This asymmetry arises due to the nature of the generation process, where one vortex is formed before the

other, and influences the other, a feature remnant of initial conditions. The data presented by Sleath (1987) (his figure 36) indicate that jet–like features in the OBLs indeed form toward the end of a cycle and propagate at and angle to the vertical.

Figure 5.12 shows a plot of instantaneous velocity vectors in the vicinity of roughness elements, soon before the outer flow (from left to right) reverses its direction at $\omega t = 2\pi$; the flow near the wall responds to this reversal with a short time delay. Note the similarity of vortex structures to that of figure 5.11b(iii). Because the flow in OBL is so irregular, incisive details such as those shown in figure 5.12 were captured by PTV system only occasionally. Signatures of separated vortices, however, were always evident in PTV. No attempts were made, in the present study, to educe complex three-dimensional flow structures within OBLs, and figure 5.12 was merely presented to provide qualitative evidence for the claim of dipole–like structure formation.

5.2.3 Turbulent kinetic energy

The emergence of dipole–like structures is also evident from the turbulent kinetic energy (TKE) measurements shown in figure 5.13, where the measurable component of TKE ($K_o = 1/2(\tilde{u'}^2 + \tilde{v'}^2)$), is shown up to $y/\Delta_w = 1$ over one cycle. Note the intensification of K_o surrounding $\omega t = \pi/2$, where the conditions for maximum vorticity production during the first half cycle exist. An enhancement of K_o can also be seen in the second half of the cycle, near $\omega t = 3\pi/2$, but this increase spreads to greater heights than that of $\omega t = \pi/2$. This may be due to maturation of dipole–like structures in the latter half of the cycle (see figure 5.11b(iii) and the discussion on Reynolds stresses below).
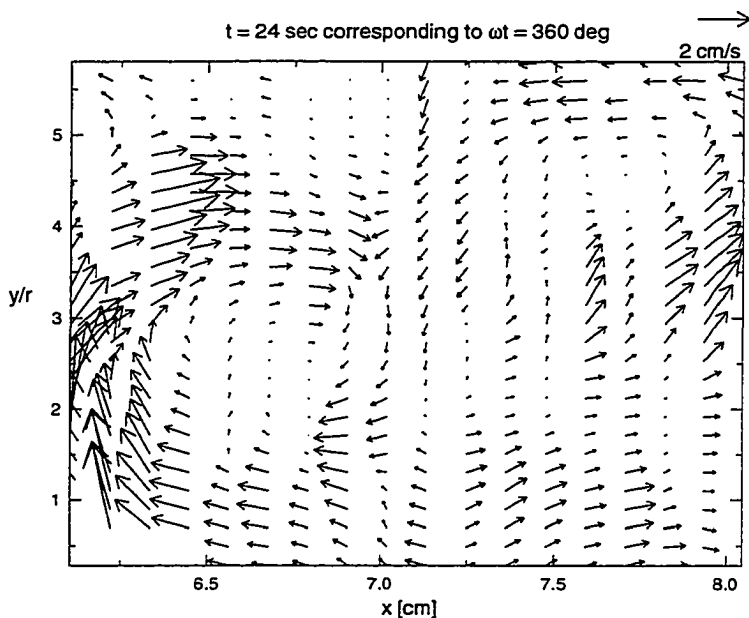
FIGURE 5.12. Velocity field measured relative to the roughness elements at an instant just before $\omega t = 2\pi$: A=14cm, T=6s, L=W=0.48cm, r=0.08cm.

5.2.4 Shear stress in oscillatory boundary layer

The Reynolds stress $\tau_R = -\rho\widetilde{u'v'}$ variation over a cycle was shown in figure 5.14, as a function of the distance from the wall. During $0 < \omega t < \pi$, whence the outer flow is from right to left, the velocity fluctuations can be biased with $u' < 0$, $v' > 0$, and $-u'v' > 0$, which is generally evident from figure 5.14. The high turbulence levels observed during the first part of the cycle (figure 5.13) can be attributed to high τ_R during $0 < \omega t < \pi/2$. The phase for maximum τ_R in the first half of the cycle seems to be constant for $y/r < 5$, and increases with y for $y/r > 5$, perhaps indicating the quick response of wall region ($y/r \approx 1 - 5$) to the variation of bottom conditions (as discussed earlier) and the time lag between the τ_R production near the wall and its
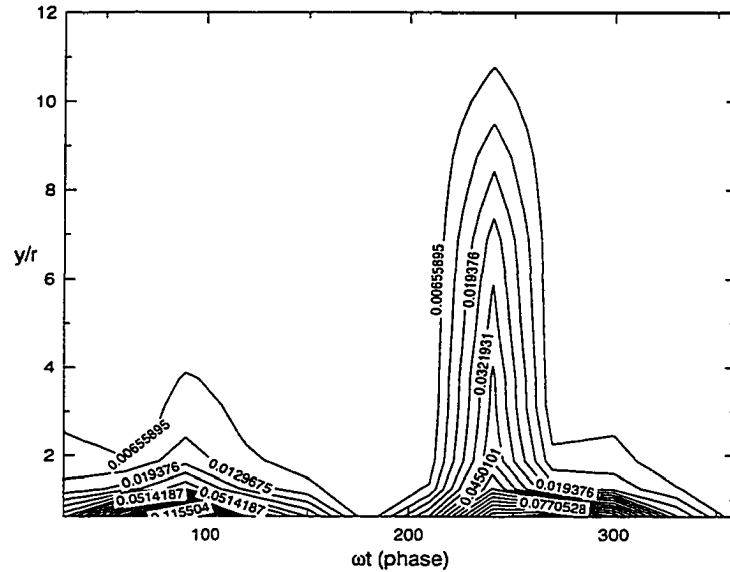
FIGURE 5.13. Distribution of normalized turbulent kinetic energy K_o/U_o^2 during one cycle of oscillations: A=12cm, T=5s, $W = L$ =0.48cm, r=0.08cm. The data have been averaged over 10 cycles.

transport to the measurement location when $y/r > 5$. During a substantial part of the oscillating cycle, τ_R is close to zero, indicating that the turbulence production occurs only during a part of the cycle. In $\pi < \omega t < 2\pi$, the observation of non–zero Reynolds stresses is consistent with enhanced K_o in the same range of phases.

The total stress (equation 5.6) is shown in figure 5.15, which illustrates that $\bar{u}\bar{v}$ is a major momentum transport entity in the OBL. Note that the total stress can be order of magnitude larger than the Reynolds stress. The increase of τ in $\pi < \omega t < 2\pi$ for $y/r = 5$ and 14.3 can be attributed to the generation and expulsion of dipole–like
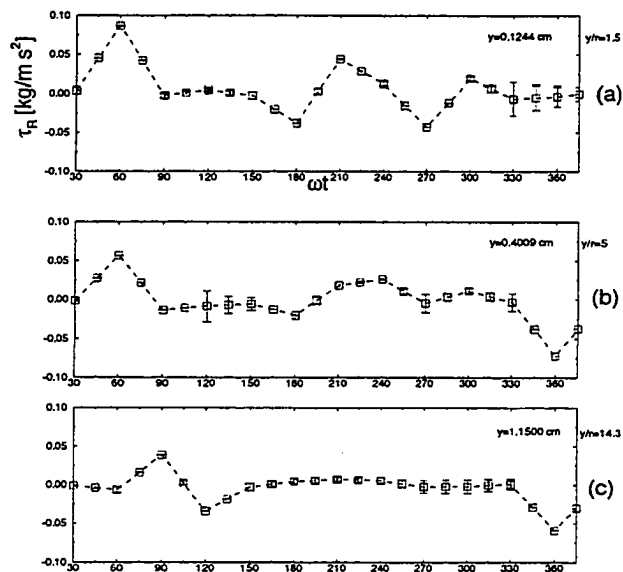
FIGURE 5.14. Distribution of Reynolds stress during one cycle of oscillations: (a) $y/r = 1.5$, (b) $y/r = 5$ and (c) $y/r = 14.3$.
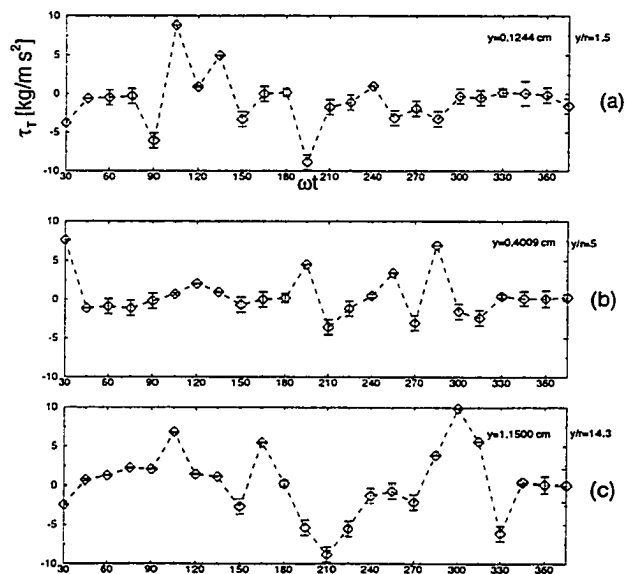
FIGURE 5.15. Distribution of total stress during one cycle of oscillations: (a) $y/r = 1.5$, (b) $y/r = 5$ and (c) $y/r = 14.3$.

structures that are capable of carrying lumps of fluid away from the boundary region.

5.2.5 Boundary–layer thickness measurements

The boundary–layer thickness Δ_w can be defined as the distance between the top of the roughness elements and the level where the velocity has a maximum, as shown in the figure 5.16. This particular definition gives a measure of a layer adjacent to the rough wall over which the velocity deviates significantly from that of the free stream. Several authors have reported measurements of Δ_w in the non–dimensional form

$$\frac{\Delta_w}{k_s} = C_1 (\frac{A}{k_s})^{C_2} \tag{5.15}$$

where k_s is Nikuradse roughness. According to Jonsson (1980), $C_1 = 0.072$ and $C_2 = 0.75$ whereas Sleath (1987) proposed $C_1 = 0.27$ and $C_2 = 0.67$. Their predictions and the present measurements are shown in figure 5.16 as a plot between Δ_w/r and A/r, where r is assumed to play the role of k_s. Note that the present results do not follow either of these predictions, but fall in between and show some scatter. When curve fitted, the present data follow $C_1 = 0.44$ and $C_2 = 0.75$. In addition, as shown in figure 5.16, when plotted as a function of $Re = A^2\omega/\nu$, the present data show a strong dependence on Re. This points the possibility that the disparities between different experiments evident from figure 5.16 can be due to the neglect of Re dependence.

The relationship between Δ_w/r on Re shown in figure 5.17 appears to be independent of A/r, as Δ_w/r values obtained at a given Re do not vary substantially in different A/r ranges. Regression analysis show that the dependence of Δ_w/r on A/r

is indeed weak, and the results can be expressed in the form

$$\left(\frac{\Delta_w}{r}\right) \approx C_3 \left(\frac{A}{r}\right)^{0.1} Re^{1.02} + C_4 \tag{5.16}$$

where $C_3 = 8.2 \times 10^{-4}$, $C_4 = -4.26$, indicating a strong influence of Re. A relation of the form $\Delta_w/r = 9.2 \times 10^{-4} Re$ is evident beyond $Re > 13,000$.

The linear dependence of Δ_w/r on Re can be explained using mechanistic arguments based on dipole–like structure formation. The vorticity associated with each vortex contained in these structures can be represented by $\Omega \approx U_o/r$, as the maximum velocity U_o and the flow separation at roughness elements of height r mainly contribute to the vorticity. Since the distance between the vortices is scaled as A, the initial upward velocity of the vortex pair can be estimated as $V_o \approx U_o A/r$. Vortices associated with dipole–like structures should have the radius r and volume Wr^2, where W is the width of roughness element, and they move away from the wall region subjecting to a viscous friction force $(\rho \nu V/r)(rW)$, where V is the velocity of propagation of the vortex pair after time of t'. Using a simple force balance, it is possible to obtain $V = V_o e^{-\nu t'/r^2}$; the distance of propagation of vortex pair, which is a measure of the boundary–layer thickness, thus becomes $\Delta_w \approx V_o r^2/\nu \approx U_o A r/\nu$ or $\Delta_w/r \approx A^2 \omega/\nu = Re$, which is in agreement with observations described by equation 5.16.

5.2.6 Length–scale measurements

Parametrization of length–scales in terms of governing variables is central to the parametrization of eddy diffusivities of OBLs. To this end, a number of length–scales have been proposed. These include the mixing length based on friction velocity
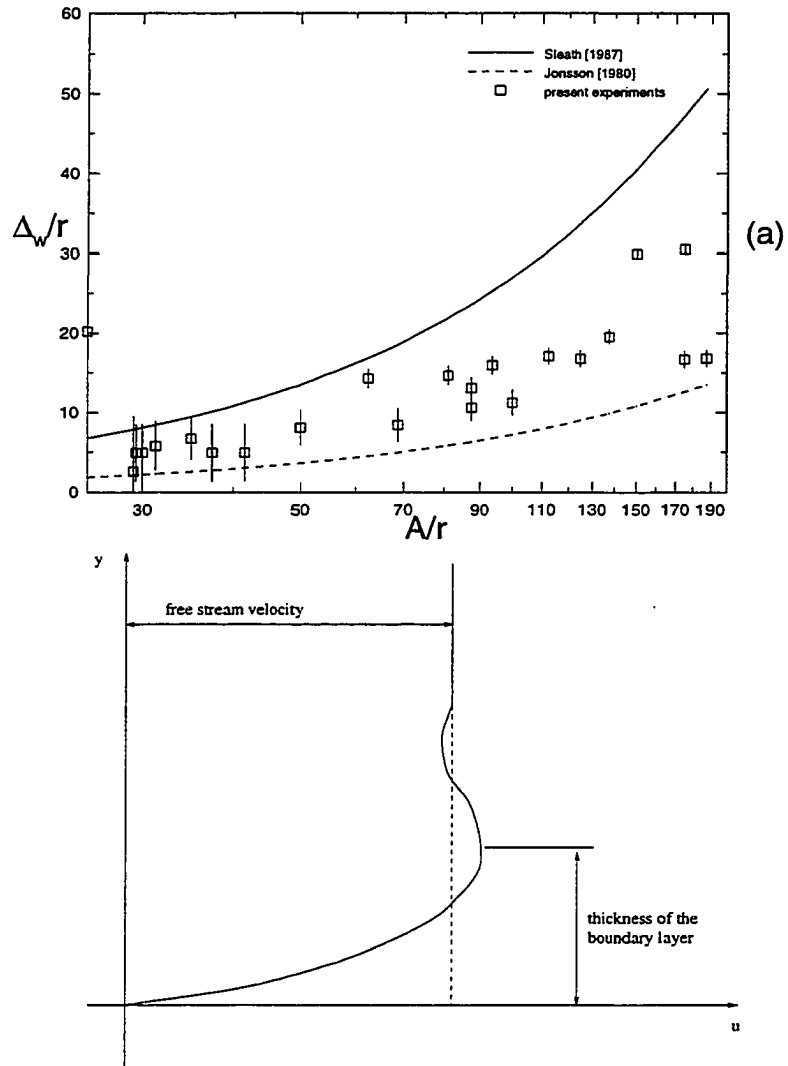
FIGURE 5.16. (a) Boundary–layer thickness measurements compared with the correlations proposed by Sleath (1987) and Jonsson (1980). (b) Definition of boundary layer thickness.
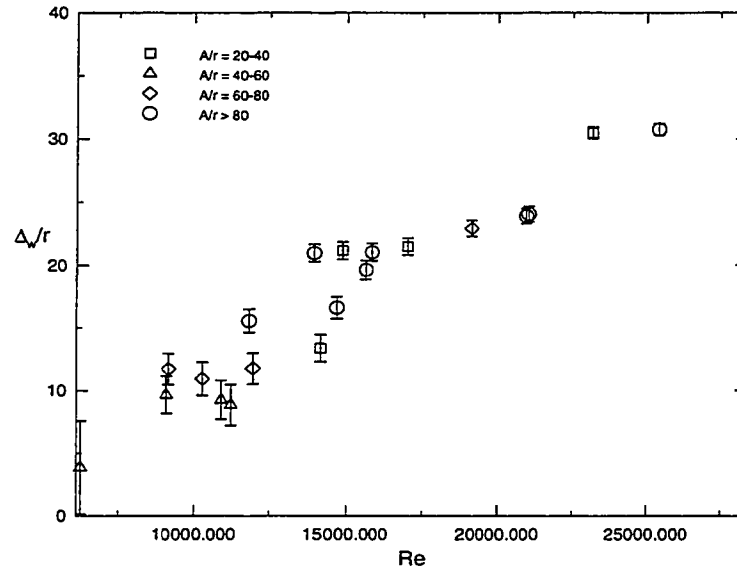
FIGURE 5.17. Normalized boundary–layer thickness as a function of Re.

$u_*(t) = (\tau_b(t)/\rho)^{1/2}$ proposed by Sleath (1987),

$$l_{mix} = \frac{u_*(t)}{\frac{\partial u}{\partial y}} \qquad (5.17)$$

he boundary layer scale used by Grant & Madsen (1979) (which has also been utilized by Trowbridge & Madsen (1984)),

$$l_{GM} = \kappa \frac{\overline{u_*(t)}}{\omega} \qquad (5.18)$$

and the length–scale

$$l_* = \frac{u_{*max}}{\omega} \qquad (5.19)$$

based on the maximum friction velocity (Nielsen (1992)).

In order to evaluate the relevance of these scales to OBL, our measurements were used to evaluate turbulent length–scales at different heights y. These are the longitudinal $L_x{}^{uu}(y,t)$ and transverse $L_x{}^{vv}(y,t)$ turbulent length–scales defined by the general expression

$$L_x{}^{u_i u_j}(y,t) = \int_0^\infty \frac{\langle u_i'(x,y,t)u_j'(x+r,y,t)\rangle}{\langle u_i'\rangle\langle u_j'\rangle} dr = \int_0^\infty R_x{}^{ij}(r,y,t)dr \qquad (5.20)$$

where $\langle\rangle$ represents the horizontal spatial average at a given phase ωt and height y and $R_x{}^{ij}(r,y,t)$ is the auto–correlation function. Figure 5.18 shows typical auto-correlation functions for several distances y, where the plots represent $R_x{}^{ij}(r,y,t)$ taken at a given phase averaged over ten cycles. Figure 5.19 shows integral length-scale measurements and their comparison with equations 5.17– 5.19. Also shown is the laminar Stokes boundary–layer thickness $l_s = \sqrt{2\nu/\omega}$. Inspection of these plots reveal that turbulent length–scales in the OBL are reasonably well predicted by the formulation of Grant & Madsen (1979), although notable discrepancies between the model and measurements can be seen at some phases. The predictions seems to be less satisfactory for $Re < 18000$, where length–scales tend to oscillate around l_{GM} value (not shown). As expected, the laminar Stokes layer thickness is smaller than the measured one.

To investigate the applicability of the present results to high Reynolds number oceanic situations, the length–scales at a given height were averaged over ten wave cycles, and the results (normalized by scale l_{GM}) were plotted as a function of Re (figure 5.20). Since the governing non–dimensional parameters involve A/r and Re, the data were separated into four A/r ranges (which are indicated by different symbols). It appears that, at low Re, the normalized length–scales are dependent on Re,
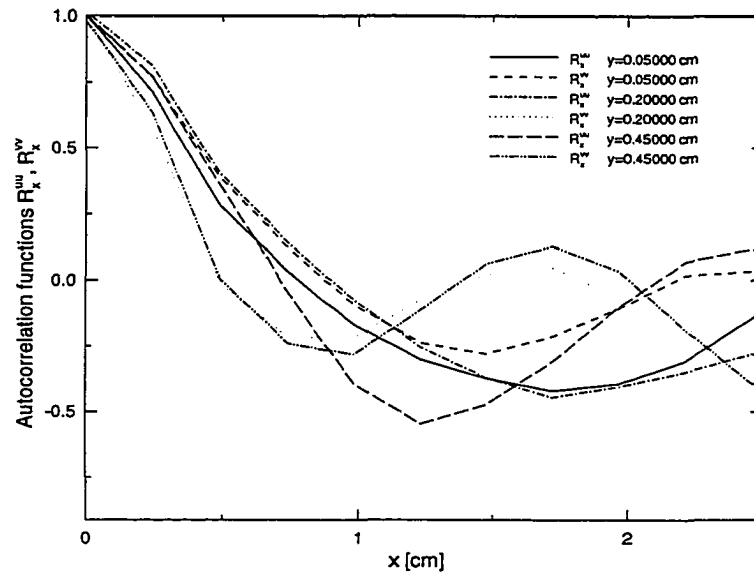
FIGURE 5.18. Set of auto–correlation functions obtained at three different heights for two velocity components at the phase ωt=60 deg. A=12cm, T=5s, $L = W$ =0.48cm, r=0.08cm, Re=18086.

but they seem to approach an asymptotic value $Re > 18000$. Any dependence on A/r could not be identified from the present data.

5.2.7 Calculation of eddy–viscosity coefficient

As mentioned before, a large number of eddy diffusivity models exist and have been tested in the context of coastal boundary layer. Since the traditional definition 5.8 of eddy viscosity is different from that used in OBL models, both eddy coefficients were calculated using the present data. Following the traditional approach, the molecular viscosity was neglected in eddy–coefficient calculations.
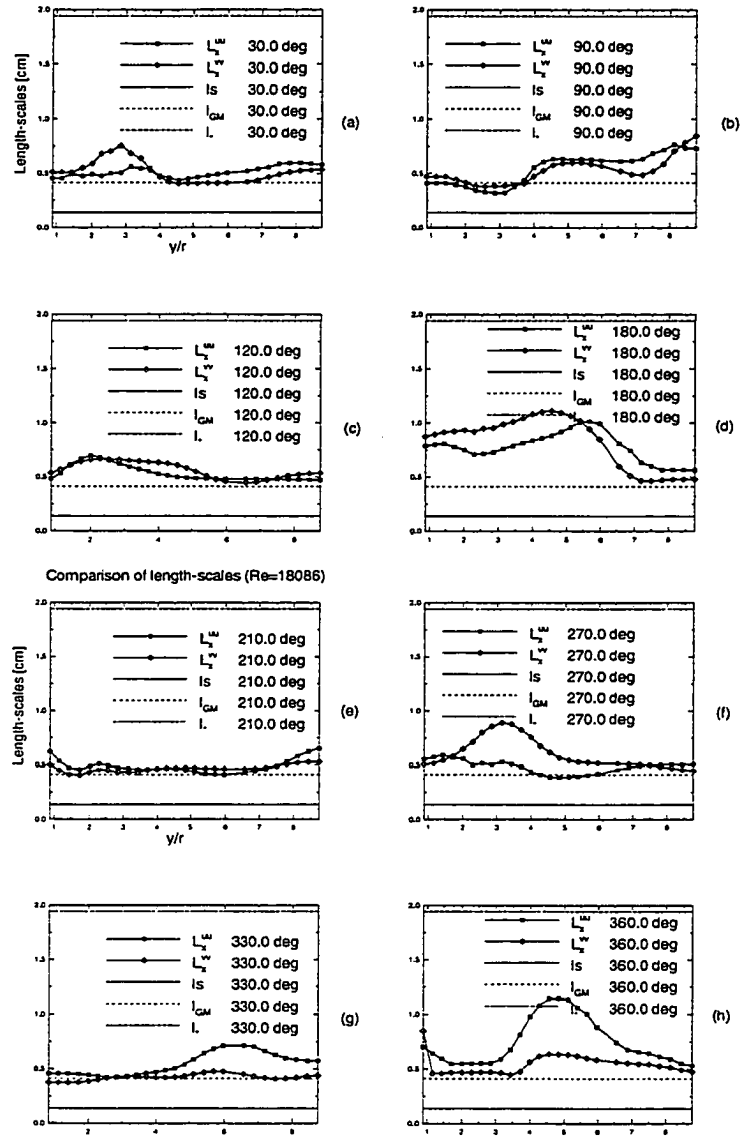
FIGURE 5.19. Comparison of experimentally determined length–scales and theoretical models 5.17–5.19: (a) 30°, (b) 90°, (c) 120°, (d) 180°, (e) 210°, (f) 270°, (g) 330°, (h) 360°. The Stokes length is also included. The experimental parameters are the same as in figure 5.18.

Integral length-scale $L_x^{uu}=f(Re,A/r)$

(a)

Integral length-scale $L_x^{vv}=f(Re,A/r)$

(b)
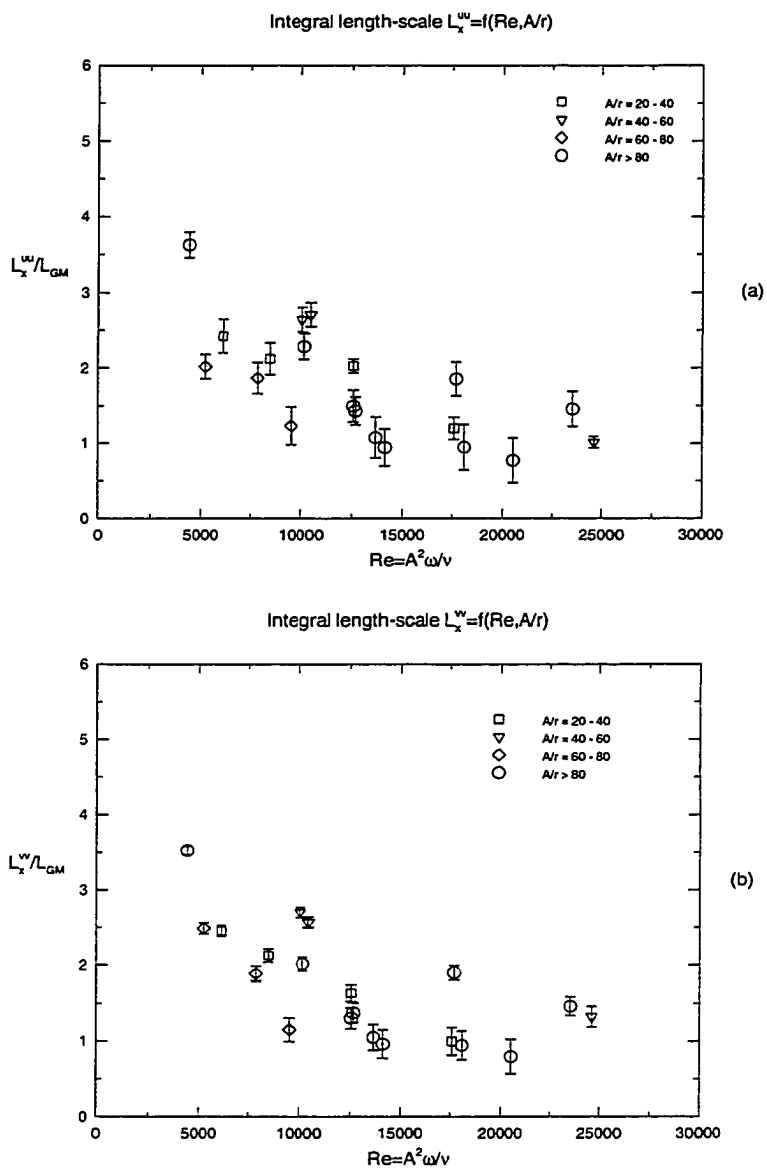
FIGURE 5.20. Integral length–scales, averaged over 10 cycles, plotted as functions of Re: (a) $L_x{}^{uu}/l_{GM}$ and (b) $L_x{}^{vv}/l_{GM}$.

Figure 5.21 shows how ν_i varies with the normalized distance from the wall at different phases. Note that ν_i is highly space and time dependent, having both positive and negative values. The occurrence of negative eddy coefficients has been noted previously by Sleath (1987), and Jonsson & Carlsen (1976). The fact that adjacent layers of the OBL correspond to and move with at different phases of oscillations poses difficulties for defining eddy diffusivities in a consistent way. Inspection of figure 5.21 indicates that the eddy diffusivities tend to be significantly larger near the edge of the boundary layer, though the turbulence intensities there are much smaller. The reason for this behaviour is the smallness of $\partial \tilde{u}/\partial y$, which artificially increases ν_i.

Figure 5.22 shows the eddy viscosity ν_T based on equation 5.7, which tends to be much larger due to contributions of dipole–like motions to the $\tilde{v}$ component. Comparison of the measurements with the space–time varying eddy diffusivity of Trowbridge & Madsen (1984) (equations 5.11–5.13) are also shown in figure 5.22. It is clear that the experimental eddy viscosity ν_T based on the total stress behaves much differently than that predicted by Trowbridge & Madsen (1984) $\nu_{T\&M}$; it takes both positive and negative values. The observed disagreements call for the development of new space–time dependent ν_T parametrizations, perhaps focusing on momentum transports by vortex structures as proposed in this study.
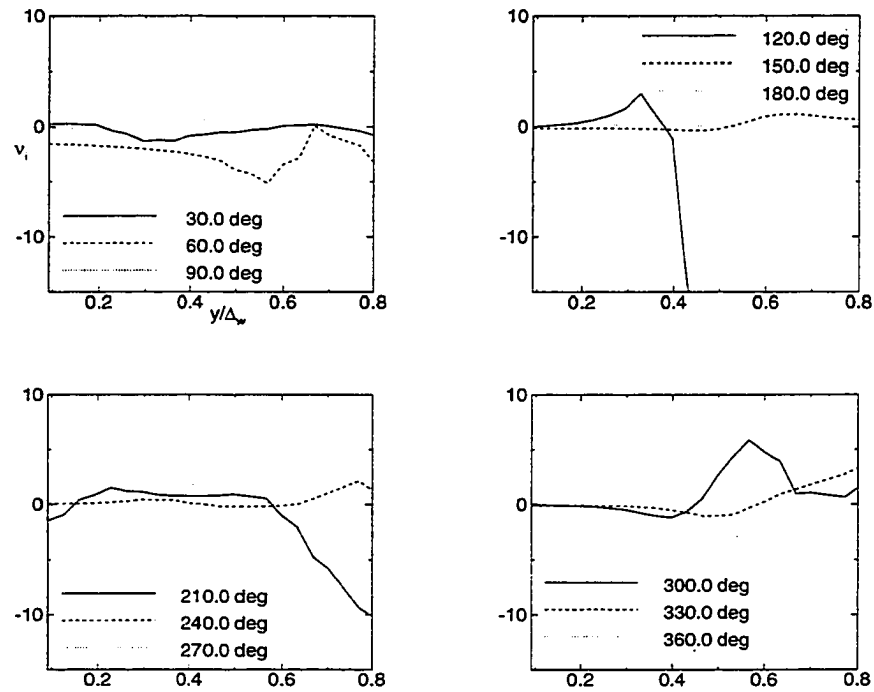
FIGURE 5.21. Variation of eddy viscosity in the direction normal to the wall, obtained by equation 5.8: (a) $\omega t = 30 - 90°$, (b) $\omega t = 120 - 180°$, (c) $\omega t = 210 - 270°$, (d) $\omega t = 300 - 360°$. Experimental conditions: A=14cm, T=6s, L=W=0.48cm, r=0.08cm, Re=20521.
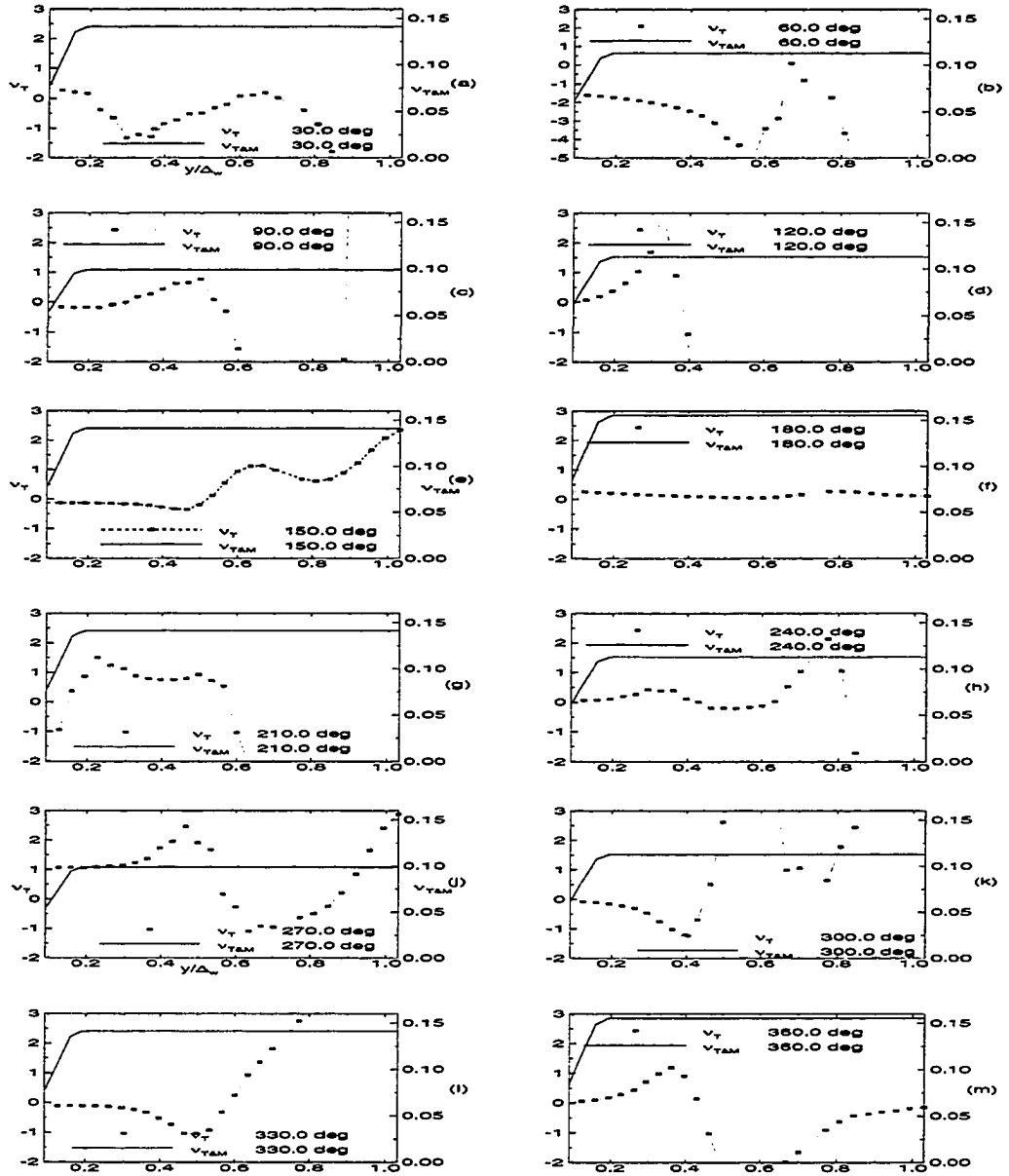
FIGURE 5.22. Comparison of experimental eddy viscosity ν_T with the model of Trowbridge & Madsen (1984) $\nu_{T\&M}$ (solid line), for different phases of the flow (a)–(m). Exp#22: A=14cm, T=6s, L=W=0.48cm, r=0.08cm, Re=20521.

5.3 RESULTS AND DISCUSSION ON WAVE–CURRENT BOUNDARY LAYERS

5.3.1 The scope of research

Wave–current boundary layers were investigated in the long tank with oscillatory bottom, as described in Chapter 4. Experiments were conducted with different outer flow parameters: the amplitude of oscillation A, the period of oscillations T, velocity of the mean flow (or current) U_m, and the bottom roughness (r, d) (d represents the distance between the roughness elements and $d = L = W$). The test conditions are listed in table 5.4. The main goal was to obtain more information on turbulence characteristics of the flow as a function of outer flow parameters. In order to compare present results with theoretical models, experiments and field measurements, the velocity field, obtained relative to the laboratory coordinates, was transformed into velocity field corresponding to the ocean conditions and wave tank conditions using equation 3.2.

The focus of present research is to broaden the studies on turbulent characteristics of the wave–current flow, to study the relationship between the kinematics and the dynamics of flow (eddy viscosity), to identify mechanisms and processes related to the wave–current boundary layer (integral length–scales, distribution of turbulent kinetic energy) and to compare experimental results with existing theoretical models. Special attention was given to appropriate scaling that enables extrapolation of results to different experiments and field measurements.

The variables that should define the characteristics of the wave–current boundary-layer are:

$$(A, T(\omega), r, d, \nu, U_m, \rho, D_h) \tag{5.21}$$

where ν is the kinematic viscosity, ρ is the density and D_h is the hydraulic diameter that specifies the width over which the steady current motion exists. By pure dimensional analysis, the main governing parameters of the wave–current boundary–layer problem are:

$$(Re_o = \frac{A^2\omega}{\nu}, Re_m = \frac{U_m D_h}{\nu}, \frac{U_m}{A\omega}, \frac{A}{r}, \frac{r}{d}) \tag{5.22}$$

The listed variables in the equation 5.21 represent the outer flow parameters, i. e. the characteristics of external forcing and correspond to ocean parameters which values could be found in results of field measurements. The results of present research will be presented in context of dimensionless parameters given in 5.22.

The parameter ranges of present research are shown in figures 5.23 and 5.24. In figure 5.23, the Reynolds number of oscillations $Re_o < 30,000$, is much less than the Reynolds numbers under field conditions. According to Nielsen (1992), the limiting conditions representing the real ocean are $(A, T) = (0.3m, 6s)$, corresponding to $Re_o \approx 100,000$. Some other field measurements, however, have indicated that $T \approx 10 - 12$ seconds. Conversely, with respect to the bottom roughness, it was possible to reproduce real ocean conditions with usual values $r/A = 0.06 - 0.08$. Another new way to look at the roughness influence is to use the ratio of height and distance between the roughness elements, i. e. r/d. Figure 5.24 overviews the ratio of the Reynolds number of mean current and Reynolds number of oscillations. The ratio taken relatively wide range $Re_m/Re_o = 1 - 12$, which can be of utility of extrapolating experimental results to real ocean conditions.

Exp. No.	A [cm]	T [s]	U_m [cm/s]	r	$Re_o = A^2\omega/\nu$	$Re_m = U_m D_h/\nu$
2	5	5	9.63	r8	3142	29853
5	10	6	8.74	r8	10472	27094
6	12	8	9.37	r8	11309	29056
7	14	8	9.31	r8	15394	28855
8	16	9	9.59	r8	17872	29723
9	18	10	9.33	r8	20357	28923
11	25	15	9.40	r8	26180	29140
15	9	5	8.82	r8	10178	27342
16	11	6	8.78	r8	12671	27228
17	13	7	8.59	r8	15169	26629
18	15	8	8.73	r8	17671	27063
19	17	8	8.61	r8	22698	26660
20	19	9	8.63	r8	25203	26711
21	20	12	8.70	r8	20945	26976
22	21	13	8.55	r8	21315	26505
26	7	5	7.98	r7	6157	24734
27	9	6	8.34	r7	8482	25848
28	11	8	8.39	r7	9503	26021
29	13	9	8.44	r7	11798	26159
30	10	7	8.13	r7	8976	25203
32	4	4	8.55	r7	2513	26518
33	5	4	8.34	r7	3927	25865
34	6	5	8.74	r7	4524	27097
35	7	6	8.35	r7	5131	25880
36	8	5	8.48	r7	8042	26286
37	9	6	8.16	r7	8482	25288
39	8	5	9.75	r2	8042	30216
40	9	5	10.04	r2	10178	31118
41	10	6	9.89	r2	10472	30663
42	11	7	9.72	r2	10861	30138
43	12	8	9.85	r2	11310	30521
44	13	8	9.65	r2	13273	29941
45	15	9	9.68	r2	15708	30001
47	10	7	7.30	r2	8976	22617
48	12	7	7.22	r2	12925	22394
49	14	8	7.51	r2	15394	23271
50	16	9	7.14	r2	17872	22126
51	18	10	7.28	r2	20358	22574

TABLE 5.4. Test conditions for wave–current boundary layer investigation.

Parameter range for the wave-current experiments

r/d ratio of height and distance between roughness elements
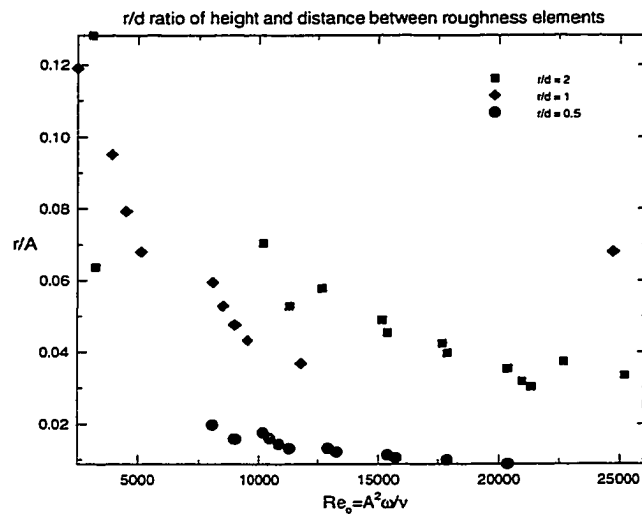
FIGURE 5.23. An overview of the ranges of the Reynolds number of oscillations $Re_o = A^2\omega/\nu$ and relative roughness r/A.

Parameter range for the wave-current experiments

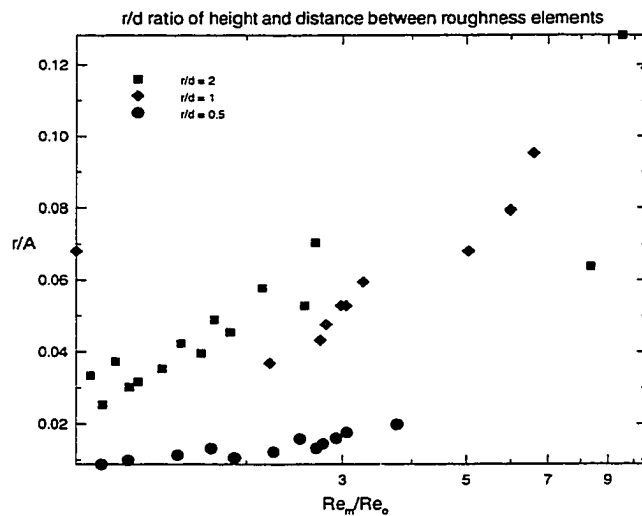r/d ratio of height and distance between roughness elements

FIGURE 5.24. An overview of the ranges of the ratio of Reynolds numbers of mean current Re_m to that of oscillations Re_o and relative roughness r/A.
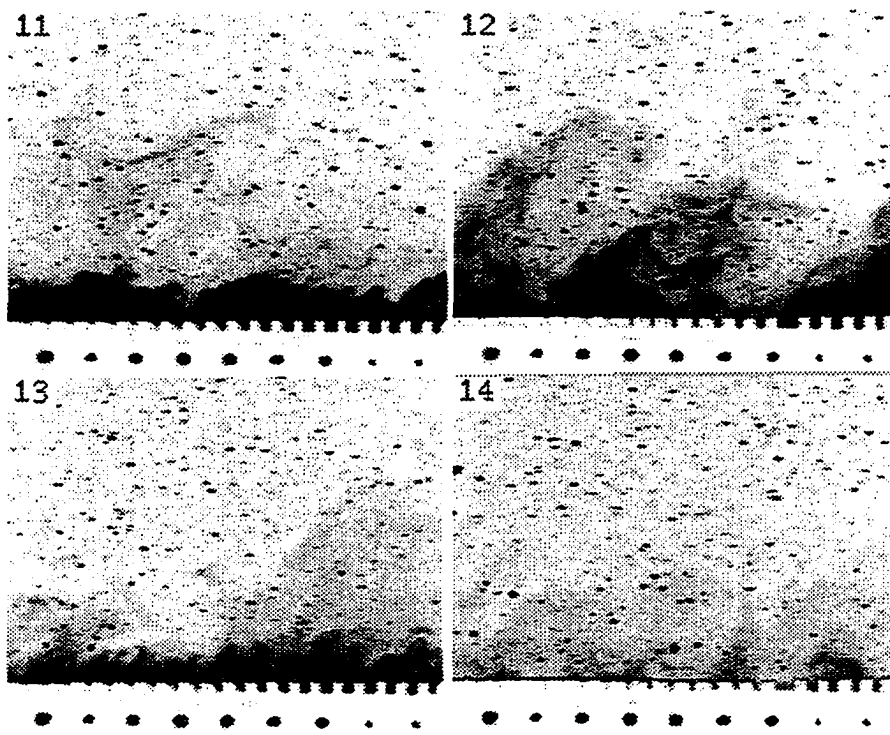
FIGURE 5.25. Visualization of the wave–current boundary layer: $A = 12$ cm, $T = 8$ s, $U_m = 9.13$ cm/s, $r/d = 1$.

5.3.2 Flow observations

An example of a sequence of photographs taken during an experiment is shown in figure 5.25. For clarity, images are presented by negative grey scale, i. e. in real application the particles are white, background is dark and the visualization dye is white. The first image represents flow at phase $\omega t = 360^o$, when the plate reverses its motion (the plate was oscillated with velocity $u_P = A\omega sin(\omega t)$). The formation of vortices can be observed in the immediate vicinity of bottom; the dye is trapped within an eddy rather than carried away by the mean current. The second image corresponds to $\omega t = 180^o$, and one cannot observe any formation of vortices; the dye is ejected out and mixed in the current stream. Same conclusion can be drawn from the third ($\omega t = 360^o$) and the forth ($\omega t = 180^o$) image, which are repetitions of the previous sequence. The difference in the thickness of the eddies was due to gradually dwindling dye supply under the mean current that carried away the dye.

The flow visualization studies show that the formation of vortices occurs when the fluid driven by the plate decelerates at the end of half–cycle that moves against the current ($\omega t = 360^o$). The shear between the layer adjacent to the roughness elements and the mean stream appears to be the cause for such vortex formation. However, at $\omega t = 180^o$, the fluid layers near the surface are moving in the same direction as the current and there is no vortex formation. This is different from the case of pure oscillatory boundary layers, where the formation of vortices are pronounced at the end of each half–cycle. The natural question that rises from the flow visualization is: what are the consequences on the boundary–layer dynamics if a mean current is simply added to the wave motion. In pure wave motion, the vortices are interacting with each other during the whole cycle and their action is spreading away from the bed. In the case of combined flow, vortices are pronounced only at $\omega t = 360^o$ and

the vortices so formed are advected by the mean current. Therefore, if the wave dominated sublayer exists (as was assumed by Grant & Madsen (1979)), one can expect that this layer will be much thinner, as in the case of pure wave motion. The vortices close to the bottom cause vigorous mixing of fluid parcels, the consequence being that the current velocity close to the bottom can be much higher than that in the case of steady current alone. Therefore, we might expect that the addition of waves to the current can decrease the thickness of the boundary layer.

5.3.3 Boundary–layer thickness

The discussion on the boundary–layer thickness will be based on the assumption of Grant & Madsen (1979) (see figure 1.3) that a thin sublayer exists in the immediate vicinity of the bed strongly influenced by the wave forcing (wave sublayer). Above the wave sublayer, the steady current "feels" the influence of apparent roughness created by the interaction between the wave sublayer and bottom physical roughness. The data presented in this section are based on the following definitions of the thickness of boundary layer (sublayer):

- The thickness of the wave sublayer (δ_w) within the wave–current boundary layer is the distance from the bottom where local instantaneous velocity reaches $0.99\%A\omega\sin(\omega t)$ and $\partial\tilde{u}/\partial y \approx 0$.

- The total thickness of the wave–current boundary layer (Δ_{cw}) is the distance from the bottom where local instantaneous velocity reaches $0.99\%U_m$ and $\partial\overline{u}/\partial y \approx 0$.

In general, the ratio of the total boundary–layer thickness to the wave sublayer thickness is a function of outer parameters as:

$$\frac{\Delta_{cw}}{\delta_w} = f(U_m, A, \omega, r, d, \nu) \tag{5.23}$$

that can be presented in terms of:

$$\frac{\Delta_{cw}}{\delta_w} = F(\frac{U_m}{A\omega}, \frac{A}{r}, \frac{r}{d}) \tag{5.24}$$

The data analysis showed that a fit to equation 5.24 is better represented by the data if the distance between the roughness elements d is substituted by the length–scale u_{*cw}/ω. The physical meaning of this length–scale is that it represents the combined influence of the velocity scale in the immediate vicinity of the bottom u_{*cw} and the time–scale of fluid motions near the bottom ω. Moreover, this length–scale contains the fluid properties ρ and ν, contained in the u_{*cw}. The results of such a fit are shown in figure 5.26 and a relation of the form:

$$\frac{\Delta_{cw}}{\delta_w} = (\frac{r\omega}{u_{*cw}})^{0.217}(\frac{U_m}{A\omega})^{0.01}(\frac{A}{r})^{0.00047} \tag{5.25}$$

is recognized. The experimental data show that the wave sublayer can be $20-80\%$ of the total wave–current boundary–layer thickness, depending on the outer parameters of flow. Grant & Madsen (1979) assumed the following expression for the wave sublayer thickness:

$$\delta_w = C_1 \frac{\kappa u_{*cw}}{\omega} \tag{5.26}$$

Thickness of the boundary layer for wave-current case

Δ_{cw} total thickness of the W+C boundary layer

δ_w thickness of the wave sublayer in the W+C boundary layer
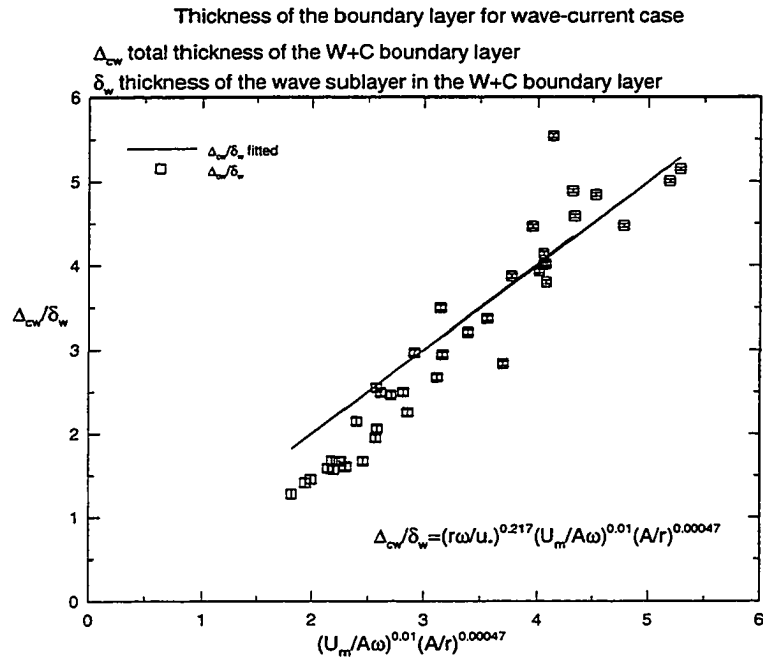
FIGURE 5.26. Ratio of the total thickness of the wave–current boundary layer Δ_{cw} to the thickness of wave dominated sublayer δ_w. The line represents the equation 5.25 and symbols are experimental data.

where the constant takes values $C_1 = 2$–4. A comparison of their theoretical prediction of the wave sublayer thickness with that obtained experimentally is shown in figure 5.27. It was evident that $C_1 = 4$ is better suited than the $C_1 = 2$; the best fit is represented by $C_1 = 4.36$ shown in figure 5.27. Moreover, the thickness of the wave sublayer is increasing if the scale u_{*cw}/ω is increasing.

A comparison between the wave–current boundary-layer thickness Δ_{cw} and that of steady current Δ_c, evaluated with the same velocity of the current, is presented in figure 5.28. As was predicted by visual observations, the addition of waves to the steady current decreases (by 25–55%) the overall thickness of the boundary layer

Comparison of theoretical and experimental thickness of the wave sublayer

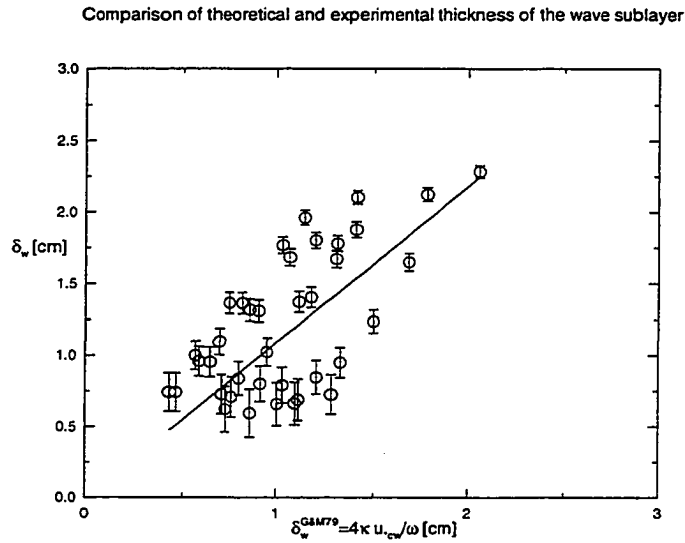FIGURE 5.27. The ratio of the theoretical thickness of the wave sublayer $\delta_w{}^{GM79}$ to the experimental thickness of the wave sublayer δ_w.
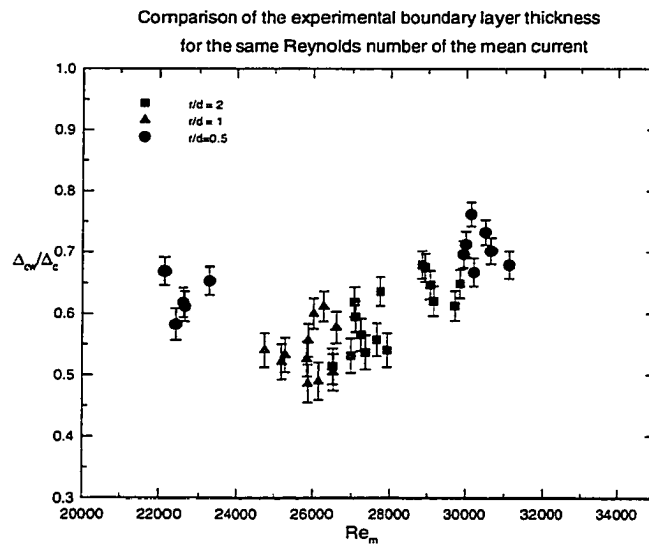

FIGURE 5.28. The ratio of the thickness of the wave–current layer Δ_{cw} to the thickness of the steady current boundary layer Δ_c.

in comparison to the boundary layer of steady current. The existence of the wave sublayer enhances momentum, mixing near the bed and leads to more drastic velocity change in a thinner layer near the bottom. According to experimental results, if r/d is smaller, Δ_{cw} is closer to Δ_c. Also, overall thickness of the wave–current boundary layer is larger compared to pure wave boundary layer with the same Reynolds number of oscillations (see figure 5.29). Even though the propagation of vortices created in the wave sublayer is bounded by the steady current, the total thickness Δ_{cw} is still larger than Δ_w. It seems that the difference between the Δ_{cw} and Δ_w is smaller if r/d is larger.

Finally, the ratio between the thickness of the pure wave boundary layer and the wave sublayer in wave–current boundary layer is presented in figure 5.30. The wave sublayer is thinner than the pure wave boundary layer for the same Re_o if $r/d \geq 1$. The reason may be the creation of additional "stable" eddies between the roughness elements (for $r \geq d$), as it was reported and discussed by Perry *et al.* (1987). Hence, stable vortices between the roughness elements do not strongly interact with the local mean velocity that follows the contour of the bottom, decreasing the thickness of the wave sublayer. In the case when $r \leq d$, the vortices are formed by interaction of mean current and roughness elements, in addition of vortex creation at $\omega t = 360^o$, increasing the thickness of wave sublayer. The scatter of the data presented in figures 5.29 and 5.30 is due to the multitude of parameters influencing this particular type of flow (see equation 5.22.

5.3.4 Velocity profile

The analysis of velocity profiles to be presented here is based on the models of Grant & Madsen (1979) and Nielsen (1992). The procedure of obtaining the velocity components, according to 2.69, involves the measurement of two–dimensional mean and

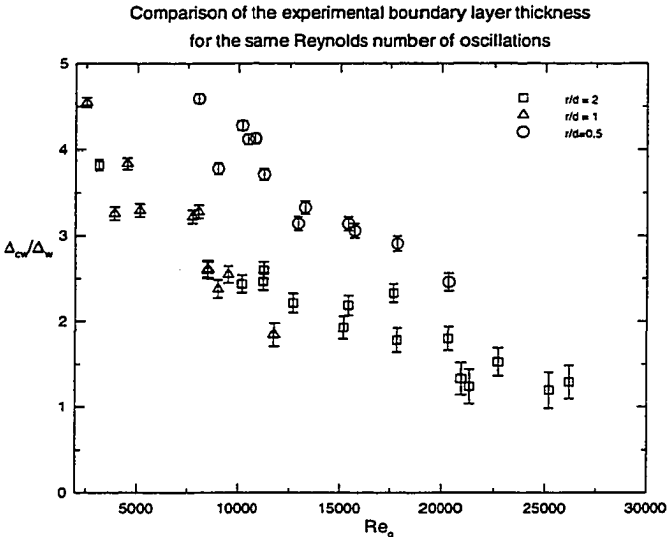**FIGURE 5.29.** Ratio of the thickness of the wave–current layer Δ_{cw} to the thickness of the wave boundary layer Δ_w.
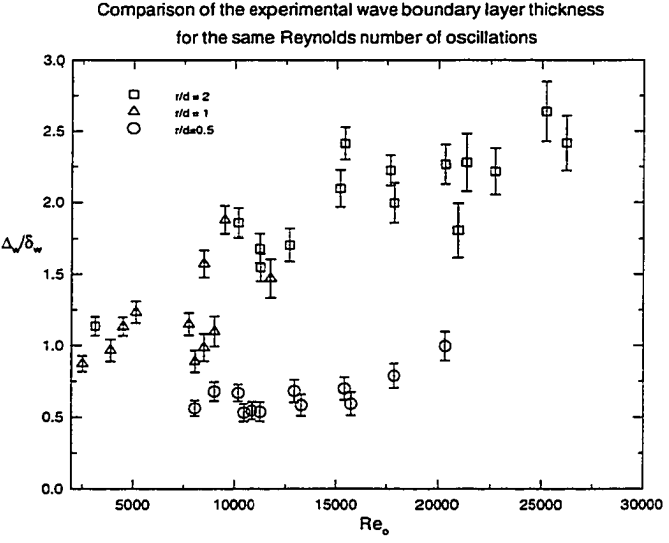

FIGURE 5.30. Ratio of the thickness of the pure wave boundary layer Δ_w to the thickness of the wave sublayer δ_w.

instantaneous velocities using PTV. The mean velocity was obtained by ensemble averaging of instantaneous velocities over ten successive cycles of oscillations. The periodic component of velocity is obtained by phase averaging of ten successive cycles according to 2.70. Based on this decomposition it is possible to study the validity of certain theoretical models available for the prediction of shear stress and eddy viscosity. In addition, in order to check the model of Grant & Madsen (1979), the mean velocity was fit to the logarithmic profile and the best fit was used to determine the apparent roughness.

An example of the mean velocity profile is presented in figure 5.31. The profile was obtained by averaging ten cycles (which means averaging 2100 frames, in this particular example). The mean velocity interpolated into the Eulerian grid consists of 20 points in the horizontal and 60 points in the vertical direction, and the window of particle tracking was 15×12 cm. The first column of velocities within the window was omitted due to the fact that the particle tracking program assumes certain initial values of velocity at the entrance to the window, thus leading to non–uniform profiles.

The periodic velocity averaged over 10 cycles is shown in figure 5.32, for some phases of oscillations. Note the change of the direction and intensity of the periodic velocity from one phase to the other. It is, also, interesting to note that the amplitude wave velocity $A\omega=8.37$ cm/s is almost the same as current velocity $U_m=8.13$ cm/s, so that the periodic velocity is symmetrical with respect to the initial moment where the wave forcing (wave velocity) is zero ($\omega t = 0^o$).

The effect of the wave forcing (periodic velocity) can be seen clearly in figure 5.33. The instantaneous velocity is presented for 4 phases of oscillations and it can be seen that in one half of the cycle the current velocity is enhancing and in the other half of the cycle it is reducing the instantaneous velocity. Since for the case shown, the wave

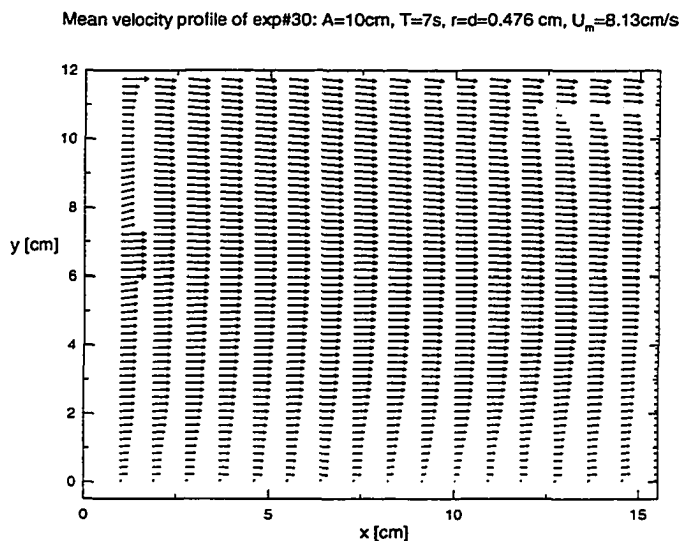Mean velocity profile of exp#30: A=10cm, T=7s, r=d=0.476 cm, U_m=8.13cm/s

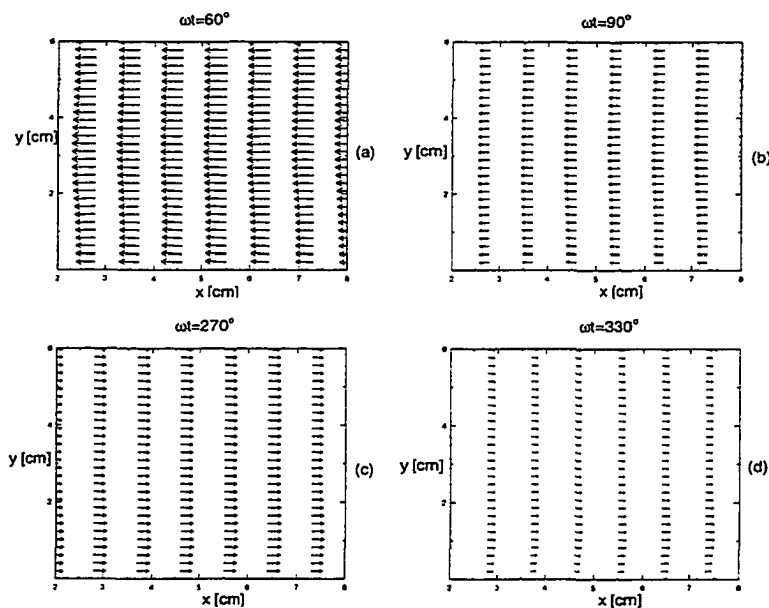FIGURE 5.31. The mean velocity for Exp#30: A=10 cm, T=7 s, r=d=0.476 cm, U_m=8.13 cm/s.

FIGURE 5.32. The periodic velocity for Exp#30: A=10 cm, T=7 s, r=d=0.476 cm, U_m=8.13 cm/s.

amplitude velocity and current velocity are different, and hence the instantaneous velocity is not symmetric with respect to $\omega t = 0^o$.

In order to verify the model of Grant & Madsen (1979), it is necessary to take a closer look at the mean velocity component of the wave–current boundary layer. Figure 5.34 shows that the mean velocity profile is relatively homogeneous in the streamwise direction and a comparison with the steady current boundary layer case is given in figure 5.35. It appears from figure 5.35 that the mean velocity profile in the case of wave–current boundary layer is much steeper closer to the bottom. The possible reason for this observation is better momentum mixing closer to the bottom due to the ejection of vortices as the consequence of wave periodic forcing.

In order to compare experimental results with the theoretical model of Grant & Madsen (1979), the mean velocity was fitted to the logarithmic profile according to 2.63 and 2.64 to evaluate κ and the apparent roughness k_{*cw}. Grant & Madsen (1979) decomposed the velocity into the wave and current component as

$$u = u_c + u_w \tag{5.27}$$

and proposed following definitions of friction velocity to describe the current:

$$u_{*c}^2 = \kappa |u_{*c}| y \frac{\partial u_c}{\partial y}, \qquad y > \delta_w \tag{5.28}$$

$$u_{*c}^2 = \kappa |u_{*cw}| y \frac{\partial u_c}{\partial y}, \qquad y < \delta_w \tag{5.29}$$

Therefore, in the data fitting, u_{*c} was obtained using 5.28 for $y > \delta_w$ and using 5.29 for $y < \delta_w$. The friction velocity u_{*cw} was obtained according to the definition of
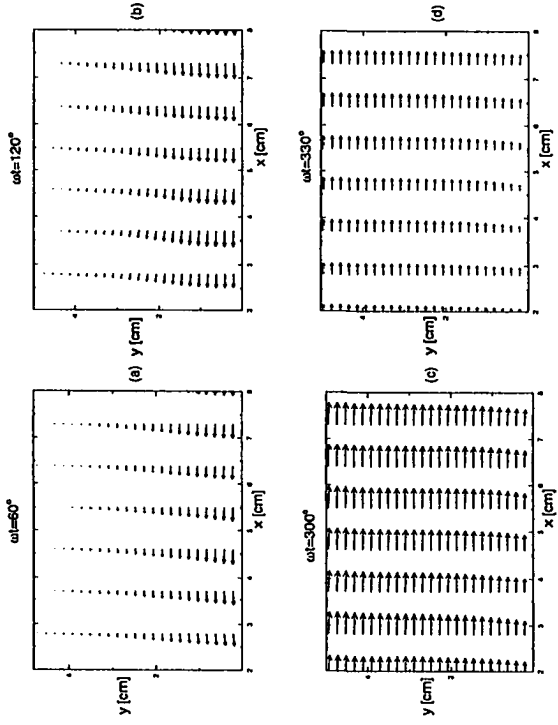
FIGURE 5.33. The instantaneous velocity for Exp#8: $A=16$ cm, $T=9$ s, $r=0.635$ cm, $d=0.318$ cm, $U_m=9.59$ cm/s.

Mean velocity profile at 18 streamwise locations

Exp#8: A=16cm, T=9s, r=0.635cm, d=0.318cm, U_m=9.59cm/s
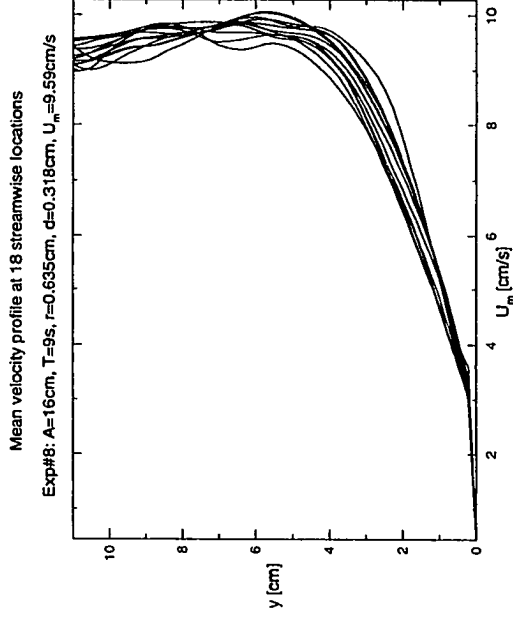
FIGURE 5.34. The mean velocity at different streamwise locations within the velocity field for Exp#8: $A=16$ cm, $T=9$ s, $r=0.635$ cm, $d=0.318$ cm, $U_m=9.59$ cm/s. The distance between horizontal locations is $\Delta x = 0.2$ cm.
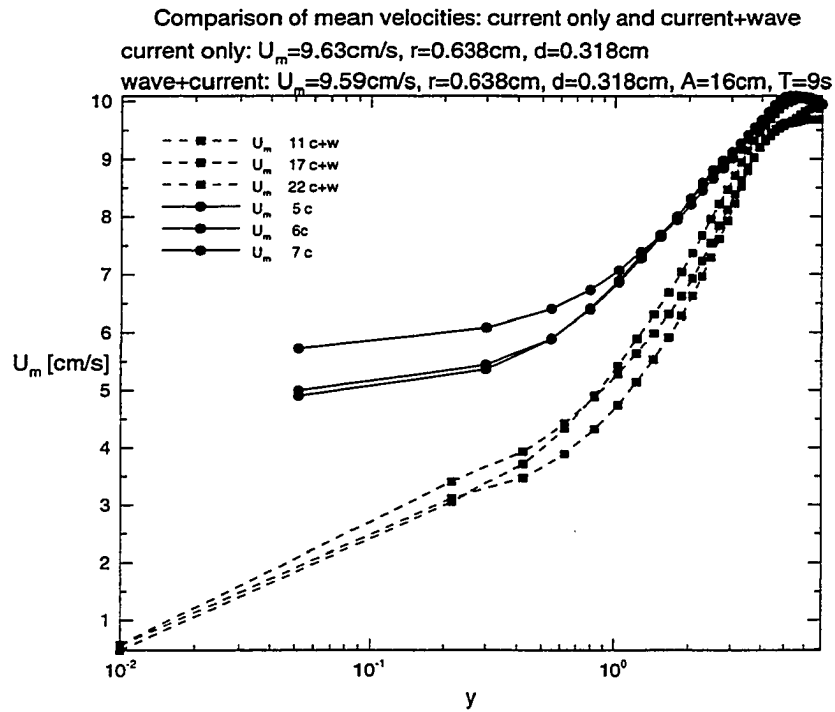
FIGURE 5.35. A comparison of velocity profiles in steady current and wave–current boundary layers.

Grant & Madsen (1979):

$$|u_{*cw}|^2 = \frac{|\tau_{b,max}|}{\rho} \tag{5.30}$$

The values of κ for the steady (κ_c), and wave–current κ_{cw} were compared for cases $y < \delta_w$ and $\delta_w < y < \Delta_{cw}$. The curve fit for $y < \delta_w$ showed that κ takes values smaller than 0.4, representing a new velocity distribution with much higher values close to the bottom; see table 5.5.

In general, the apparent roughness can be presented in the form:

$$\frac{k_{*cw}}{k_{*c}} = f(\frac{A\omega}{u_{*cw}}, \frac{r}{A}) \tag{5.31}$$

So far, there were only a few attempts to study this function form. Grant & Madsen (1979) proposed:

$$\frac{k_{*cw}}{k_{*c}} = (24\frac{u_{*cw}}{A\omega}\frac{A}{k_{*c}})^{(1-\frac{u_{*c}}{u_{*cw}})} \tag{5.32}$$

and Sleath (1991) included the dependence of apparent roughness on physical bottom roughness r as

$$\frac{k_{*cw}}{k_{*c}} = 1 + 0.19\frac{A\omega}{u_{*cw}}\sqrt{\frac{A}{r}} \tag{5.33}$$

A comparison of the apparent roughness obtained by fitting experimental data to 2.63 with the models of Sleath (1991) and Grant & Madsen (1979) is presented in figure 5.36. It seems that model of Sleath (1991) underestimates the apparent rough-

exp.	κ_c SS	k_{*c} SS	κ_{cw} $y < \delta_w$	k_{*cw} $y < \delta_w$	κ_{cw} $\delta_w < y < \Delta_{cw}$	k_{*cw} $\delta_w < y < \Delta_{cw}$
02	0.379	0.213	0.417	0.107	0.178	1.510
05	0.379	0.213	0.367	0.113	0.093	8.063
06	0.379	0.213	0.271	0.150	0.138	2.568
08	0.379	0.213	0.239	0.171	0.095	5.339
11	0.379	0.213	0.261	0.191	0.074	10.11
15	0.448	0.116	0.261	0.138	0.235	1.273
16	0.448	0.116	0.223	0.197	0.093	5.729
17	0.448	0.116	0.189	0.208	0.115	3.033
18	0.448	0.116	0.201	0.214	0.089	6.045
19	0.448	0.116	0.104	0.380	0.076	4.976
20	0.448	0.116	0.250	0.124	0.116	5.004
22	0.448	0.116	0.218	0.267	0.046	15.64
27	0.398	0.072	0.049	0.563	0.213	0.742
32	0.423	0.203	0.234	0.342	0.305	1.360
33	0.423	0.203	0.015	0.982	0.201	2.027
34	0.423	0.203	0.213	1.230	0.383	1.377
35	0.423	0.203	0.278	1.425	0.232	1.032
47	0.425	0.132	0.045	2.350	0.248	1.681
51	0.425	0.132	0.014	2.763	0.144	7.681

TABLE 5.5. Fitted values of Karman's constant and apparent roughness obtained using 2.63, 2.64. The Karman's constants κ_c and κ_{cw} correspond to steady current and wave–current case, respectively. k_c is Nikuradse roughness obtained for steady current case and k_{*cw} is the apparent roughness.

ness, while experimental values are slightly smaller than the prediction of Grant & Madsen (1979).

The experimental apparent roughness (see figure 5.37) showed a best fit of the form:

$$\frac{k_{*cw}}{k_{*c}} = (0.1\frac{A\omega}{u_{*cw}})^6 \tag{5.34}$$

The apparent roughness increases rapidly with the ratio of amplitude to height of the bottom roughness and it depends on the ratio of amplitude of wave velocity to the friction velocity. Experimental results obtained by Arnskov *et al.* (1993) also show a similar dependence on the ratio of mean and friction velocity, but they did not describe that by any analytical expression.

5.3.5 Velocity fluctuations and turbulent kinetic energy

There are several measurements of velocity fluctuations in wave–current flows, for example, Kemp & Simons (1982), Kemp & Simons (1983), George & Sleath (1979). In the present study the velocity fluctuations were obtained by the software *Trk2DVel*, using simple Reynolds decomposition:

$$u' = u - \overline{u} \tag{5.35}$$

and the velocity field was transformed to an equivalent velocity field relative to a coordinate system fixed to the oscillating plate. The fluctuations were calculated in steps of 0.033 seconds, which is the highest possible resolution of Particle Tracking software.

The horizontal velocity fluctuations were presented in figure 5.38 and 5.39. Intense fluctuations appear at 7 and 14 seconds, corresponding to the phases where the vortices were formed and ejected out of the top of roughness elements. At these instances, the fluctuations $\approx 50\%$ of the free stream velocity; due to the fact that u' contains both u' and $\tilde{u}$. The fluctuations decay away from the bottom from approximately $25\% U_o$ at y=0.25cm to $10\% U_o$ at y=4cm, which is the top of the boundary layer for this particular case.
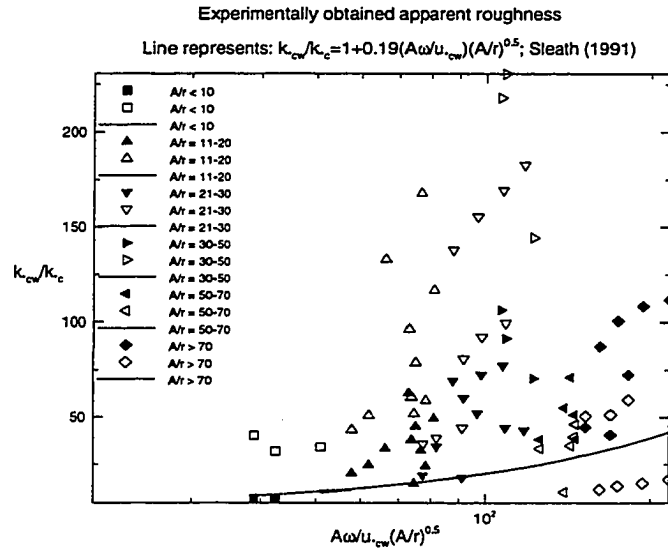
FIGURE 5.36. Experimentally obtained apparent roughness (solid symbols) compared to the theoretical models of Sleath (1991)–(line) and Grant & Madsen (1979)–(outlined symbols).
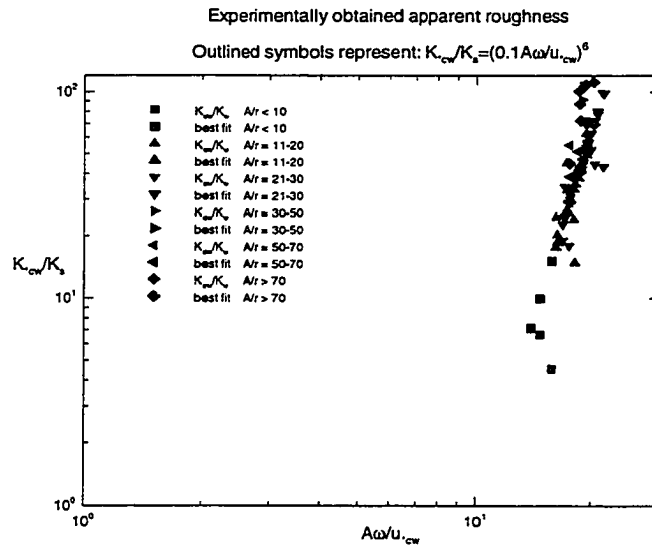
FIGURE 5.37. Empirically fitted apparent roughness as a function of $A\omega/u_{*cw}$ and A/r as in 5.31.
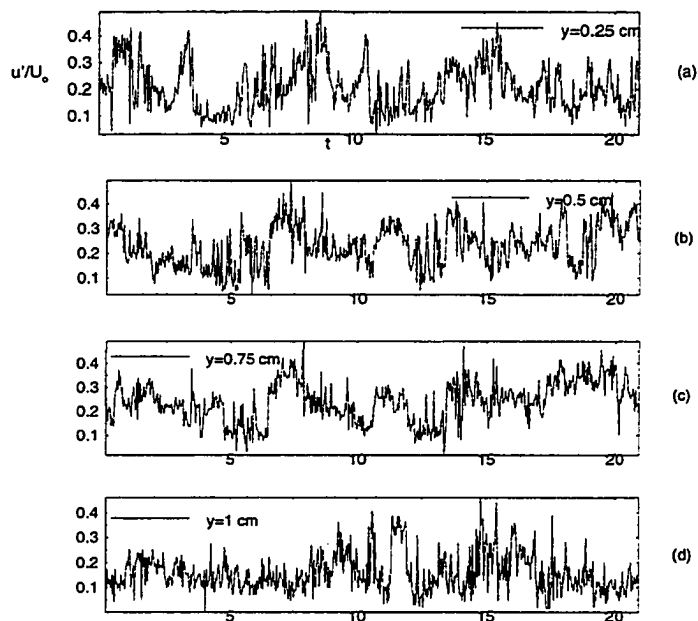
FIGURE 5.38. Horizontal velocity fluctuations for Exp#30: A=10 cm, T=7 s, r=d=0.476 cm, U_m=8.13 cm/s, y= (a) 0.25, (b) 0.5, (c) 0.75, (d) 1 cm.
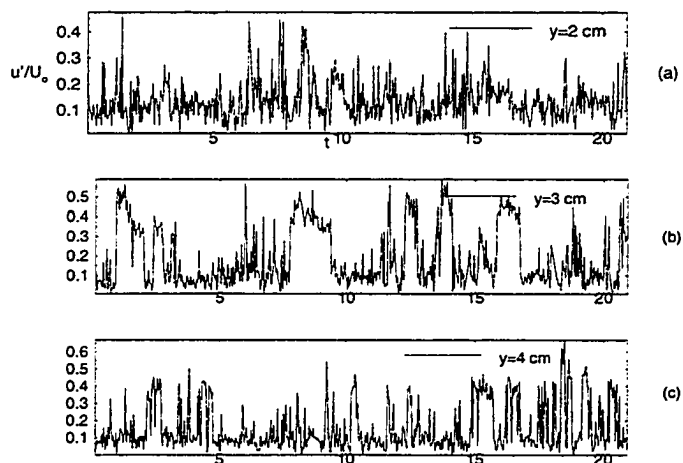
FIGURE 5.39. Horizontal velocity fluctuations for Exp#30: A=10 cm, T=7 s, r=d=0.476 cm, U_m=8.13 cm/s. y= (a) 2, (b) 3, (c) 4 cm.
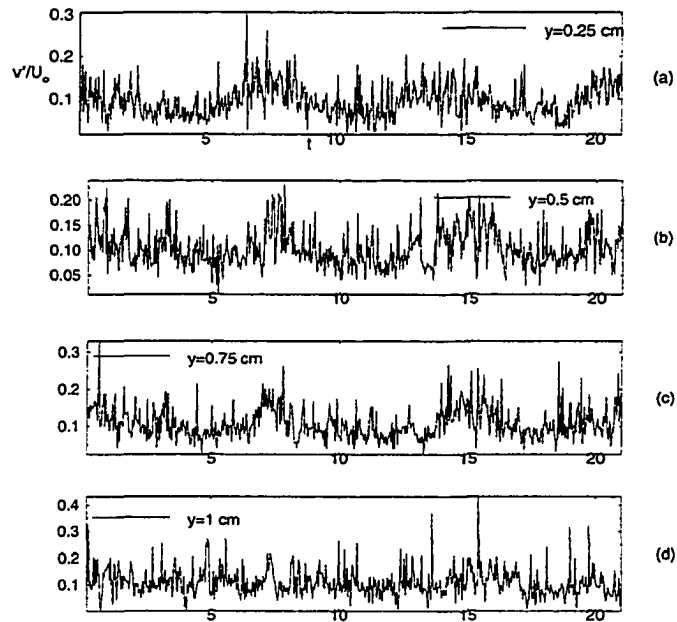
FIGURE 5.40. Vertical velocity fluctuations for Exp#30: A =10 cm, T=7 s, r = d =0.476 cm, U_m=8.13 cm/s, y= (a) 0.25, (b) 0.5, (c) 0.75, (d) 1 cm.
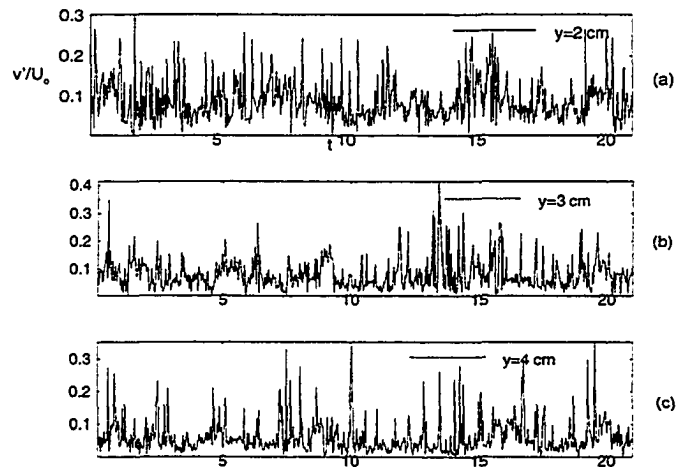
FIGURE 5.41. Vertical velocity fluctuations for Exp#30: A=10 cm, T=7 s, r = d =0.476 cm, U_m=8.13 cm/s, y= (a) 2, (b) 3, (c) 4 cm.

Similar tendency can be observed for the vertical velocity fluctuations (see figure 5.40 and 5.41). The only difference is that the maximum vertical velocity fluctuations reach up to 30–40%U_o, the typical values being a 15%U_o, and 5%U_o closer to the top of the boundary layer. The present results are consistent with the previous measurements of Kemp & Simons (1982) and Kemp & Simons (1983). It was noticed in all cases, both in past and present results, that the velocity fluctuations are periodic very close to the bottom, the period being the period of wave forcing. If the measurements are close to the top of the boundary layer, the fluctuations become random.

Another possible approach to study the turbulent characteristics of the flow is to observe the changes of the turbulent kinetic energy (TKE), which is simply defined as:

$$K_o = \frac{1}{2}(\tilde{u'}^2 + \tilde{v'}^2) \tag{5.36}$$

The horizontally averaged K_o was calculated for 12 phases of the flow using data obtained over a two–dimensional window. The results are shown in figure 5.42, which shows that K_o values are much higher for the wave–current case compared to the wave only case (figure 5.13). In latter case, the production of turbulent kinetic energy is intensified toward the end of each half–cycle ($\omega t = 180^o, 360^o$), with noticeable production at the phases of large orbital velocities ($\omega t = 90^o, 270^o$). In case of wave–current boundary layer, K_o becomes intensified close to the top of boundary layer at $\omega t = 90^o, 180^o, 270^o, 360^o$, indicating possible interaction of high mean velocity flow with vortices ejected out of the top of roughness elements.

Spatial distribution of the turbulent kinetic energy from one phase to the another is illustrated in figures 5.43 and 5.44. The horizontal homogeneity of the flow
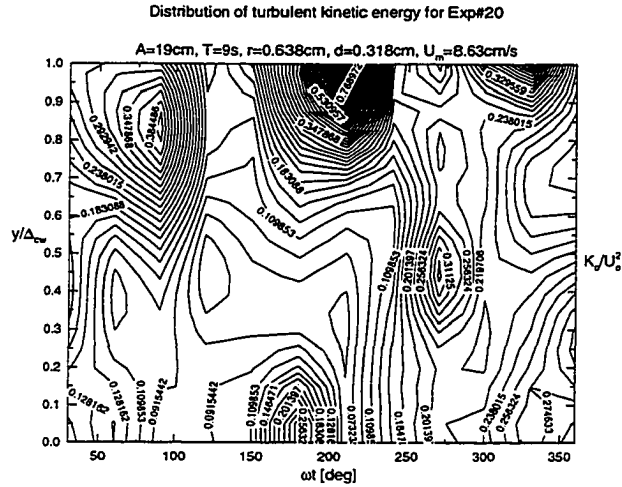
FIGURE 5.42. The turbulent kinetic energy for Exp#20: A=19 cm, T=9 s, r=0.638 cm, d=0.318 cm, U_m=8.63 cm/s.

FIGURE 5.43. The turbulent kinetic energy in a 2–D window for Exp#20: A=19 cm, T=9 s, r=0.638 cm, d=0.318 cm, U_m=8.63 cm/s. (a) $\omega t = 90^o$ and (b) $\omega t = 180^o$.

Turbulent kinetic energy in 2-D domain for Exp#20
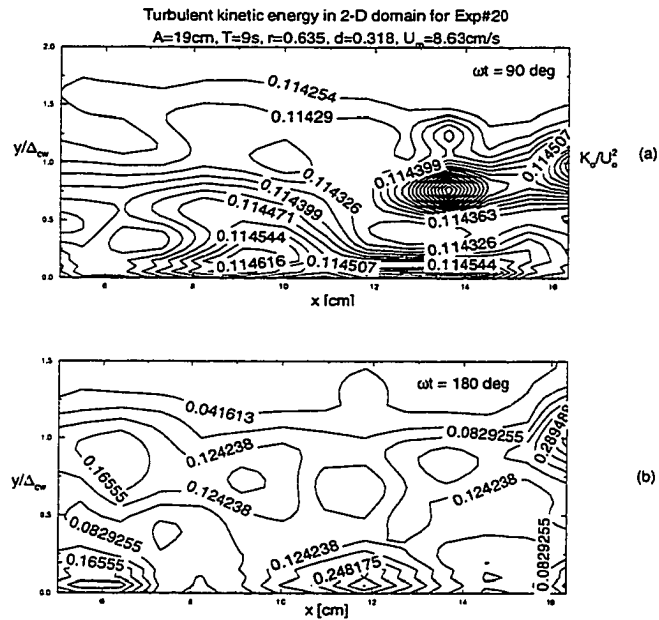A=19cm, T=9s, r=0.635, d=0.318, U_m=8.63cm/s
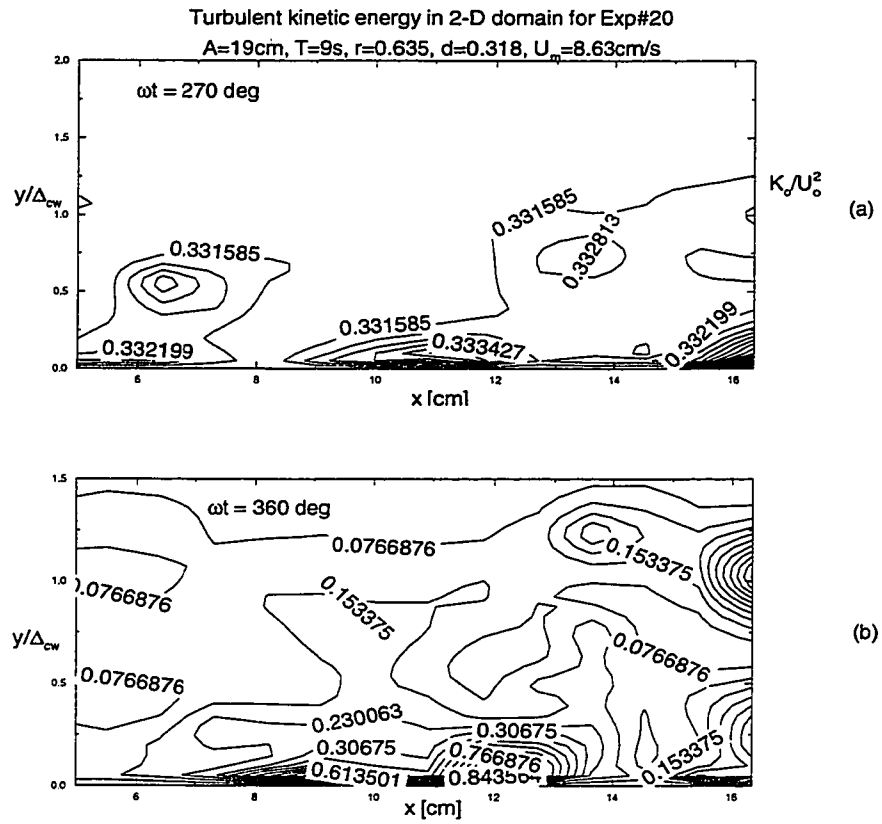
FIGURE 5.44. The turbulent kinetic energy in a 2–D window for Exp#20: A=19 cm, T=9 s, r=0.638 cm, d=0.318 cm, U_m=8.63 cm/s. (a) $\omega t = 270°$ and (b) $\omega t = 360°$.

implies that K_o is uniform in x–direction. According to these figures, this uniformity is satisfied only approximately at $\omega t = 90°, 180°, 270°$, but not satisfied at the end of the second half–cycle $\omega t = 360°$. The interesting observation is that K_o is confined to certain "cells", with the maximum TKE in its center. These isolated patches might represent the vortices that are ejected out of roughness elements and interact with the coming current. Due to the ejection of vortices, the production of the turbulent kinetic energy is highest just above the bottom roughness elements. Due to spatially intermittent ejection of single vortices upward, the velocity field has a tendency to be non–uniform in the horizontal direction, but it tends to have some periodicity.

5.3.6 The bottom shear stress and friction velocity

The bottom shear stress plays a major role in ocean boundary layers since it is directly responsible for sediment transport, scour and erosion. For the wave–current boundary layer, the bottom shear stress is defined as:

$$\tau_b = \rho u_{*cw}{}^2 = \mu \frac{\partial u}{\partial y}\Big|_{y=0} \tag{5.37}$$

where u_{*cw} is friction velocity and u is instantaneous velocity. Because of the strong time dependent nature of the problem, the instantaneous values will be considered first. The friction velocity takes the sign of bottom shear stress, and it is defined as:

$$|u_{*cw}|u_{*cw} = \frac{\tau_b}{\rho} \tag{5.38}$$

The bottom shear stress is a function of time and, because of the nominal horizontal non–uniformity, it can be a function of the streamwise coordinate x. The results shown in figures 5.45 and 5.46, however, show that the bottom shear stress and friction velocity are uniform in the horizontal (streamwise) direction. Thus, the bottom

Bottom shear stress for 12 phases of oscillations

Experiment #20: A=19cm, T=9s, w-d-r=0.318-0.318-0.635cm, U$_m$=8.63cm/s
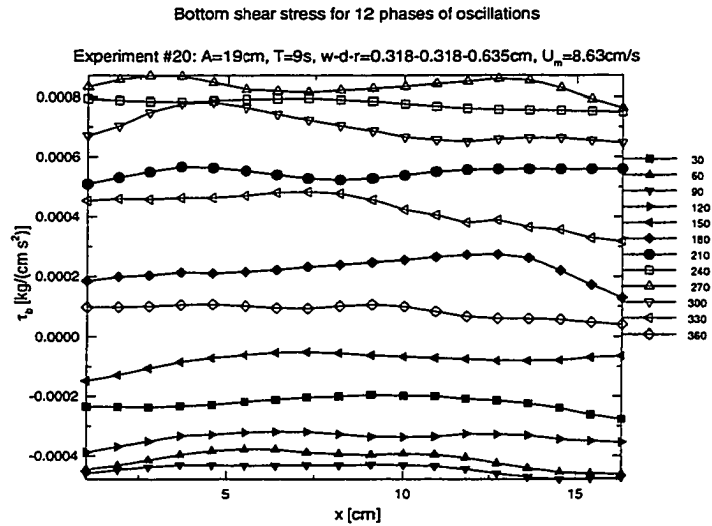
FIGURE 5.45. The bottom shear stress as a function of the streamwise coordinate and phase of oscillations for Exp#20: A=19 cm, T=9 s, r=0.638 cm, d=0.318 cm, U_m=8.63 cm/s.

Friction velocity for 12 phases of oscillations

Experiment #20: A=19cm, T=9s, w-d-r=0.318-0.318-0.635cm, U$_m$=8.63cm/s
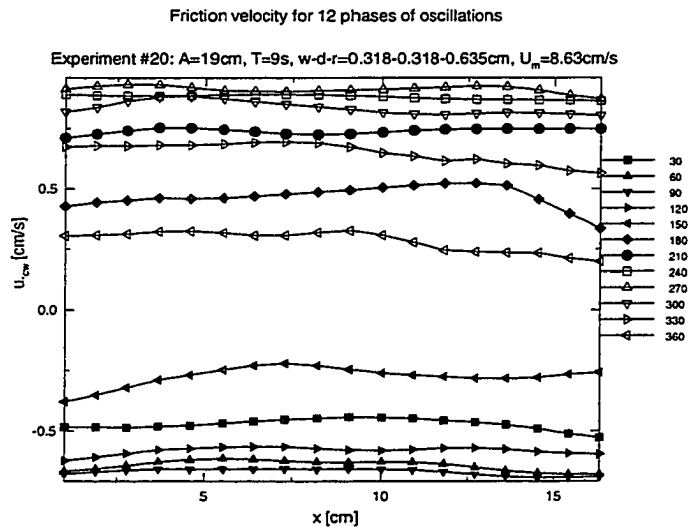
FIGURE 5.46. The friction velocity as a function of the streamwise coordinate and phase of oscillations for Exp#20: A=19 cm, T=9 s, r=0.638 cm, d=0.318 cm, U_m=8.63 cm/s.

shear stress and the friction velocity will be averaged in the streamwise direction for a particular phase of oscillation.

In general, the friction velocity of the wave–current case is a function of following outer flow parameters:

$$u_{*cw} = f(T(\omega), t, U_m, A, r, d, \nu, \rho) \tag{5.39}$$

that can lead to the form

$$u_{*cw} = u^A(\omega t) F(\frac{U_m}{A\omega}, \frac{A}{r}, \frac{r}{d}) \tag{5.40}$$

The change of the friction velocity with respect to the phase of oscillation is shown in figure 5.47 for 30 different experiments. The values of friction velocity are not symmetric for the first and second half–cycle. The first half–cycle corresponds to the phases when the free stream velocity has the same direction of propagation as the bottom plate. The velocity gradient at the bottom seems to be negative for this half–cycle due to the existence of a thin layer of fluid that flows in the opposite direction of that of the plate, thus enhancing the negative velocity close to the bottom (especially when velocity transformation is applied). The velocity gradient becomes positive just before $\omega t = 180^o$ due to the decellaration of the plate.

In the second half–cycle, the velocity of the plate and hence the thin layer above it opposes the velocity of the mean current. Motion of the current above this highly sheared region contributes to a huge positive velocity gradient and large friction velocity.

Friction velocity for the wave-current case
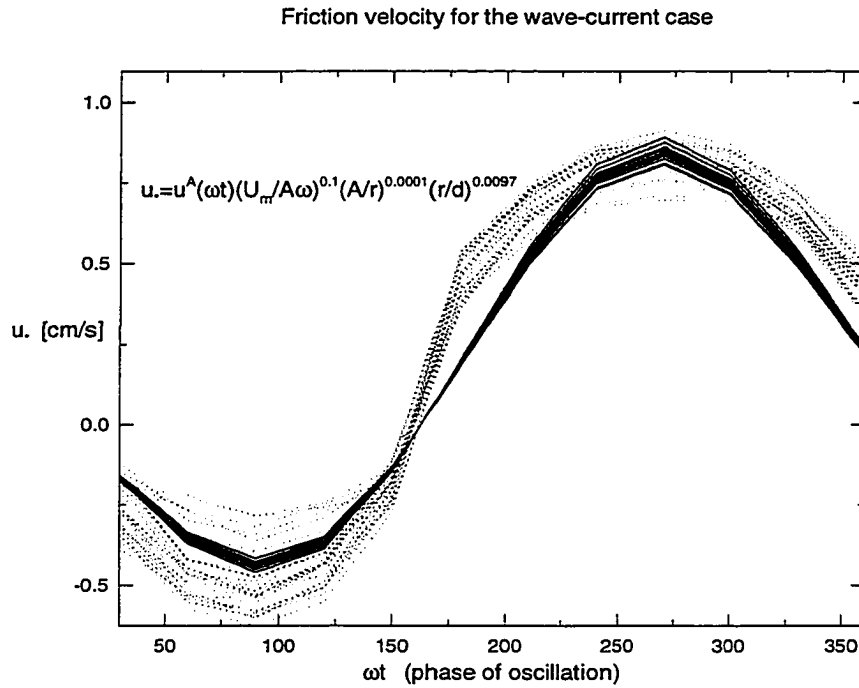
FIGURE 5.47. The friction velocity as a function of the phase of oscillations for different experiments.

The best curve-fit for the friction velocity that collapse the data can be given by:

$$u_{*cw} = u^A(\omega t)(\frac{U_m}{A\omega})^{0.1}(\frac{A}{r})^{0.0001}(\frac{r}{d})^{0.0097} \qquad (5.41)$$

where $u^A(\omega, t)$ is some velocity component that changes in time (for this particular case, the time varying velocity component was found in form:

$$u^A(\omega, t) = u_1 + u_2 sin(C_1\omega t + C_2)^2 \qquad (5.42)$$

where $u_1 = 0.2974$ cm/s, $u_2 = 0.48$ cm/s, $C_1 = 2\pi/694.85$ and $C_2 = -4.0013$. This expression indicates that the dominant external parameter is the ratio of the mean

current and the amplitude of the oscillatory velocity. The solid line in figure 5.47 represents the previous curve fit applied to all experiments.

The previous fit was obtained using the outer flow parameters according to equation 5.41. Another possibility to present the friction velocity is:

$$\frac{u_{*cw}}{U_m} = F(\frac{A}{r}, \frac{A^2\omega}{\nu})$$

(5.43)

The ratio of friction velocity and mean current velocity is increasing significantly with A/r (as shown in figure 5.48). The dependence on the Reynolds number of oscillations is shown in figure 5.49. It is possible to conclude that, qualitatively, u_{*cw}/U_m increases with, both, the Reynolds number of oscillations and the A/r.

Another common approach of quantifying the bottom shear stress is through the friction factor, defined by Jonsson (1966) and Kajiura (1968) as

$$\tau_{b,max} = \frac{1}{2}\rho f_w (A\omega)^2$$

(5.44)

So far, only a few experimental studies that dealt with the friction factor in the wave–current boundary layers. It has been determined that, for the laminar flow, the friction factor depends on the Reynolds number as:

$$f_w = \frac{2}{\sqrt{\frac{A^2\omega}{\nu}}}$$

(5.45)

The experimentally determined friction factors based on the present data and equation 5.44 are shown in figure 5.50. The friction factor has a weak dependence on Re_o than in the case of laminar flow, for larger values of Re_o. Similar results were also obtained for wave boundary layers (see Justesen (1988), Nielsen (1992)); in these

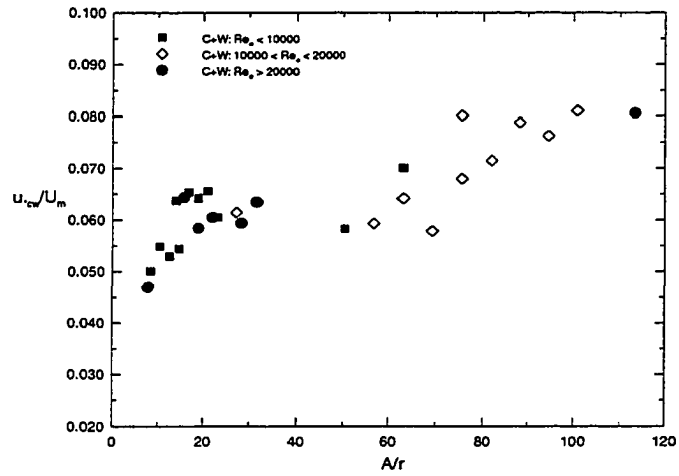FIGURE 5.48. The friction velocity as a function of relative roughness for different experiments.
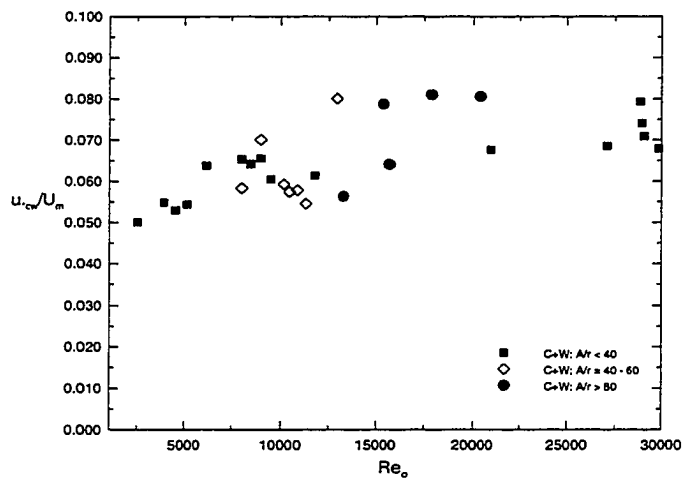
FIGURE 5.49. The friction velocity as a function of the Reynolds number of oscillations for different experiments.

Friction·factor for the wave-current experiments
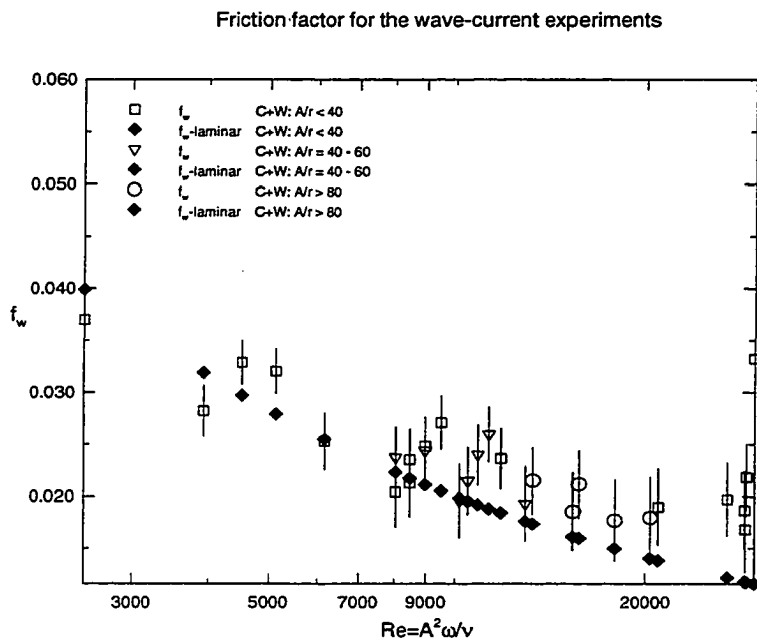
FIGURE 5.50. The friction factor as a function of the Reynolds number of oscillations.
Solid symbols represent a friction factor for the laminar flow.

cases it has been argued that the friction factor is the function of Reynolds number of oscillations Re_o and the relative roughness (r/A). However, for wave–current boundary layers, an additional factor signifying the ratio of the mean current and amplitude of the oscillatory velocity, comes into play:

$$f_w = F(\frac{A^2\omega}{\nu}, \frac{r}{A}, \frac{U_m}{A\omega})$$ (5.46)

As shown in figure 5.51, the friction factor increases linearly with the ratio of mean and amplitude velocity as:

$$f_w = 0.0286(\frac{U_m}{A\omega}) - 0.003$$ (5.47)

Arnskov *et al.* (1993) attempted to measure the friction factor as a function of the ratio of mean and friction velocity. Their data were very scattered and it was not possible to draw any conclusions. The results of the present experiments plotted according to their values, are shown in figure 5.52. It can be clearly seen that the friction factor increases with the ratio of the mean and friction velocity (for $U_m/u_{*cw} > 15$). However, it is more convenient to use outer flow parameters, especially when the results are compared with previous experiments.

The friction factor was also determined as a function of the relative roughness. Nielsen (1992) proposed an empirical relationship between the friction factor and the relative roughness for the wave boundary layer as:

$$f_w = \exp\{5.5(\frac{r}{A})^{0.2} - 6.3\}$$ (5.48)

This friction factor for the wave boundary layers was compared with that of wave–current boundary layers in figure 5.53. Our results for the wave boundary layer friction factor (solid symbols in figure 5.53) agree with 5.48, but the results for wave–current
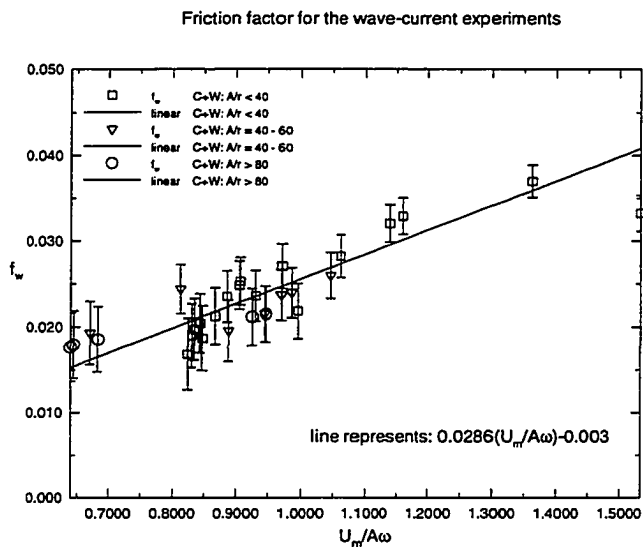
FIGURE 5.51. The friction factor as a function of the ratio of mean and amplitude velocity.
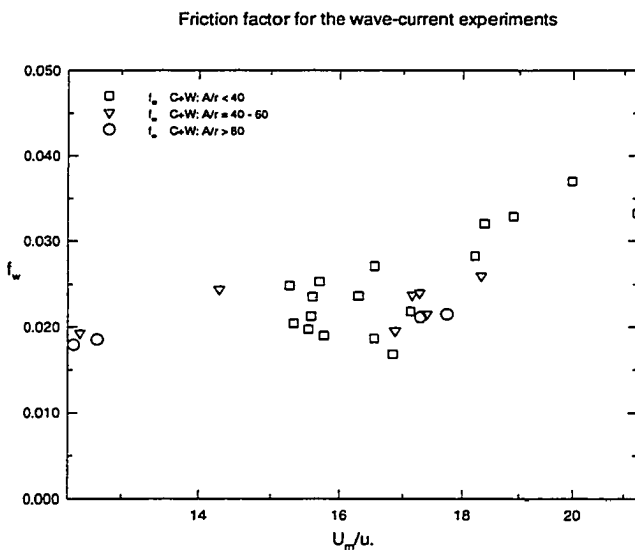
FIGURE 5.52. The friction factor as a function of the ratio of mean and friction velocity.

Friction factor for the wave-current experiments
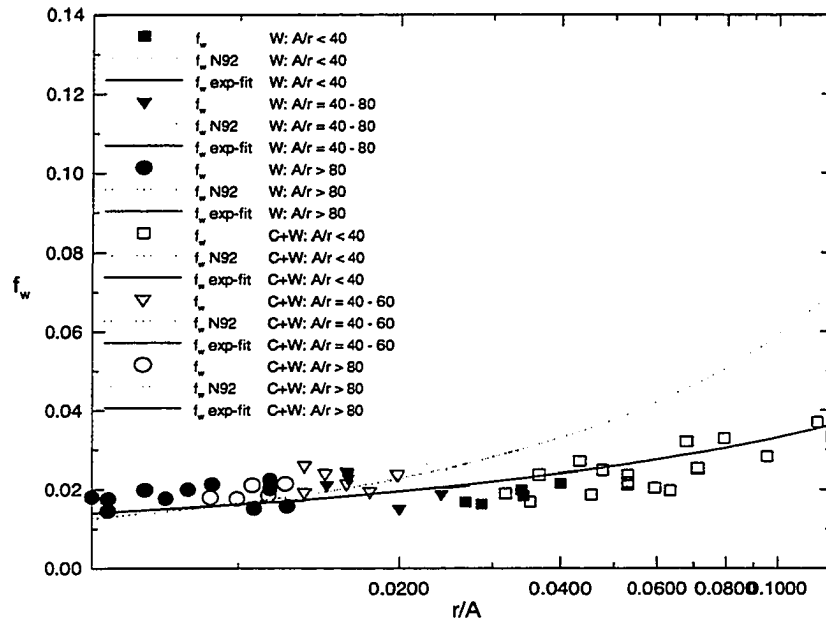
FIGURE 5.53. The friction factor as a function of the relative roughness, comparisons are made with the empirical expression 5.48 of Nielsen (1992) (dashed line) and the experimentally obtained data (symbols) were fitted to 5.49 (solid line).

case were lower for $r/A > 0.02$. It is interesting that the values of the friction factor for the wave–current case are not considerably larger than those of wave boundary layers. The reason appears to be that the major cause of high bottom friction is the short period wave motion, but not the current contribution. Our results show that It has been determined that the results for the wave–current friction factor can be estimated using:

$$f_w = exp\{3.18(\frac{r}{A})^{0.18} - 5.51\} \qquad (5.49)$$

The studies of friction factor of wave–current boundary layers showed that the friction factor is increasing with the ratio of mean and amplitude velocity and relative roughness, while it is decreasing with Reynolds number of oscillations.

5.3.7 Shear stress and eddy viscosity

The concept of eddy viscosity as a link between the dynamics (shear stress) and kinematics (rate of strain) of the flow is rather a complicated entity in wave–current boundary layers. Attempts to model the shear stresses and eddy viscosities have been usually based on the assumption of steady boundary layers (Grant & Madsen (1979), Sleath (1990)) and the possibility of the superposition of the characteristics of the flow.

The recent model of Nielsen (1992) (see Chapter 2) represents an attempt to model flow in wave–current boundary layers using the contributions of different time scales. The velocity was decomposed according to 2.69, and the equations of motion were time and phase–averaged. The mean shear stress (equation 2.71) was obtained by time-averaging the equation of motion, which is a function of x and y coordinates. The dominant contribution to the mean stress comes from the product of horizontal and vertical mean velocities. Velocity gradient, the product of periodic horizontal

and vertical velocity components and the Reynolds stress were averaged over the cycle of oscillation (over 12 phases). The periodic shear stress is time–dependent function $\tilde{\tau}(x, y, t)$ and it was calculated on the basis of the gradient of periodic velocity which was found for each position in the flow field for each phase of oscillation. The dominant terms were found to be the product of mean and periodic velocity components. The phase averaging of the product of the periodic horizontal and vertical velocity components was obtained by averaging at one phase of oscillation along the horizontal direction. The Reynolds stress was phase averaged in the same way.

It is important to note that the two shear stresses are not simply components of the total shear stress in the wave–current boundary layer. The periodic shear stress represents short–scale flow dynamics while mean shear stress signifies large–scale flow dynamics. However, both stresses represent contributions to the vertical flux of horizontal momentum. The model of Nielsen (1992) is the first to consider non–linear interactions between short and large scales motions, identified in the work of Grant & Madsen (1979). One of the major aims of the present work is to test the model of Nielsen (1992) which has not been experimentally verified so far.

The mean shear stress in the two–dimensional window of measurement is shown in figures 5.54 and 5.55 for two different experiments. It is interesting to note that the contours of the mean shear stress are approximately parallel to the horizontal (streamwise) direction in the upper part of the boundary layer dominated by the mean current. In the part of the boundary layer close to the bottom, this horizontal homogeneity is broken and contours tend to concentrate on specific vortex structure in the wave dominated part of the boundary layer.

Periodic shear stresses for different phases of the flow are presented in figures 5.56 and 5.57. The periodic shear stress is not as uniform in horizontal direction as

Shear stress 'felt' by the mean current (Nielsen, 1992)

Exp#9: A=18cm, T=8s, U$_m$=9.33cm/s, I-w-r=0.318-0.318-0.635cm

FIGURE 5.54. The distribution of mean shear stress in the two–dimensional flow field for exp#9.

Shear stress 'felt' by the steady current (Nielsen, 1992)

Exp#28: A=11cm, T=8s, U$_m$=8.39cm, I-w-r=0.476-0.476-0.476cm

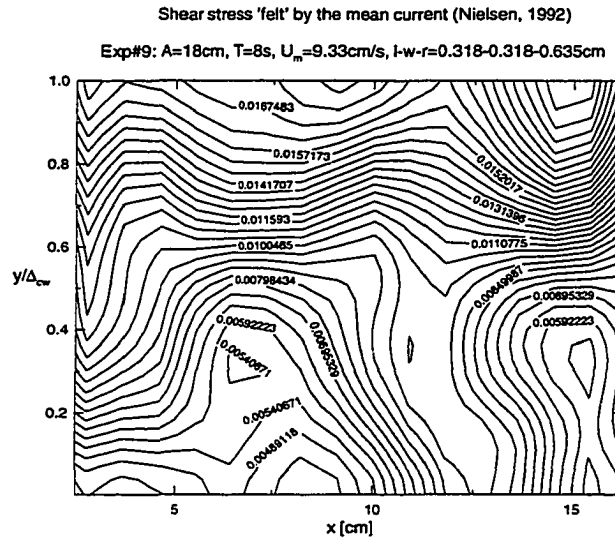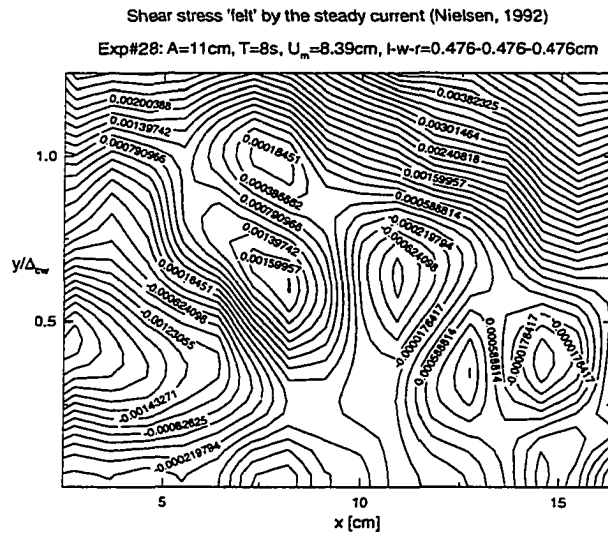FIGURE 5.55. The distribution of mean shear stress in the two–dimensional flow field for exp#9.

FIGURE 5.56. The distribution of periodic shear stress in the two–dimensional flow field for exp#9. (a) $\omega t = 90^o$ and (b) $\omega t = 180^o$.
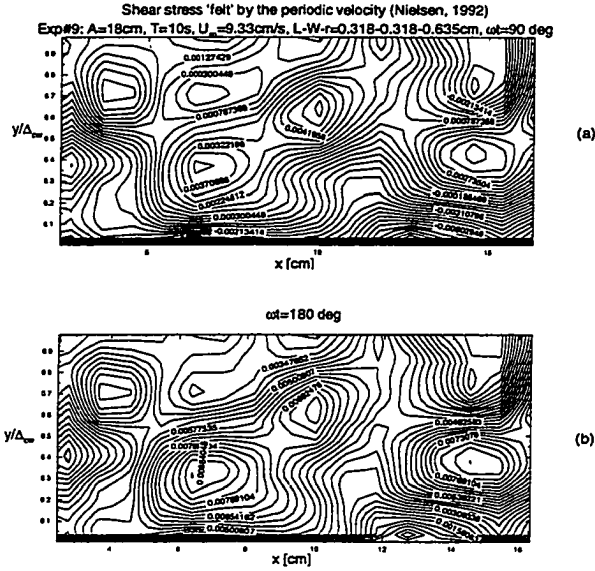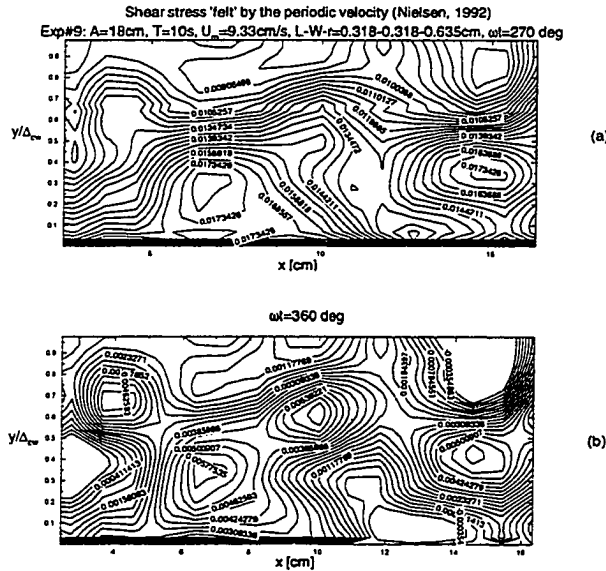

FIGURE 5.57. The distribution of periodic shear stress in the two–dimensional flow field for exp#9. (a) $\omega t = 270^o$ and (b) $\omega t = 360^o$.

the mean shear stress even at greater heights. As it was stated earlier, the periodic shear stress manifests short–scale motions, and one can observe small contour cells representing different vortex structures. The horizontal distance between the captured vortices appears to be on the order of the amplitude.

The eddy viscosity ν_c in model of Nielsen (1992) based on the mean shear stress, represents "the eddy viscosity felt by the steady flow component", while the one based on periodic shear stress ν_w represents "the one felt by the periodic (velocity) component". The expressions for the "mean" and "periodic" eddy viscosity were presented in Chapter 2 (equations 2.73 and 2.74). The eddy viscosity ν_c is a function of coordinates only, while ν_w is a function of coordinates and time. In order to present and simplify comparison between the two, both eddy viscosities are averaged in the horizontal direction and are presented in figures 5.58, 5.59 and 5.60. Eddy viscosity based on the mean and periodic shear stress are compared with the model of Grant & Madsen (1979) presented in equations 2.65 and 2.66. The reason for this comparison is to present how a model based on steady boundary layer concepts (Grant & Madsen (1979)) compares with the Nielsen's concept of mean and periodic stresses. It can be clearly seen that the eddy viscosity based on steady boundary layer concepts is much smaller than the ν_c and ν_w, sometimes an order of magnitude. The eddy viscosity based on the mean current is much larger than that based on the periodic stress in the region close to the bottom. Closer to the top, ν_c increases rapidly, probably due to the fact that the gradient of the mean velocity is very small closer to the top of the boundary layer. On the other hand, the eddy viscosity based on periodic stress takes both positive and negative values, the negative values mostly close to the bottom, perhaps due to the ejection of vortex structures from the top of roughness elements as in the case of wave boundary layers (Sleath (1987)). It seems that ν_w is strictly negative in the first half–cycle ($\omega t = 0 - 180^o$) while it is taking both positive and

FIGURE 5.58. Comparison of eddy viscosities for exp#9. $\omega t =$ (a) 30°, (b) 60°, (c) 90°, (d) 120°.
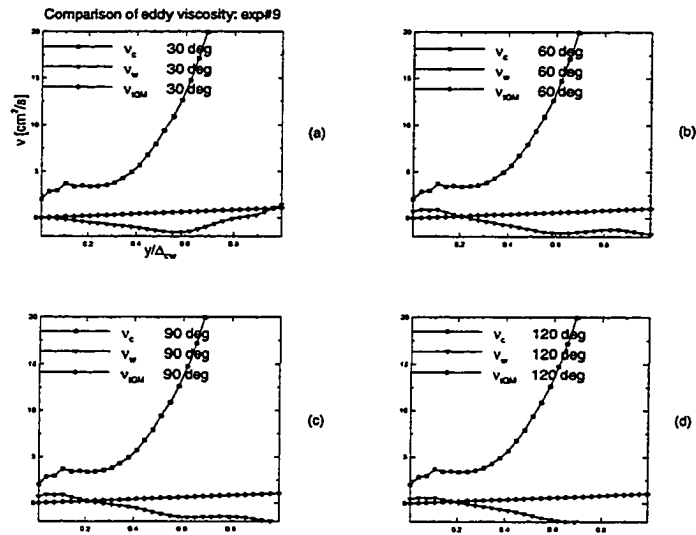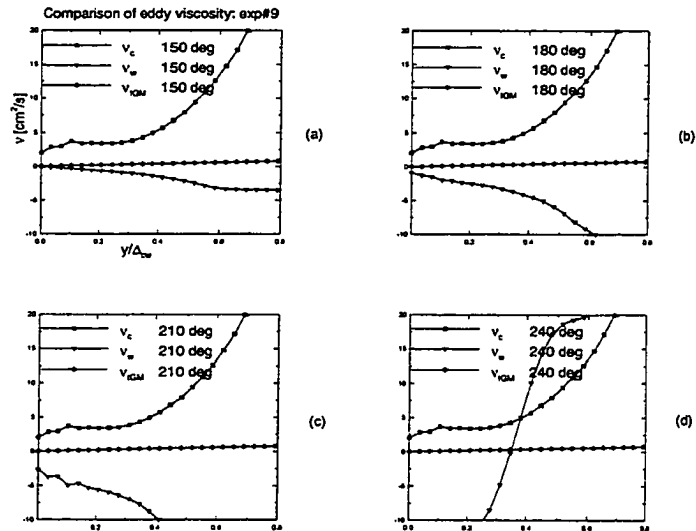

FIGURE 5.59. Comparison of eddy viscosities for exp#9. $\omega t =$ (a) 150°, (b) 180°, (c) 210°, (d) 240°.
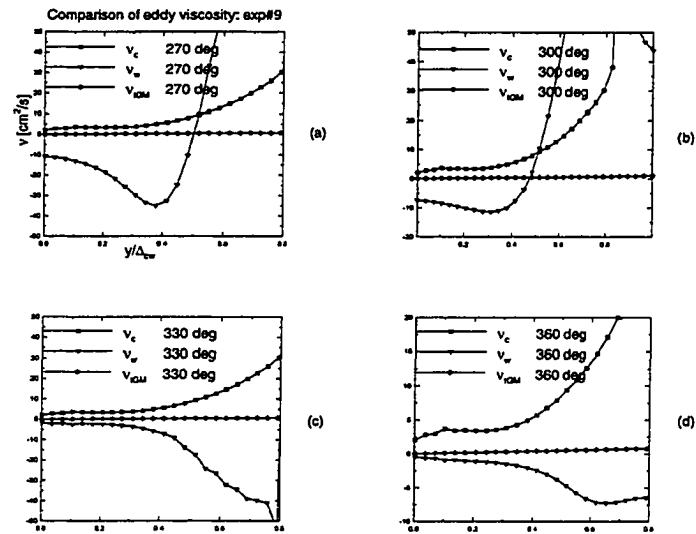
FIGURE 5.60. Comparison of eddy viscosities for exp#9. $\omega t = $ (a) $270°$, (b) $300°$, (c) $330°$, (d) $360°$.
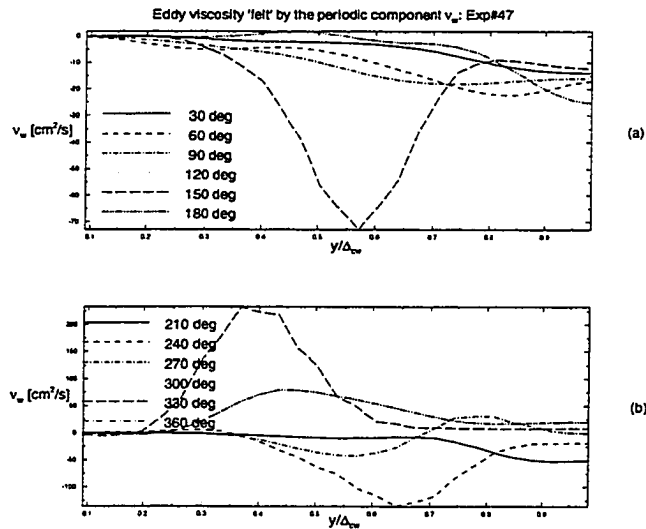
FIGURE 5.61. Experimental eddy viscosity based on the periodic shear stress for exp#47. $\omega t = $ (a) $0 - 180°$, (b) $210 - 360°$.

negative values during $\omega t = 180 - 360°$, see figure 5.61. However, it seems that closer to the bottom, where the changes of the flow field are drastic, eddy viscosity based on periodic flow is strongly negative and changes almost linearly with the distance from the bottom.

The eddy viscosity based on the mean stress are presented for a few experiments in figure 5.62. Since ν_c is the eddy viscosity "felt" by the steady current, it can be related to the concept of eddy viscosity in the steady current boundary layer. However, ν_c is much larger than that given in 2.65 and increases much rapidly with the distance from the bottom. An important observation is that ν_c is increasing linearly with the distance from the bottom in the wave sublayer $y/\delta < 0.2$, and then proceeds to increase at a steeper rate. This can be an useful observation for numerical modeling. Moreover, it was found that ν_c scales reasonably with the product of mean velocity and amplitude of oscillations (see figure 5.62b).

Nielsen (1992) deduced from available data, that ν_c is three to four time greater than ν_w. To verify this postulation, $|\nu_c/\nu_w|$ is presented in figure 5.63 over a whole cycle of oscillations. The results corroborate Nielsen's claim and show that ν_c is 2–6 time larger than ν_w on the average. For most phases, however, this ratio is close to one at the top of the boundary layer. This is somewhat expected as periodic velocities are much smaller at the edges of the boundary layer than at the bottom.

There have been only a very few experiments reported on wave–current boundary layers. Some of the comprehensive studies reported in this context are those of Kemp & Simons (1982) and Kemp & Simons (1983). They obtained the eddy viscosity based on the mean shear stress (ν_c) and observed that ν_c changes linearly in the outer layer, while the data near the bed were rather scattered (suggesting a constant value). In the present experiments, a linear increase of ν_c was also observed in the wave sublayer.
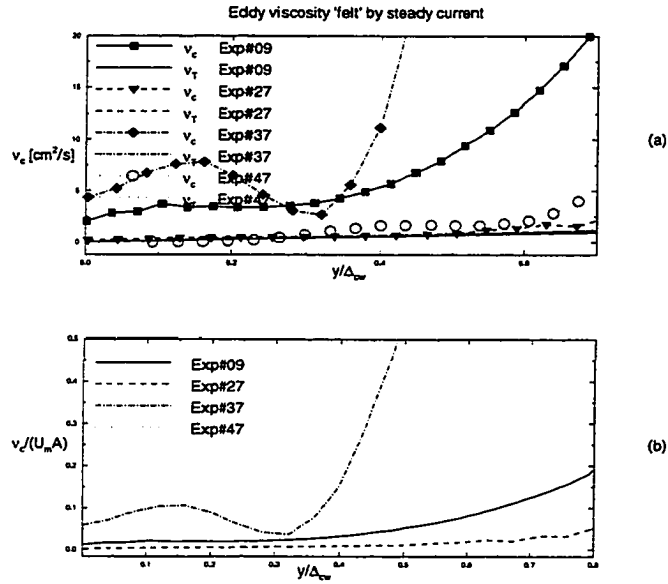
FIGURE 5.62. Comparison of eddy viscosity based on mean shear stress for exp#9, exp#27, exp#37, exp#47. (a) ν_c $[cm^2/s]$ and (b) $\nu_c/(U_m A)$
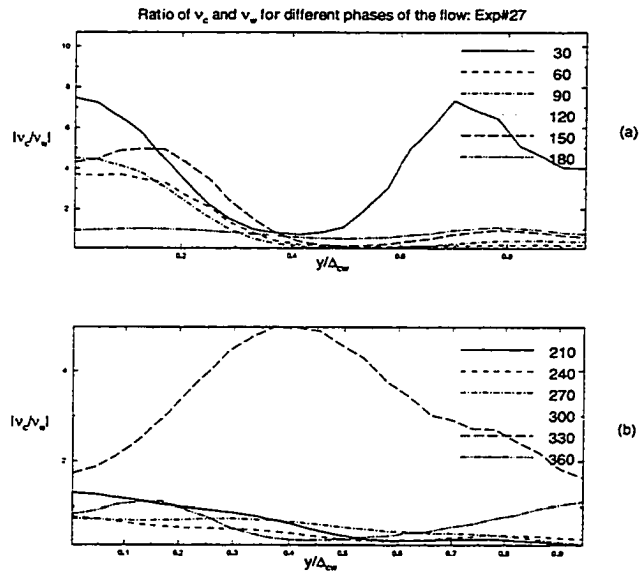
FIGURE 5.63. Comparison of eddy viscosities ν_c and ν_w. $\omega t =$ (a) $30 - 180^o$ and (b) $210 - 360^o$.
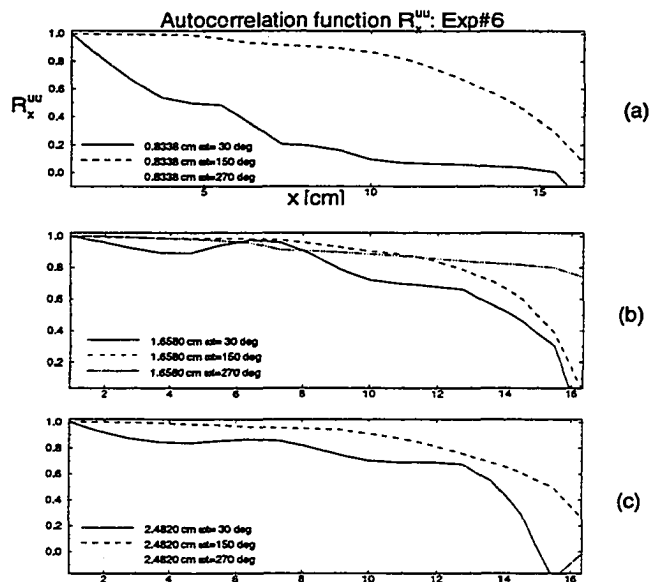
FIGURE 5.64. An example of the autocorrelation functions $R_x{}^{uu}$ for Exp#6 at $\omega t = 30, 150, 270°$. $y =$ (a) 0.83 cm, (b) 1.66 cm, (c) 2.48 cm.
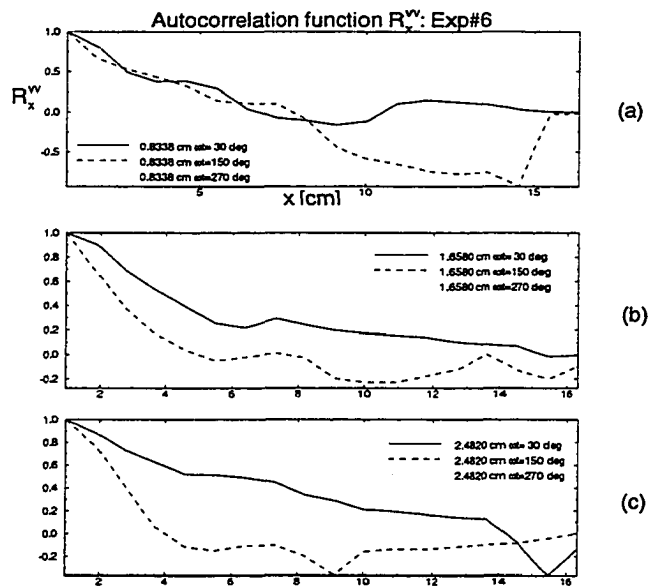
FIGURE 5.65. An example of the autocorrelation functions $R_x{}^{vv}$ for Exp#6. For caption (a)–(c) see figure 5.64.

5.3.8   Integral length–scales

The integral length–scales were evaluated using 5.20 based on velocity measurements taken in a certain phase and at a certain distance from the bottom. An example of the autocorrelation function involving horizontal velocity components is shown in figure 5.64. It is interesting to note that the integral length–scales increase with the distance from the wall. Also, integral length–scale of the vertical velocity components $L_x{}^{vv}$ are significantly smaller than that based on horizontal velocity components $L_x{}^{uu}$ (see figure 5.65).   These observations are not unexpected since the current represents a horizontally homogeneous large scale flow that is conducive to large integral scales $L_x{}^{uu}$. Closer to the bottom, the flow, is influenced by wave forcing that is characterized by short scales $L_x{}^{uu}$.

The variation of the integral length–scales with the phase of oscillation and the distance from the bottom is shown in figures 5.66–5.68.   The integral length–scales have local maxima around $y/\Delta_{cw} \approx 0.25 - 0.3$. This is observed for all phases of the flow, which demands a physical explanation. As discussed previously, the wave sublayer occupies approximately one third of the total thickness of the wave–current boundary layer, and the local maximum of integral length–scales appears to correspond to the top of the wave sublayer. This is the region where the enhanced velocity gradients could be seen near the bottom, due to the mixing induced by the interaction of waves, current and bottom roughness. Thus, the superposition of wave forcing on a steady current produces higher velocities in the immediate vicinity of bottom than in the case of current alone. Therefore, we can expect that the velocities just above the bottom in a wave–current boundary layer are more correlated than in the case of pure wave boundary layer. This explains why the integral length–scales increase with the distance from the wall in the wave sublayer and then decrease or remain approx-
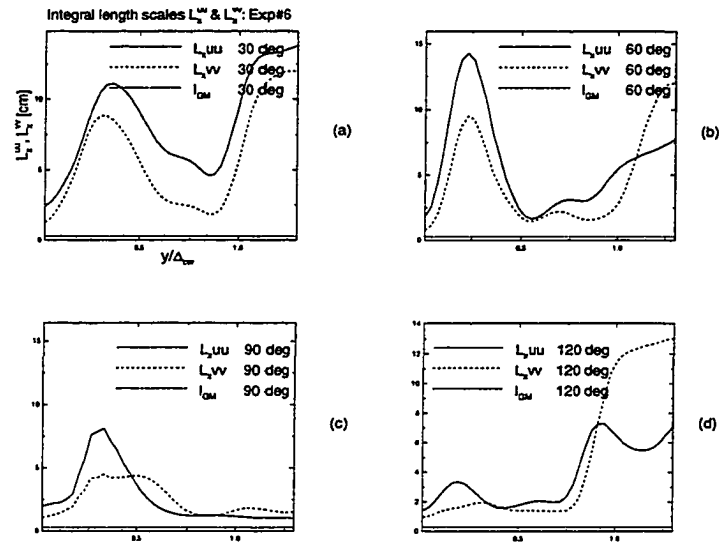
FIGURE 5.66. Integral length–scales $L_x{}^{uu}$ and $L_x{}^{vv}$ for experiment 6. $\omega t =$ (a) 30°, (b) 60°, (c) 90°, (d) 120°.
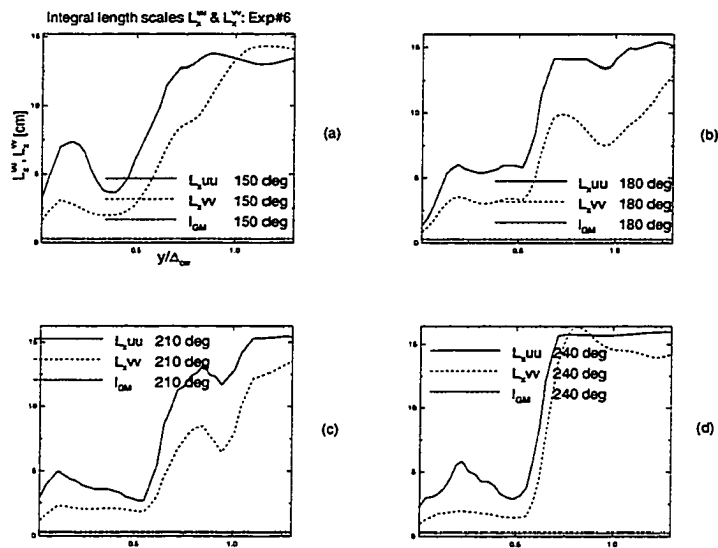
FIGURE 5.67. Integral length–scales $L_x{}^{uu}$ and $L_x{}^{vv}$ for experiment 6. $\omega t =$ (a) 150°, (b) 180°, (c) 210°, (d) 240°.
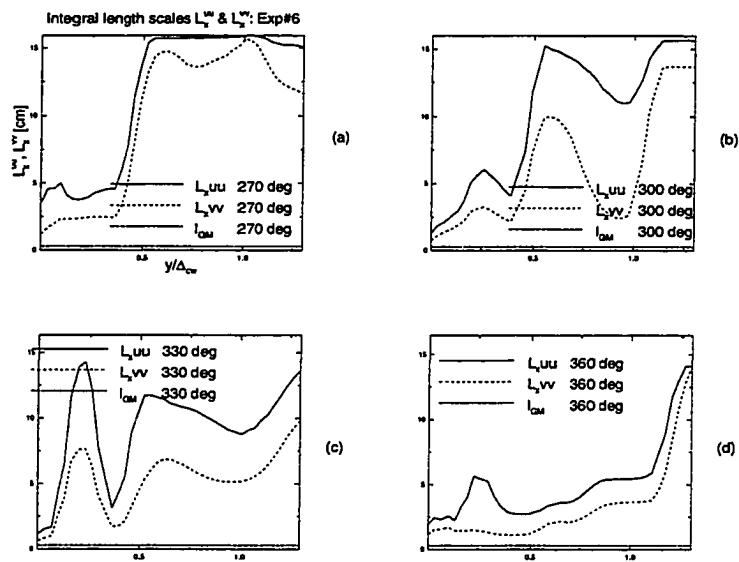
FIGURE 5.68. Integral length–scales $L_x{}^{uu}$ and $L_x{}^{vv}$ for experiment 6. $\omega t = $ (a) $270°$, (b) $300°$, (c) $330°$, (d) $360°$.

imately constant towards the top of the wave–current boundary layer. The decrease of the integral length–scales above the wave sublayer can be explained by recognizing that the steady current experiences an "artificial" or "apparent roughness" pertinent to the wave sublayer, consequently producing smaller velocities at the top of the wave sublayer. In other words, the top of the wave sublayer can be imagined as a rough surface underlying the steady current over which a turbulent boundary layer develops.

The integral length–scales were averaged for all phases of the flow and for $y/\Delta_{cw} = 0-1$ and the results were compared with the length–scales proposed by Grant & Madsen (1979) l_{GM}. The ratio of the integral length–scales to l_{GM} is shown in figure 5.69. The results were segregated to various A/r ranges and it was found that the following expressions are valid:

$$\frac{L_x{}^{uu}}{l_{GM}} = 25.377 + 97.0156e^{-(A/r)/11.2081} \tag{5.50}$$

and,

$$\frac{L_x{}^{vv}}{l_{GM}} = 15.637 + 63.016e^{-(A/r)/11.2081} \tag{5.51}$$

The measured integral scales are much larger than that proposed by Grant & Madsen (1979), especially if A/r is small. The results, therefore, hints to the possibility that the length–scales in the wave–current boundary layers cannot only be represented as a function of radial frequency of oscillations ω, but should take the general form

$$\frac{L_x{}^{uu}}{l_{GM}}, \frac{L_x{}^{vv}}{l_{GM}} = f(\frac{A}{r}, \frac{A^2\omega}{\nu}, \frac{U_m}{A\omega}) \tag{5.52}$$

The general form 5.52 is difficult to determine experimentally, since the large number of experiments is required to cover reasonable parameter ranges. Thus, the ratio
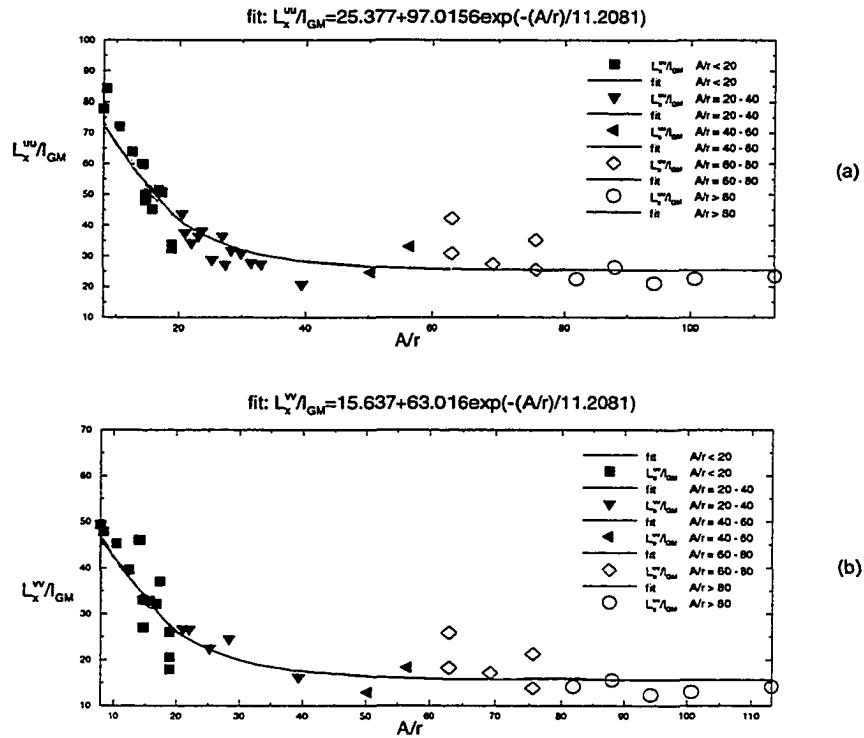
FIGURE 5.69. Integral length–scales (a) L_x^{uu} and (b) L_x^{vv}, compared to the scale of Grant & Madsen (1979).

of the integral length–scales to l_{GM} as a function of $Re_o = A^2\omega/\nu$ is shown in figure 5.70 for different A/r ranges. The ratio L_x^{uu}/l_{GM} was found to depend on the Reynolds number of oscillation as was for the for oscillatory boundary layer flows. The magnitudes of L_x^{uu}/l_{GM} (and L_x^{vv}/l_{GM}) are, however, an order of magnitude higher than the oscillatory boundary layer case. These ratios are decreasing functions of the Reynolds number and level off at $A^2\omega/\nu > 10000$ or so. The change of the ratio of integral length–scale and l_{GM} with respect to $U_m/A\omega$ is shown in figure 5.70b for different ranges of Re_o. It can be seen that the integral length–scales increase very fast as $U_m/A\omega$ increases, especially for large values of Re_o.

Integral length-scales as a function of flow parameters

(a)

(b)
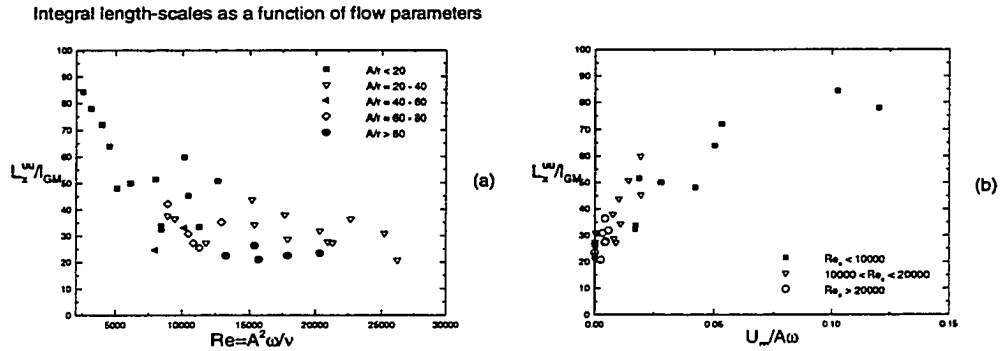
FIGURE 5.70. Integral length–scales $L_x{}^{uu}$ as functions of flow parameters: (a) $Re = A^2\omega/\nu$ and (b) $U_m/A\omega$.

Ratio of integral lengthscales: $L_x{}^{uu}/L_x{}^{vv}$

(a)

(b)
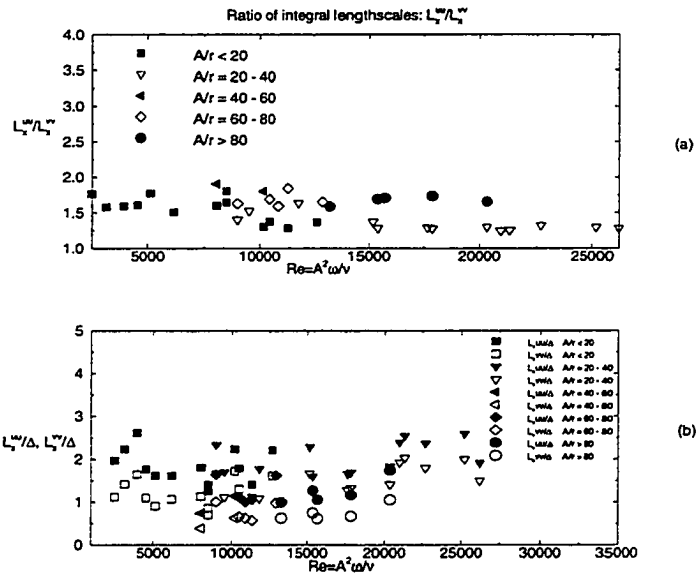
FIGURE 5.71. (a) Ratio of integral length–scales $L_x{}^{uu}/L_x{}^{vv}$. (b) Ratio of integral length–scales and boundary layer thickness.

The ratio of averaged integral length–scales $L_x{}^{uu}/L_x{}^{vv}$ as the function of Reynolds number of oscillation is presented in figure 5.71. It can be seen that this ratio is constant with respect to Reynolds number of oscillations and it is in the range $1.25 - 1.75$ for the experiments presented in this study. It is a common practice to use the integral length–scales as representative of the boundary layer layer thickness, and hence, the ratio of integral length–scale to boundary layer thickness was investigated. Figure 5.71b shows this relationship, which shows that $L_x{}^{uu}/\Delta_{cw} \approx 0.5 - 2.5$, depending on the Reynolds number of oscillations. However, this value slightly increases for $Re_o > 15000$.

CHAPTER 6

ESTIMATION OF EXPERIMENTAL ERRORS

In order to determine the reliability of data, it is necessary to present error estimations of the measurements. To this end, the method of Kline & McClintock (1953), which is based on the uncertainties of the various primary experimental measurements, was used. This method assumes that the uncertainty of each measurement (or measured variable) can be expressed with the same odds, that the measured quantity is a function of several independent variables:

$$R = R(x_1, x_2, ..., x_n) \tag{6.1}$$

and that each variable is measured with certain uncertainties $w_1, w_2, ..., w_n$. The uncertainty of the result w_R can therefore be expressed as:

$$w_R = \{(\frac{\partial R}{\partial x_1}w_1)^2 + (\frac{\partial R}{\partial x_2}w_2)^2 + ... + (\frac{\partial R}{\partial x_n}w_n)^2\}^{1/2} \tag{6.2}$$

In order to apply this analysis to present experiments, it is necessary to identify basic variables measured in each experimental run. These are the amplitude of oscillations A, period of oscillation T, time t and fluid velocity u. The uncertainty of amplitude and period of oscillation were determined during the calibration of the experimental apparatus, as $w_A{}^{max} = 0.044A$ and $w_T{}^{max} = 0.065T$ for the short tank, and $w_A{}^{max} = 0.02A$ and $w_T{}^{max} = 0.014T$ for the long tank.

The time and velocity uncertainties are specified by the software for Particle Tracking which is used to map particle trajectories. The uncertainty of velocity measure-

ments for this particular software was determined by Dalziel (1993) to be:

$$\Delta_u = (\frac{12}{m(m+1)(m+2)})^{1/2}\frac{\Delta_x}{\Delta_t}\frac{h}{480} \quad cms^{-1} \tag{6.3}$$

where m is the number of time separations used for fitting the quadratic function through the neighboring points of the trajectory of a particle, Δ_x is the accuracy of determining the position of particles in pixels and h is the vertical size of the field of view in cm. For the case of present experiments, the number of time separations used for fitting the quadratic function was typically $m = 6$, i. e., the trajectory existed if the software had a track of the particle in 6 successive time steps. The time step used for tracking was always $\Delta_t = 0.033s$, and the typical vertical size of the field of view was $h = 6cm$. The magnification of lenses yielded the size of particles spreaded over 5×5 pixels, so the accuracy in determining the position of particle can be estimated as the radius of particle which is $\Delta_x = 3$ pixels. Incorporating these estimates into 6.3, it is possible to obtain the typical uncertainty of velocity measurements to be $w_u = \Delta_u = 0.214cms^{-1}$. Finally, the uncertainty of time measurements by the particle tracking software can be estimated as $w_t = 0.017s$, which is the half time lapse between the frames. The software is using two half–frames to calculate velocity at every 0.033 s and 0.017s represents the uncertainty of grabbing a particular image at a particular instant of time.

Using the 6.2 and above uncertainties of independent quantities (A, T, t, u), the maximum measurement errors of quantities such as $\overline{u}$ and $\tilde{u}$ can be expressed as:

$$w_{U_m} = \frac{1}{\sqrt{N_m}}w_u \tag{6.4}$$

and

$$w_{\bar{u}} = \frac{1}{\sqrt{N_w}} w_u \tag{6.5}$$

where N_m is the number of data points averaged to obtain mean velocity and N_w is the number of data points averaged to obtain periodic velocity. In the present study $N_m = 120$ (10 cycles with 12 phases) and $N_w = 10$ (10 cycles of oscillations). This leads to $w_{U_m} = 0.0195 cm/s$ and $w_{\bar{u}} = 0.0957 cm/s$. The uncertainty of velocity fluctuation is also found to be $w_{u'} = 0.235 cm/s$.

Using similar analyses, the experimental errors of salient variables estimated using the technique of Kline & McClintock (1953) are presented in table 6.1. To determine the uncertainties of the shear stress w_τ and eddy viscosities ν_c and ν_w, the following assumptions on typical values were used: $\bar{u} \approx 10 cm/s$, $\tilde{u} \approx 5 cm/s$ and the velocity gradient is the same as the average gradient of instantaneous velocity at the bottom. Also, it can be seen from table 6.1 that the long tank with an improved driving mechanism for the plate motion yielded significantly lower errors for the amplitude and period of oscillations, which corresponded to lower errors of determining the Reynolds number of oscillations. Errors of the three most used experiments are shown in table 6.2 for comparison.

Error analysis showed that the relative errors of measurements for different variables are low (under 5%), except for the case of shear stress that is plagued by the cumulative errors of instantaneous, mean, periodic and fluctuation velocities. Shear stress, according to definitions of Nielsen (1992), is a variable that depends on velocity components and the size of samples that are suppose to be averaged. The only way to improve these measurements is to have a finer grid within the tracking window, which is limited by the capabilities of the Particle Tracking software. In

variable	wave	wave+current
u	0.214 cm/s	0.214 cm/s
$\bar{u}$	N/A	0.0195 cm/s
$\tilde{u}$	0.0479 cm/s	0.0957 cm/s
u'	0.219 cm/s	0.235 cm/s
u_{rms}	0.219 cm/s	0.235 cm/s
K_o	$2w_{u'}K_o$	$2w_{u'}K_o$
Δ	0.2 cm	0.18 cm
$Re_o = A^2\omega/\nu$	$0.1094Re$	$0.0424Re$
$Re_m = U_mW_t/\nu$	N/A	$0.0195/U_mRe$
$\bar{\tau}$	N/A	4.25e-05 kg/cms^2
$\tilde{\tau}$	9.1e-5 kg/cms^2	1.1e-5 kg/cms^2
ν_c	N/A	0.0068 cm^2/s
ν_w	0.0494 cm^2/s	0.0344 cm^2/s
L_x^{uu}	0.22 cm	0.18 cm

TABLE 6.1. Estimation of uncertainties for different variables for the case of oscillatory (wave) and wave–current experiments.

relative error [%]	Exp.#6	Exp.#9	Exp.#20
w_A/A	0.83	1.67	1.84
w_T/T	1.33	0.85	0.98
w_{U_m}/U_m	0.208	0.209	0.226
w_{Re_o}/Re_o	2.14	3.44	3.81
w_{Re_m}/Re_m	0.208	0.209	0.225
w_Δ/δ	3.06	3.27	4.72
$w_{\tau_b}/\overline{\tau_b}$	14.4	13.9	11.5
$w_{L_x^{uu}}/L_x^{uu}$	1.95	1.61	1.64
$w_{L_x^{vv}}/L_x^{vv}$	2.50	2.09	2.13

TABLE 6.2. The relative experimental errors for the wave–current experiments #6, #9 and #20.

all, the comprehensive analysis of errors described above clearly illustrate that the measurements reported in Chapter 5 are reliable to make inferences on wave and wave–current boundary layers.

CHAPTER 7

CONCLUSIONS

7.1 STEADY BOUNDARY LAYERS

Measurements in a steady current were performed mainly to establish confidence on the experimental techniques and apparatuses. The main conclusions of these studies are:

- The mean velocity profiles exhibited the classical logarithmic behaviour of the form $U_m/u_* = 1/\kappa ln(30y/k_s)$, with the constants κ and B being approximately similar to the canonical values, 0.4 and 5, respectively. The thickness of the overlap layer matches the data of previous studies.

- The mean velocity profiles at the different streamwise positions confirmed that the flow is fully developed in the measurement section.

- The turbulent flow outside of the boundary layer has turbulence intensities on the order $5 - 10\% U_m$.

- Turbulence intensity and shear stress have peaks in the vicinity of the top of the overlap layer.

- The eddy viscosity varies linearly with the distance from the wall in the overlap layer, but the slope was found to depend on the Reynolds number and does not match theoretical prediction of κu_*.

7.2 WAVE BOUNDARY LAYERS

The nature of oscillatory boundary layer over a rough surface was experimentally investigated in this research. A rough plate was oscillated sinusoidally according to $U_p = U_o sin(\omega t)$ under a layer of otherwise still water, and a two–dimensional section of the velocity field $u_i{}^L(x, y, t)$ relative to a laboratory coordinate system was monitored using Particle Tracking Velocimetry (PTV) and Laser–Induced Fluorescence (LIF). The results were interpreted in terms of the velocity field of an oscillating boundary layer over a stationary plate using the transformation $u = u_i{}^L(y, t) - \delta_{i1}U_o sin(\omega t)$. The main conclusions are:

- Detailed flow visualization using LIF technique revealed that the boundary layer contains dipole–like vortex structures formed due to flow separation at roughness elements. These structures propel away from the wall, exchanging momentum between inner and outer layers of OBLs. The boundary layer extends to a distance determined by the travel distance of dipole–like structure.

- The thickness of the WBL Δ_w is given by $\Delta_w/r = 8.2 \times 10^{-4}(A/r)^{0.1}Re^{1.02} - 4.26$. It is surmised argued that the disparities among previous Δ_w measurements, as well as between the previous and present work, may be due to the neglect of Re effects. Based on scaling arguments, an expression is proposed to predict Δ_w.

- The very nature of the dipole–like vortex formation causes OBLs to retain some memory with regard to initial conditions. In a given cycle, the first separated vortex tends to have an impact on the second, causing the vortex structure to propagate at an angle (rather than perpendicular) to the wall.

- The measurements of turbulence in the OBL indicate that the turbulent intensities are highest when the background velocity is at near its peak. Because of

the strong interaction between vortices generated during the first and second halves of a cycle, the turbulent intensity distributions in the two halves differ significantly.

- The generation of vortices near the wall and their transport to the outer layers of OBL are evident from the local increase of Reynolds and total stresses at certain phases of an oscillatory cycle.

- Turbulent length–scales were evaluated at different phases based on the measured auto–correlation functions. The comparison of measurements with commonly used parametrization revealed that the measurements are best described by the model of Grant & Madsen (1979) when $Re > 18,000$; notwithstanding, there are some disparities between the predictions and measurements at certain phases.

- Evaluation of eddy diffusivities based on the Reynolds stress ν_i and the total stress ν_T showed that they are highly time (phase) and space dependent and do not compare favorably with the model of Trowbridge & Madsen (1984). More refined models for ν_T based on the rich variety of flow structures present in OBLs are called for to improve the predictability coastal boundary layers.

7.3 WAVE–CURRENT BOUNDARY LAYERS

Wave–current boundary layers were studied in a long tank by using Particle Tracking Velocimetry that enabled whole-field velocity measurements in a two–dimensional window of the flow field. As in the case of WBL, the velocity field was transformed to a one that corresponds to coastal boundary layer. The intention was to correlate visual observations based on Laser Induced Fluorescence to physical concepts and quantitative measurements of turbulence. A wide range of experimental parameters

was used and a robust set of measurements was obtained. The major conclusions can be summarized as follows:

- The flow visualization showed the vortex formation only toward the end of the half–cycle, whence the orbital velocities of waves and mean current have opposite directions. Enhanced shear between the opposing current and the wall layer in the immediate vicinity of the bottom is the cause of vortex formation. The ejection of the vortices away from the bottom occurs in a direction inclined to the vertical axis due to the advection of vortices by the current.

- The flow visualization and boundary layer thickness measurements provide some qualitative support for the postulation of Grant & Madsen (1979) who raised the possibility of a wave sublayer dominated by the wave orbital motions and a layer dominated by currents. Thus, the thickness of the wave sublayer δ_w, as well as the total thickness of WCBL Δ_{cw} was determined.

- For the (wide) range of parameters studied, the total boundary layer thickness is 1.2–5.5 times larger than the thickness of the wave sublayer. This agreed fairly well with the thickness estimate $C\kappa u_{*cw}/\omega$ with a constant $C \approx 4$. Grant & Madsen (1979) proposed $C = 2 - 4$.

- For given Re_m, Re_o and r/d, the three boundary–layer thicknesses corresponding to steady Δ_c, wave Δ_w and wave–current Δ_{cw} flow show the following: (i) addition of waves to a steady current decreases the thickness of boundary layer of the current ($\Delta_{cw} < \Delta_c$), (ii) addition of a current to waves increases the thickness of the boundary layer ($\Delta_c w > \Delta_w$), and (iii) the thickness of the pure wave boundary layer is larger than the thickness of the wave sublayer ($\Delta_w > \delta_w$) if $r/d \geq 1$.

- Fitting of the mean velocity profile to the logarithmic profile of Grant & Madsen (1979) show that the constant κ for $y < \delta_w$ takes values smaller than the classical $\kappa = 0.41$, suggesting steeper changes of velocity than in the case of a steady current alone. The apparent roughness was found to be 10–100 times larger than the equivalent Nikuradse roughness, based on the same steady current velocity and bottom roughness. The apparent roughness was found to be the function of $A\omega/u_{*cw}$ and A/r.

- Velocity fluctuations and the turbulent kinetic energy (TKE) have maximum values at the phase corresponding to the ejections of vortices and it occurs just above the roughness elements. The average values of the horizontal and vertical velocity fluctuations just above the bottom are 15–20%U_o and 10%U_o respectively (based on observations of all listed experiments). Velocity fluctuations are decaying with the distance from the bottom.

- The ejection of vortices causes non–uniformity of turbulent kinetic energy values in the horizontal direction. For phases where the velocity is well established, the TKE levels are uniform in the most of the 2–D domain.

- The bottom shear stress and friction velocity are nearly uniform in the streamwise (horizontal) direction, and averaging of results in horizontal direction is justified for this case.

- The change of friction velocity during a cycle of oscillation showed the same trend for all experiments, in that it does not change as a harmonic function. The dominant parameter that determines the friction velocity is the ratio of the mean velocity and the amplitude of wave velocity.

- The friction factor for wave boundary layers follows previously published empirical results based on relative roughness of the bed. However, there are only a few experimental studies available on wave–current boundary layers with which the present results can be compared. The present studies show that the friction factor increases slowly with the relative roughness and it is slightly larger in the WCBL compared to the WBL. The latter suggests that the main cause of increased bottom shear stress is the periodically imposed motion. The friction factor increases linearly with the ratio of the mean to amplitude of wave velocity.

- The mean shear stress related to the steady current within the boundary layer (based on the model of Nielsen (1992) shows horizontal uniformity, except near the bottom. The mean shear stress near the bottom changes only a little, although it is subject to dynamical processes due to the interaction of flow with roughness elements.

- The periodic shear stress changes rapidly from one phase of oscillations to another signifying the formation and propagation of vortices ejected from roughness elements.

- In the wave boundary layer, the eddy viscosity based on the mean shear stress ν_c is increasing linearly with the distance from the bottom. In the layer loft the wave sublayer ν_c is increasing much faster (nonlinearly). The observed values of ν_c are mostly positive.

- The eddy viscosity based on the periodic shear stress ν_w takes both positive and negative values. In the wave sublayer ν_w is almost always negative and its variation with the distance from the bottom is approximately linear.

- The eddy viscosity based on the periodic shear stress ν_w is 2–6 times smaller than the eddy viscosity based on the mean shear stress ν_c, with the exception that $\nu_w/\nu_c \approx 1$ at the top of the boundary layer.

- The horizontal integral length–scales based on autocorrelation functions at various phases are much larger for wave–current boundary layers than for oscillatory (wave) boundary layers. Increased spatial correlations generated by the steady current accounts for this enhancement.

- Integral length–scales showed a local maximum at $y/\Delta_{cw} \approx 0.3$, corresponds to the top of the wave sublayer. The integral length–scales increase rapidly within the wave sublayer as a consequence of the increase of local velocity near the bed due to vigorous mixing by the wave motions. The integral length–scales decrease or even remain approximately constant above the wave sublayer due to the fact that the steady current experiences an " apparent roughness" due to the wave sublayer. The data, in general, support the notion of Grant & Madsen (1979) that the wave–current boundary layer can be divided into a layer dominated by wave action (wave sublayer) and a layer dominated by the mean current.

- The measured integral length–scales $L_x{}^{uu}$ and $L_x{}^{vv}$ are much larger than that proposed by Grant & Madsen (1979) l_{GM} for wave–current boundary layer. Their scale based on the friction velocity and the radial frequency of oscillation is not satisfactory enough for this type of complex flows that depend on several governing flow parameters. Owing to the difficulty of finding an exact correlation, only a crude parameter dependence of the integral length–scales was identified. The ratios $L_x{}^{uu}/l_{GM}$ and $L_x{}^{vv}/l_{GM}$ decreases with A/r, but for the small relative bottom roughness this ratio is approximately 15–25. Also,

$L_x{}^{uu}/l_{GM}$ decreases with the Reynolds number of oscillations and levels off at $A^2\omega/\nu > 10000$. The ratio $L_x{}^{uu}/L_x{}^{vv}$ takes values 1.25–1.75 and the integral length–scales are 0.5–2.5 times larger than the thickness of the wave–current boundary layer.

7.4 RECOMMENDATIONS FOR FUTURE WORK

There are numerous theoretical and numerical studies on the wave boundary layer, but they have not considered specific mechanisms (e.g. vortex dynamics) that are operative at various phases and how such mechanisms are related to overall dynamics of the flow. All numerical studies failed to include physics related to such mechanisms into the modeling efforts. The main reason for this gap is the lack of information on the physics of flow structures that occur during various parts of the cycle. The future wave boundary layer studies should pay close attention to such features, if possible using three–dimensional flow diagnostics. For such studies, it is insufficient to use one point LDV measurements, as was done often in the past. Information so obtained can be used to improve numerical models by using time–varying eddy viscosities based on accurate physics.

Only a few experimental investigations have been reported on wave–current boundary layers, and any new detailed experiments will be welcome to this area of research. The present research have demonstrated that the concepts of Grant & Madsen (1979) for wave–current boundary layers have strong physical foundation, yet their formulation suffers from some oversimplification. Measurements of turbulent characteristics of the flow covering a wide range of parameters, therefore, are required to carefully detect physical processes responsible for changes of eddy viscosities. It appears that the model of Nielsen (1992) gives a good start for the determination of time–dependent

eddy viscosity, but, more research is needed to assimilate such approaches to yield accurate predictability of coastal oceans.

REFERENCES

ARNSKOV, M. M., FREDSØE, J. & SUMER, B. M. 1993 Bed shear stress measurements over a smooth bed in three-dimensional wave–current motion. *Coast. Engng.* **20**, 277–316.

ASANO, T., GODO, H. & IWAGAKI, Y. 1988 Application of low-reynolds number turbulence model to oscillating bottom boundary layers. *Coastal Engng. Japan* pp. 1–9.

BAGNOLD, R. A. 1946 Motion of waves in shallow water: Interaction of waves and sand bottoms. *Proc. Roy. Soc. Lond.* pp. 1–15.

BREVIK, I. 1981 Oscillatory rough turbulent boundary layers. *J. Waterway, Port, Coastal and Ocean Div.* **107**, 175–188.

BREVIK, I. & AAS, B. 1980 Flume experiment on waves and currents. i. rippled bed. *Coast. Engng.* **3**, 149–177.

BRØRS, B. & EIDSVIK, K. J. 1994 Oscillatory boundary layer flows modelled with dynamic reynolds stress turbulence closure. *Cont. Shelf Res.* **14**, 1455–1475.

CELIK, I. & RODI, W. 1985 Calculation of wave–induced turbulent flows in estuaries. *Ocean Engng.* pp. 531–542.

CHOWDHURY, S. A., SATO, M. & UENO, A. 1997 Numerical model of the turbulent wave boundary layer induced by finite amplitude water waves. *Appl. Ocean Res.* **19**, 201–209.

CLAUSER, F. H. 1956 The turbulent boundary layer. *Adv. in Appl. Mech.* **4**.

DALZIEL, S. B. 1992 Decay of rotating turbulence: some particle tracking experiments. *Appl. Sci. Res.* **49**, 217–244.

DALZIEL, S. B. 1993 *DigImage: Image Processing for Fluid Dynamics.* DL Research Partners. United Kingdom.

DAVIES, A. G. 1986 A model of oscillatory rough turbulent boundary layer flow. *Estuarine Coastal Shelf Science* **23**, 353–374.

DRAYTON, M. J. 1993 Eulerian and Lagrangian studies of inhomogeneous turbulence generated by an oscillating grid. PhD thesis, Cambridge University DAMTP.

DU TOIT, C. G. & SLEATH, J. F. A. 1981 Velocity measurements close to rippled beds in oscillatory flow. *J. Fluid Mech.* **112**, 71–96.

EARNSHAW, H. C. 1996 A study of flow over a rippled bed using Particle Image Velocimetry. PhD thesis, The University of Edinburgh.

EVDOSHENKO, M. A. & LOZOVATSKI, I. D. 1994 Time-space variability of the near bottom nepheloid layer at the west Sahara continental slope and shelf. *Oceans 94: Proc. of Oceans Engng. for Today's Tech. and Tomorrow's Preservation, Conf. of EEEA, Brest, France* **1**, 502–505.

FREDSØE, J. 1984 Turbulent boundary layer in wave-current motion. *J. Hydraulic Res.* **110**, 1103–1120.

FREDSŒ, J. & DEIGAARD, R. 1992 *Mechanics of coastal sediment transport.* World Scientific.

GEORGE, C. B. & SLEATH, J. F. A. 1979 Measurements of combined oscillatory and steady flow over a rough bed. *J. Hydraulic Res.* **17**, 303–313.

GRANT, W. D. & MADSEN, O. S. 1979 Combined wave and current interaction with a rough bottom. *J. Geophys. Res.* **84**, 1797–1808.

GRANT, W. D. & MADSEN, O. S. 1986 The continental shelf bottom boundary layer. *Ann. Rev. Fluid Mech.* **18**, 265–305.

GRASS, A. J. 1971 Structural features of turbulent flow over smooth and rough boundaries. *J. of Fluid Mech.* **50**, 233–255.

HINO, M., KASHIWAYANAGI, M., NAKAYAMA, A. & HARA, T. 1983 Experiments on the turbulence statistics and the structure of reciprocating oscillatory flow. *J. Fluid Mech.* **131**, 363–400.

HORIKAWA, K. & WATANABE, A. 1968 Laboratory study on oscillatory boundary layer flow. *Coastal Engng. Conf. Japan* **11**, 13–28.

HUSSAIN, A. K. & REYNOLDS, W. C. 1970 The mechanics of an organized wave in turbulent shear flow. *J. Fluid Mech.* **41**, 241–258.

HUSSAIN, A. K. & REYNOLDS, W. C. 1975 Measurements in fully developed turbulent channel flow. *Fluids Eng. Division of ASME* pp. 568–580.

JENSEN, B. L., SUMER, B. M. & FREDSØE, J. 1989 Turbulent oscillatory boundary layers at high Reynolds numbers. *J. Fluid Mech.* **206**, 265–297.

JONSSON, I. G. 1966 Wave boundary layers and friction factors. *Proc. 10th Int. Conf. on Coastal Engng.* pp. 127–148.

JONSSON, I. G. 1980 A new approach to oscillatory rough turbulent boundary layers. *Ocean Engng.* **7**, 109–152.

JONSSON, I. G. & CARLSEN, N. A. 1976 Experimental and theoretical investigations in an oscillatory turbulent boundary layer. *J. Hydraulic Res.* **14**, 45–60.

JUSTESEN, P. 1988 Prediction of turbulent oscillatory flow over rough beds. *Coastal Engng.* **12**, 257–284.

JUSTESEN, P. 1991 A note on turbulence calculations in the wave boundary layer. *J. Hydraulic Res.* **29**, 699–711.

KAJIURA, K. 1968 A model of the bottom boundary layer in water waves. *Bull. of the Earthquake Res. Inst.* **46**, 75–123.

KALKANIS, G. 1964 Transportation of bed material due to wave action. *US Army CERC Technical Memo* .

KÁRMÁN, T. V. 1930 Mechanische ahnlichkeit und turbulenz. *Math.-Phys.* **58**.

KEMP, P. H. & SIMONS, R. R. 1982 The interaction between waves and a turbulent current: waves propagating with the current. *J. Fluid Mech.* **116**, 227–250.

KEMP, P. H. & SIMONS, R. R. 1983 The interaction between waves and a turbulent current: waves propagating against the current. *J. Fluid Mech.* **130**, 73–89.

KIM, H. T., KLINE, S. J. & REYNOLDS, W. C. 1971 The production of turbulence near a smooth in a turbulent boundary layer. *J. of Fluid Mech.* **50**, 133–160.

KLINE, S. J. & MCCLINTOCK, F. A. 1953 Describing uncertainties in single–sample experiments. *Mech. Engng.* **3**.

KNOBLOCH, E. & PIERCE, R. D. 1998 On mean flows associated with traveling water waves. *Fluid Dynamics Res.* **22**, 61–71.

KONTAR, E. A. & SOKOV, A. V. 1997 On the benthic boundary layer's dynamics. *J. of Marine Systems* **11**, 369–385.

LAMBRAKOS, K. F., MYRHAUG, D. & SLAATTELID, O. H. 1988 Seabed current boundary layers in water–plus–current flow conditions. *J. Waterway, Port, Coastal and Ocean Engng.* **114**, 161–174.

LANDWEBER, L. 1960 Reanalysis of boundary layer data on a flat plate. *9th Int. Towing Tank Conf.* .

LEUTHEUSSER, H. J. 1963 Turbulent flow in rectangular ducts. *J. Hydraulics Div.* pp. 1–19.

LUNDGREN, H. & SOERENSEN, T. 1956 A pulsating water tunnel. *Proc. 6th Int. Conf. Coast. Engng.* .

MADSEN, O. S. 1994 Spectral wave–current bottom boundary layer flows. *21th Int. Conf. on Coastal Engng.* pp. 384–398.

MADSEN, O. S., CHISHOLM, T. A. & WRIGHT, L. D. 1994 Suspended sediment transport in inner shelf waters during extreme storms. *Proc. 24th Int. Conf. on Coastal Engng. Res.* .

MADSEN, O. S. & ROSENGAUS, M. M. 1988 Spectral wave attenuation by bottom friction: theory. *21st Coastal Engng. Conf.* pp. 492–504.

MADSEN, O. S. & WIKRAMANAYAKE, P. N. 1991 Simple models for turbulent wave-current bottom boundary layer flow. *Tech. Rep. US Army Corps of Engineers, Report DRP–91–1* pp. 1–150.

MADSEN, O. S., WRIGHT, L. D., BOON, J. D. & CHISHOLM, T. A. 1993 Wind stress, bed roughness and sediment suspension on the inner shelf during an extreme storm event. *Continetal Shelf Res.* **13**, 1303–1324.

MALARKEY, J. & DAVIES, A. G. 1998 Modeling wave-current interactions in rough turbulent bottom boundary layers. *Ocean Engng.* **25**, 119–141.

MILLIKAN, C. B. 1939 A critical discussion of turbulent flow in channels and circular tubes. *Proc. 5th Int. Conf. on Appl. Mechanics* .

MYRHAUG, D. 1982 On a theoretical model of rough turbulent wave boundary layers. *Ocean Engng.* **9**, 547–565.

MYRHAUG, D., SLAATTELID, O. H., SOULSBY, R. L. & LAMBRAKOS, K. F. 1995 Measurements and analysis of flow velocity and sediment concentration at the seabed. *Appl. Mech. Rev.* **48**, 570–587.

NIELSEN, P. 1984 On the motion of suspended sand particle. *J. Geophys. Res.* **89**, 616–626.

NIELSEN, P. 1992 *Coastal bottom boundary layers and sediment transport.* World Scientific.

PERRY, A. E., LIM, K. L. & HENBEST, S. M. 1987 An experimental study of the turbulence structure in smooth- and rough-wall boundary layers. *J. of Fluid Mech.* **177**, 437–466.

RENIERS, A., BATTJES, J. A., FALQUÉS, A. & HUNTLEY, D. A. 1997 A laboratory study on the shear instability of longshore currents. *J. of Geophys. Res.* **102**, 8597–8609.

SAJJADI, S. G. & WAYWELL, M. N. 1997 Application of roughness-dependent boundary conditions to turbulent oscillatory flows. *Int. J. Heat and Fluid Flow* **18**, 368–375.

SAVIOLI, J. & JUSTESEN, P. 1997 Sediment in oscillatory flows over a plane bed. *J. Hydraulic Res.* **35**, 177–190.

SIGNELL, R. P. & LIST, J. H. 1997 Effect of wave–enhanced bottom friction on storm–driven circulation in massachusetts bay. *J. of Waterway, Port, Coastal and Ocean Engng.* pp. 233–239.

SLAATTELID, O. H., MYRHAUG, D. & LAMBRAKOS, K. F. 1990 North sea bottom steady boundary layer measurements. *J. Waterway, Port, Coastal and Ocean Engng.* **116**, 614–632.

SLEATH, J. F. A. 1974 Velocities above rough bed in oscillatory flow. *J. Waterways, Harbours and Coastal Engng Div.* **100**, 287–304.

SLEATH, J. F. A. 1984 *Sea bed mechanics.* John Wiley & Sons.

SLEATH, J. F. A. 1987 Turbulent oscillatory flow over rough beds. *J. Fluid Mech.* **182**, 369–409.

SLEATH, J. F. A. 1990 Velocities and bed friction in combined flows. *Proc. 22nd Conf. Coast. Engng.* pp. 450–463.

SLEATH, J. F. A. 1991 Velocities and shear stresses in wave–current flows. *J. Geophys. Res.* **96**, 15237–15244.

SLEATH, J. F. A. 1995 Coastal bottom boundary layers. *Appl. Mech. Rev.* **48**, 589–599.

SMITH, J. D. & MCLEAN, S. R. 1977 Spatialy averaged flow over a wavy surface. *J. Geophys. Res.* **82**, 1735–1746.

SRDIĆ, A. N. 1998 Interaction of dense particles with stratified and turbulent environment. PhD thesis, Arizona State University.

SWAN, C. 1990 An experimental study of waves on a strongly sheared current profile. *Proc. 22nd Coast. Engng. Conf.* **1**, 489–502.

TENNEKES, H. & LUMLEY, J. L. 1989 *A first course in turbulence*. The MIT Press.

TOWNSEND, A. A. 1956 *The structure of turbulent shear flow*. Cambridge University Press.

TROWBRIDGE, J. H. & AGRAWAL, Y. C. 1995 Glimpses of a wave boundary layer. *J. Geophys. Res.* **100**, 20729–20743.

TROWBRIDGE, J. H. & KINEKE, G. C. 1994 Structure and dynamics of fluid muds on the Amazon continental shelf. *J. Geophys. Res.* **99**, 865–874.

TROWBRIDGE, J. & MADSEN, O. S. 1984 Turbulent wave boundary layers: 1. model formulation and first-order solution. *J. Geophys. Res.* **89**, 7989–7997.

VILLARET, C. 1987 Etude experimentale et numerique des lois d'erosion pour des sediments cohesifs. *Ph. D. Thesis, Universite Scientifique et Medicale de Grenoble, France* .

VILLARET, C. & DAVIES, A. G. 1995 Numerical models of flow–suspension particle interaction. *Appl. Mech. Rev.* **49**, 601–609.

VILLARET, C. & PERRIER, G. 1992 Transport of fine sand by combined waves and current: an experimental study. *Technical Report, Laboratoire National d'Hydraulique, France, Ref. HE-42/92.68* .

VITTORI, G. & VERZICCO, R. 1998 Direct simulation of transition in an oscillatory boundary layer. *J. Fluid Mech.* **371**, 207–232.

VOROPAYEV, S. I., AFANASYEV, Y. D. & VAN HEIJST, G. J. F. 1995 Two-dimensional flows with zero net momentum: evolution of vortex quadrupoles and oscillating–grid turbulence. *J. Fluid Mech.* **282**, 21–44.

WAYWELL, M. N. & SAJJADI, S. G. 1997 Transition from laminar to turbulence in oscillatory boundary layer flows over a smooth flat plate. *Math. Engng. Ind.* **6**, 79–97.

WHITE, F. M. 1991 *Viscous Fluid Flow.* McGraw–Hill.

BIOGRAPHICAL SKETCH

Rajka Krstić was born in Sombor, Yugoslavia, on December 6, 1969. She received her elementary education at the "Nikola Vukićević" Elementary School in Sombor, Yugoslavia, between 1976 and 1984. In 1986 she completed her general high school education at the Economic High School in Sombor. Her interest in science and engineering motivated her to continue her high school education at the Mathematical High School in Sombor, which she graduated from in 1988. In 1988 she pursued the studies at the Mechanical Engineering Department (Aerospace Engineering Branch), at University of Belgrade. During the studies at the Aerospace Engineering Department, she conducted the student practical training at the Moscow Aviation Institute - Moscow, Russia, during the Fall of 1992. She graduated with the Bachelor degree in Aerospace Engineering, with her Diploma Work in Aerodynamics, in July of 1993.

Following her graduation, in 1993, Rajka came to University of Akron, Ohio, to pursue graduate studies in Mechanical Engineering. In 1996 she graduated with a Master of Science degree in Mechanical Engineering and continued her Doctoral studies at Arizona State University. In 1999 she graduated with a Doctor of Philosophy degree in Aerospace Engineering. Rajka is a student member of the ASME, AIAA and NSPE.